Institute of Thermoelectricity, Academy of Sciences and Ministry of Education and Science of Ukraine

Journal of THERMOELECTRICITY

International Research

Founded in December, 1993

published 6 times a year

No. 3 *2014*

Editorial Board

International Editorial Board

Founders - National Academy of Sciences, Ukraine
Institute of Thermoelectricity of National Academy of Sciences and Ministry of Education and Science of Ukraine

Certificate of state registration № КВ 15496-4068 ПР

Editorial office manager O. Pugantseva

Approved for printing by the Academic Council of Institute of Thermoelectricity of the National Academy of Sciences and Ministry of Education and Science, Ukraine

Address of editorial office:
Ukraine, 58002, Chernivtsi, General Post Office, P.O. Box 86.
Phone: +(380-372) 90 31 65.
Fax: +(380-3722) 4 19 17.
E-mail: jt@inst.cv.ua
http://www.jt.inst.cv.ua

Signed for publication 15.08.14. Format 70×108/16. Offset paper №1. Offset printing.
Printer's sheet 11.1. Publisher's signature 9.2. Circulation 400 copies. Order 6.

Printed from the layout original made by "Journal of Thermoelectricity" editorial board
in the printing house of "Bukrek" publishers,
10, Radischev Str., Chernivtsi, 58000, Ukraine

CONTENTS

P.V. Gorsky

Institute of Thermoelectricity of the NAS and MES Ukraine,
1 Nauky str., Chernivtsi, 58029, Ukraine

P.V.Gorsky

ELECTRIC CONDUCTIVITY OF FUNCTIONAL, INCLUDING THERMOELECTRIC, MATERIALS DESCRIBED BY THE FIVAZ MODEL, IN QUASI-CLASSICAL RANGE OF MAGNETIC FIELDS

Development, optimization and use of these or other functional, including thermoelectric, materials for creation of specific devices, elements and systems supposes their adequately precise description on the basis of certain model assumptions of their band spectrum and the mechanisms of charge carrier scattering in them. In some cases the character of band spectrum of these materials directly determines their range of application. An efficient tool of experimental verification, and not infrequently of formation of the above model assumptions, is for instance, investigation of the Shubnikov-de Haas oscillations with different orientations of a magnetic field. However, for a conventional quasi-classical theory taking into account only relaxation time oscillations, in the framework of which, as a rule, processing and interpretation of the experimental results takes place, the specific character of nonparabolicity of charge carrier band spectrum and finite extension of the Fermi surface along the direction of a magnetic field are inessential. This can result in the uncertainty of determination of, for instance, charge carrier concentration, as well as in the controversy of data on the band spectrum of material obtained by different methods. Therefore, the paper introduces an improved theory of the Shubnikov-de Haas oscillations in functional, including thermoelectric, layered materials described by the Fivaz model. The calculations are performed in the framework of Ohm's law applicability for the case when the electric and quantizing magnetic fields are parallel to each other and perpendicular to the layers. In so doing, three factors are taken into account, namely the oscillating dependence of relaxation time on a magnetic field in the range of application of quasi-classical approximation, the nonparabolicity of charge carriers band spectrum described by the Fivaz model and finite extension of the Fermi surface along the direction of a magnetic field.

Key words: Shubnikov-de Haas effect, Fivaz model, relaxation time, density of states, quasi-classical approximation.

Introduction

The Shubnikov-de Haas effect is an efficient tool of studying the band spectrum and mechanisms of charge carrier scattering in functional, including thermoelectric, materials. Investigation of thermoelectric materials in strong magnetic fields, using this effect as well, is addressed in a number of works [1-3]. Study on the Shubnikov-de Haas effect with different orientations of magnetic field permits in the framework of the Lifshits-Kosevich theory [4] to restore the shape of the Fermi surface, as well as to determine the concentration and relaxation times of charge carriers. However, very often in real crystals there are deviations from the Lifshits-Kosevich theory, owing to which, for instance, charge carrier concentrations, found from the Shubnikov-de Haas

effect and the Hall effect can differ considerably. The reasons for this difference, in particular, can be nonparabolicity of charge carriers band spectrum and finite extension of the Fermi surface along the direction of a magnetic field that are ignored by conventional Lifshits-Kosevich theory. As a consequence, for instance, at zero concentration of charge carriers, this theory, at least formally, yields physically incorrect result, namely there are oscillations in the absence of the Fermi surface. Theory of electric conductivity of crystals described by the Fivaz model [5], free from these restrictions, is constructed in [6], where it is shown that the nonparabolicity effects can be also pronounced in the case of closed Fermi surfaces. However, in this work, an essential model assumption is made that relaxation time of a longitudinal quasi-pulse is only a function of this quasi-pulse and does not oscillate with a variation of a magnetic field. At the same time, from the results of works [7, 8] it follows that in the case when a fair amount of the Landau levels fit in a narrow miniband describing electron motion perpendicular to layers, a decisive contribution to electric conductivity oscillations is made exactly by the magnetic field dependence of relaxation time. This time already depends on the energy of electron as a whole, rather than on a longitudinal quasi-pulse alone. Therefore, the purpose of this paper is develop a consistent theory of the Shubnikov-de Haas oscillations with regard to all the three factors, namely relaxation time oscillations, band spectrum nonparabolicity in the framework of the Fivaz model and finite extension of the Fermi surface along the direction of a magnetic field.

Derivation and analysis of a formula for longitudinal electric conductivity

In the derivation of a formula for longitudinal conductivity we will follow the procedure described in [8], but modify this procedure with regard to the Fermi surface closedness and its finite extension along the direction of a magnetic field. The energy spectrum of charge carriers in thermoelectric material described by the Fivaz model in a quantizing magnetic field perpendicular to layers is determined as:

$$\varepsilon\left(n,k_z\right)=\mu^*B\left(2n+1\right)+\Delta\left(1-\cos ak_z\right). \tag{1}$$

In this formula, n, k_z are the Landau level number and quasi-pulse component in a direction perpendicular to layers, respectively, $\mu^*=\mu_B m_0/m^*$, μ_B, m_0, m^* are the Bohr magneton, free electron mass and electron effective mass in layer plane, respectively, Δ, a are the half-width of mini band in a direction perpendicular to layers and the distance between translation equivalent layers, respectively, B is magnetic field induction.

The relaxation time of a longitudinal quasi-pulse, as with a conventional approach, will be assumed to be inversely proportional to electron states density in a magnetic field. Using the Poisson formula and taking into account the expansion of the Landau levels due to collisions depending on magnetic field B and electron energy ε the relaxation time for the case of energy spectrum (1) can be written as:

$$\tau\left(\varepsilon,B\right)=\frac{\pi\tau_0}{\kappa_\varepsilon}\left\{1-2\exp\left(-\pi kT_{D0}\chi_\varepsilon/\mu^*B\right)\left[\cos\left(\pi\frac{\varepsilon-\Delta}{\mu^*B}\right)\left[C_0J_0\left(\pi\Delta/\mu^*B\right)+\right.\right.\right.$$
$$\left.\left.\left.+2\sum_{r=1}^{\infty}\left(-1\right)^r C_{2r}J_{2r}\left(\pi\Delta/\mu^*B\right)\right]-2\sin\left(\pi\frac{\varepsilon-\Delta}{\mu^*B}\right)\sum_{r=0}^{\infty}\left(-1\right)^r C_{2r+1}J_{2r+1}\left(\pi\Delta/\mu^*B\right)\right]\right\}^{-1}. \tag{2}$$

In this formula, τ_0, T_{D0} are, respectively, relaxation time and the Dingle temperature for an open Fermi surface in the absence of a magnetic field, $\kappa_\varepsilon=\arccos(1-\varepsilon/\Delta)$ for closed constant-energy

surface, and $\kappa_\varepsilon = \pi$ for open constant-energy surfaces, $C_0 = \kappa_\varepsilon$, $C_m = \sin m\,\kappa_\varepsilon/m$, $J_n(x)$ are the Bessel functions of the first kind of actual argument. Therefore, for open surfaces (2) goes over to the formula of [8]. Besides, formula (2), unlike the formula of [8], explicitly takes into consideration the fact that in the absence of the Fermi surface the Shubnikov-de Haas oscillations are absent.

To calculate the electrical conductivity of thermoelectric material, we will need a sum of moduli of electron longitudinal velocities in the occupied Landau subbands. According to [8], with regard to (1) it reduces to calculation of integral of the kind:

$$I = \int_0^\infty \cos\left[\pi\left(\frac{\varepsilon}{\mu^* B} - x\right)\right]\sqrt{2\left(\frac{\varepsilon - \mu^* Bx}{\Delta}\right) - \left(\frac{\varepsilon - \mu^* Bx}{\Delta}\right)^2}\,dx. \tag{3}$$

However, the upper integration limit in this integral is not correct. By analogy with formula (2), the upper integration limit should be equal to $\varepsilon / \mu^* B$. This statement is true inasmuch as, according to the Poisson summation formula, the integration variable x comes from essentially positive value $2n + 1$ in formula (1). The above limitation also explicitly takes into account the absence of the Shubnikov-de Haas oscillations in the absence of the Fermi surface [6]. Therefore, in conformity with procedure [8] with regard to (2), as well as the correct upper limit in (3), the formula for full electric conductivity of thermoelectric material at low temperatures with neglecting the field and temperature dependence of chemical potential acquires the following form:

$$\sigma = \sigma_0 + \sigma_1 + \sigma_2 + \sigma_3. \tag{4}$$

In so doing:

$$\sigma_0 = \frac{8\pi^3 e^2 m^* a \tau_0 \Delta^2}{h^4}\left(1 - \frac{\sin 2\kappa_\zeta}{2\kappa_\zeta}\right), \tag{5}$$

$$\begin{aligned}\sigma_1 = 2\sigma_0 R_T R_D \Bigg\{ &\cos\left(\pi\frac{\zeta - \Delta}{\mu^* B}\right)\left[C_0 J_0\left(\frac{\pi\Delta}{\mu^* B}\right) + 2\sum_{r=1}^{\infty}(-1)^r C_{2r} J_{2r}\left(\frac{\pi\Delta}{\mu^* B}\right)\right] - \\ &-2\sin\left(\pi\frac{\zeta - \Delta}{\mu^* B}\right)\sum_{r=0}^{\infty}(-1)^r C_{2r+1} J_{2r+1}\left(\frac{\pi\Delta}{\mu^* B}\right)\Bigg\},\end{aligned} \tag{6}$$

$$\begin{aligned}\sigma_2 = -\frac{8\pi^3 e^2 m^* a \tau_0 \Delta^2}{h^4} R_T R_D \Bigg\{ &\cos\left(\pi\frac{\zeta - \Delta}{\mu^* B}\right)\Bigg[\left(\tilde{C}_0 - \tilde{C}_2\right) J_0\left(\frac{\pi\Delta}{\mu^* B}\right) + \\ &+\sum_{r=1}^{\infty}(-1)^r\left(2\tilde{C}_{2r} - \tilde{C}_{2r+2} - \tilde{C}_{2r-2}\right) J_{2r}\left(\frac{\pi\Delta}{\mu^* B}\right)\Bigg] + \\ &+\sin\left(\pi\frac{\zeta - \Delta}{\mu^* B}\right)\sum_{r=0}^{\infty}(-1)^r\left(2\tilde{C}_{2r+1} - \tilde{C}_{2r+3} - \tilde{C}_{|2r-1|}\right) J_{2r+1}\left(\frac{\pi\Delta}{\mu^* B}\right)\Bigg\},\end{aligned} \tag{7}$$

$$\sigma_3 = -\frac{8\pi^3 e^2 m^* a \tau_0 \Delta^2}{h^4} R_D^2 \left\{ \left[C_0 J_0\left(\frac{\pi\Delta}{\mu^* B}\right) + 2\sum_{r=1}^{\infty} (-1)^r C_{2r} J_{2r}\left(\frac{\pi\Delta}{\mu^* B}\right) \right] \times \right.$$
$$\times \left[\left(\tilde{C}_0 - \tilde{C}_2\right) J_0\left(\frac{\pi\Delta}{\mu^* B}\right) + \sum_{r=1}^{\infty} (-1)^r \left(2\tilde{C}_{2r} - \tilde{C}_{2r+2} - \tilde{C}_{2r-2}\right) J_{2r}\left(\frac{\pi\Delta}{\mu^* B}\right) \right] + \quad (8)$$
$$\left. + 2\left[\sum_{r=0}^{\infty} (-1)^r C_{2r+1} J_{2r+1}\left(\frac{\pi\Delta}{\mu^* B}\right) \right] \left[\sum_{r=0}^{\infty} (-1)^r \left(2\tilde{C}_{2r+1} - \tilde{C}_{2r+3} - \tilde{C}_{|2r-1|}\right) J_{2r+1}\left(\frac{\pi\Delta}{\mu^* B}\right) \right] \right\},$$

In formulae (5) – (8), ζ is chemical potential of charge carrier gas in material, $C_0 = \kappa_\zeta = \arccos(1 - \zeta/\Delta)$ for closed Fermi surfaces, and $C_0 = \kappa_\zeta = \pi$ for open Fermi surfaces, $C_m = \sin mC_0/m$, $\tilde{C}_m = C_m/C_0$. Reducing multipliers R_T and R_D are given below:

$$R_T = \frac{\pi^2 kT/\mu^* B}{\mathrm{sh}\left(\pi^2 kT/\mu^* B\right)}, \quad (9)$$

$$R_D = \exp\left(-\pi k T_{D0} \kappa_\zeta / \mu^* B\right). \quad (10)$$

The former in a known way takes into account temperature "blurring" of oscillations, and the latter is caused by expansion of the Landau levels due to electron scattering on impurity ions. Exactly this scattering is dominant in the range of existence of the Shubnikov-de Haas oscillations. The nonparabolicity of conduction band of thermoelectric material in formulae (6) – (8) is manifested in the presence of the Bessel functions, and finite extension of the Fermi surface along the direction of the field affects the Shubnikov-de Haas oscillations through modulating coefficients C_m and $\tilde{C}_m$ that become, respectively, zero and unity at $\zeta = 0$, i.e. with disappearance of the Fermi surface. Thus, if the Fermi surface disappears, the Shubnikov-de Haas oscillations disappear "in principle", rather than "in probability" and "on the average". Here lies one of the basic distinctions of the proposed approach from the conventional one.

Components of longitudinal electric conductivity entering into formula (4) can be interpreted as follows. Component σ_0 is electric conductivity of thermoelectric material at low temperatures in the absence of a magnetic field. Component σ_1 determines the main contribution to the Shubnikov-de Haas oscillations due to relaxation time oscillations in the range of quasi-classical approximation applicability. Component σ_2 shows itself even in the absence of relaxation time oscillations. It is caused by quantization of phase space in a magnetic field and can become dominant with increasing induction of a magnetic field. In the range of application of quasi-classical approximation, component σ_2 results only in phase shift and certain renormalization of amplitude of the main oscillations determined by component σ_1. Component σ_3 describes the so-called "slow" oscillations [8] whose frequency does not depend on the sections of the Fermi surface by planes perpendicular to a magnetic field. Owing to this, "slow" oscillations are not subject to temperature "blurring", but decay only due to scattering processes. However, these oscillations disappear alongside with common "quick" oscillations with disappearance of the Fermi surface.

Analysis shows that in the effective mass approximation remain only components σ_0, σ_1, σ_2 and they, respectively, are:

$$\sigma_0 = \frac{32\pi^3 e^2 m^* a \tau_0 \Delta\zeta}{3h^4}, \quad (11)$$

$$\sigma_1 = 2\sigma_0 R_T R_D \sqrt{\frac{\mu^* B}{\Delta}} \left[\cos\left(\frac{\pi\zeta}{\mu^* B}\right) C\left(\sqrt{\frac{\zeta}{\mu^* B}}\right) + \sin\left(\frac{\pi\zeta}{\mu^* B}\right) S\left(\sqrt{\frac{\zeta}{\mu^* B}}\right) \right], \tag{12}$$

$$\sigma_2 = -\frac{32\pi^2 e^2 m^* a \tau_0 \Delta^2}{h^4} R_T R_D \left(\frac{\mu^* B}{\Delta}\right)^{3/2} \left[\sin\left(\frac{\pi\zeta}{\mu^* B}\right) C\left(\sqrt{\frac{\zeta}{\mu^* B}}\right) - \cos\left(\frac{\pi\zeta}{\mu^* B}\right) S\left(\sqrt{\frac{\zeta}{\mu^* B}}\right) \right]. \tag{13}$$

In formulae (12) and (13), $C(x)$ and $S(x)$ are the Fresnel cosine- and sine-integrals, respectively. Inasmuch as $C(0) = S(0) = 0$, in this case we also take into account the fact of disappearance of oscillations with the disappearance of the Fermi surface. Transition to conventional quasi-classical approximation in these formulae is matched by condition $\zeta / \mu^* B >> 1$. Then $C(x) = S(x) \approx 0.5$ and we get:

$$\sigma_1 = \sigma_0 R_T R_D \sqrt{\frac{2\mu^* B}{\Delta}} \cos\left(\frac{\pi\zeta}{\mu^* B} - \frac{\pi}{4}\right). \tag{14}$$

Formula (14) corresponds to conventional Lifshits-Kosevich theory for the Fermi surface with the only extreme, namely maximal section by plane $k_z = 0$, perpendicular to a magnetic field. Exactly this formula, or its modifications for the cases of more compound Fermi surfaces with many extreme sections by planes perpendicular to a magnetic field, is generally used for processing experimental data on the Shubnikov-de Haas effect in functional, including thermoelectric, materials, in the case when the electrical and magnetic fields are parallel to each other. Identically, the formula for component σ_2 acquires the form:

$$\sigma_2 = -\frac{16\sqrt{2}\pi^2 e^2 m^* a \tau_0 \Delta^2}{h^4} R_T R_D \left(\frac{\mu^* B}{\Delta}\right)^{3/2} \sin\left(\frac{\pi\zeta}{\mu^* B} - \frac{\pi}{4}\right). \tag{15}$$

From formulae (14) and (15) it is seen that in the case of crystals described by the Fivaz model the condition of applicability of conventional approach whereby components σ_2 and σ_3 are neglected has the form of $\mu^* B / \Delta << 1$. In this case, for instance, component σ_2 is about $\Delta / \mu^* B$ times lower than σ_1. However, in strongly anisotropic crystals the ratio $\mu^* B / \Delta$ is not too low or even high as compared to unity, owing to which component σ_2 is not only negligibly small, but can become dominant. In this case, theory developed in [6] is correct.

Using standard trigonometric formulae, the total oscillating part of electric conductivity for a closed Fermi surface under the conditions of applicability of quasi-classical approximation can be written as:

$$\sigma_{os} = \sigma_0 R_T R_D \sqrt{1 + a^2} \sqrt{\frac{2\mu^* B}{\Delta}} \cos\left(\frac{\pi\zeta}{\mu^* B} - \frac{\pi}{4} + \phi\right). \tag{16}$$

Parameters a and ϕ describe, respectively, renormalization of the amplitude of oscillations and their phase shift. These parameters are determined as follows:

$$a = 3\mu^* B / 2\pi\zeta, \phi = \text{arctg} a. \tag{17}$$

Hence, under conditions of applicability of quasi-classical approximation, when $\mu^* B / \Delta << 1$, renormalization of amplitude and phase shift of the Shubnikov-de Haas oscillations as compared to

conventional Lifshits-Kosevich theory are small, provided that for a concrete closed Fermi surface the ratio ζ/Δ is not too small as compared to unity.

It formally follows from formula (16) that nonparabolicity described by the Fivaz model does not show itself anyhow in the Shubnikov-de Haas oscillations, if the Fermi surfaces are closed. However, in reality it is not the case. The point is that with the same concentration of charge carriers and closed Fermi surface the Fermi energy of charge carriers in thermoelectric material described by the Fivaz model is somewhat lower than in the effective mass approximation. This difference is due to the fact that with the same energy $\varepsilon < 2\Delta$, i.e. under condition of closed constant-energy surfaces, the density of states in the Fivaz model is higher than in the effective mass approximation. Therefore, even in quasi-classical approximation, as it follows from formulae (16) and (17), the said nonparabolicity should be manifested in the reduction of oscillation frequency, their phase delay and some variation of their relative contribution. The nonparabolicity is even more prominent if instead of quasi-classical formula (16) one uses shrewd formulae (5) – (8) in the framework of the Fivaz model and (11) – (13) in the effective mass approximation. It is evident from Fig.1 which shows that the nonparabolicity described by the Fivaz model results in phase delay of oscillations and rather perceptible reduction of their amplitude. This reduction, just as phase delay, is attributable to the fact that density of states in the Fivaz model is higher, hence, oscillation frequency and relaxation time is lower than in the effective mass approximation.

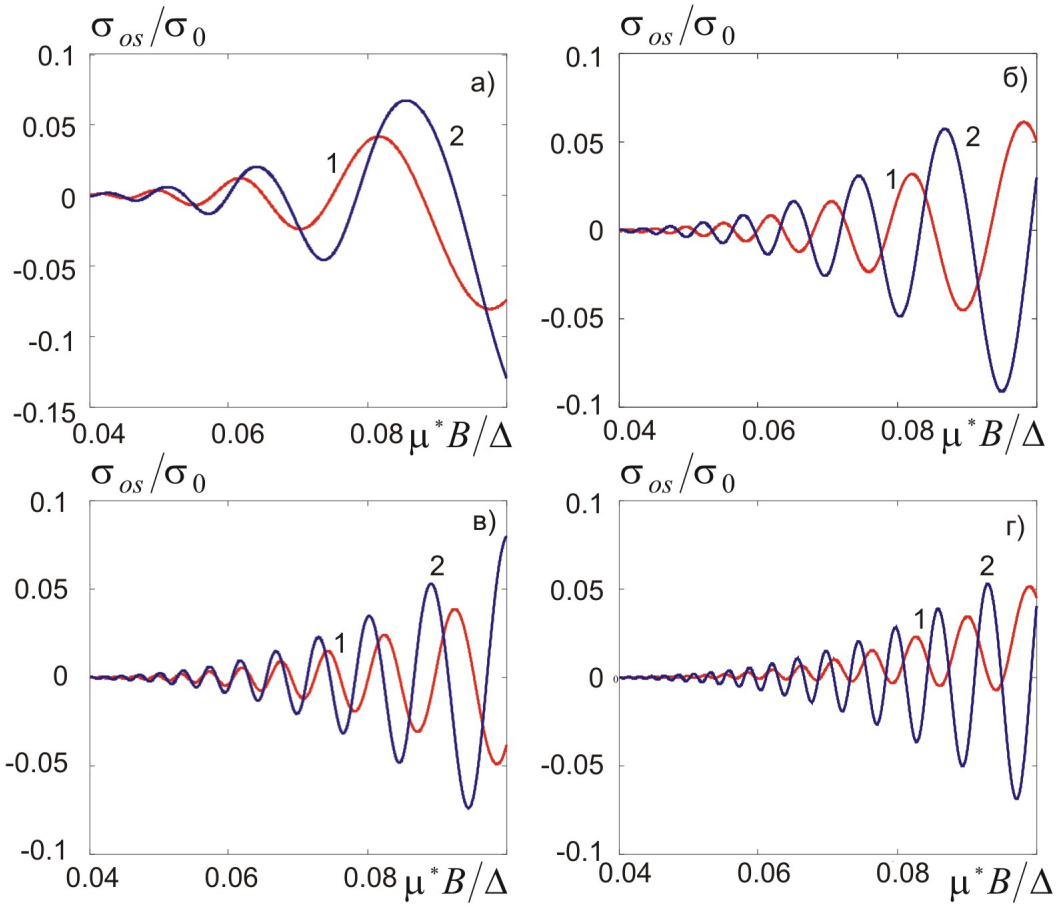

Fig. 1. Field dependence of the oscillating part of electric conductivity of thermoelectric material with closed Fermi surface in conformity with shrewd formulae with ζ/Δ value equal to: a) – 0.5;b) – 1;c) – 1.5; d) – 2. In each figure curves 1 (red) are plotted in the framework of the Fivaz model, curves 2 (blue) – in effective mass approximation.

For comparison, Fig. 2 gives the field dependence of the oscillating part of longitudinal electric conductivity of thermoelectric material in the framework of the Lifshits-Kosevich theory.

For constructing the plots the following crystal band parameters were taken: $\Delta = 0.01$ eV, $m^* = 0.01\, m_0$. These parameters correspond to rather strong crystal anisotropy, since if we take $a = 3$ nm, it turns out that the respective effective mass ratio in directions perpendicular and parallel to the layers is 85, though this is far from being a limit for layered functional materials, including thermoelectric. Moreover, it is assumed that $T = 3$ K and $T_D = 1.5$ K. With such parameters, magnetic fields indicated in the plots correspond to the range from 0.04 to 0.1 T. It was also considered that under condition of constant charge carrier concentration and absolute zero temperature the chemical potential ζ of electron gas in the Fivaz model is related to chemical potential ζ_{em} in the effective mass approximation by the following ratio:

$$(\zeta/\Delta - 1)\arccos(1-\zeta/\Delta) + \sqrt{2\zeta/\Delta - (\zeta/\Delta)^2} = (2\zeta_{em}/\Delta)^{3/2}/3. \qquad (18)$$

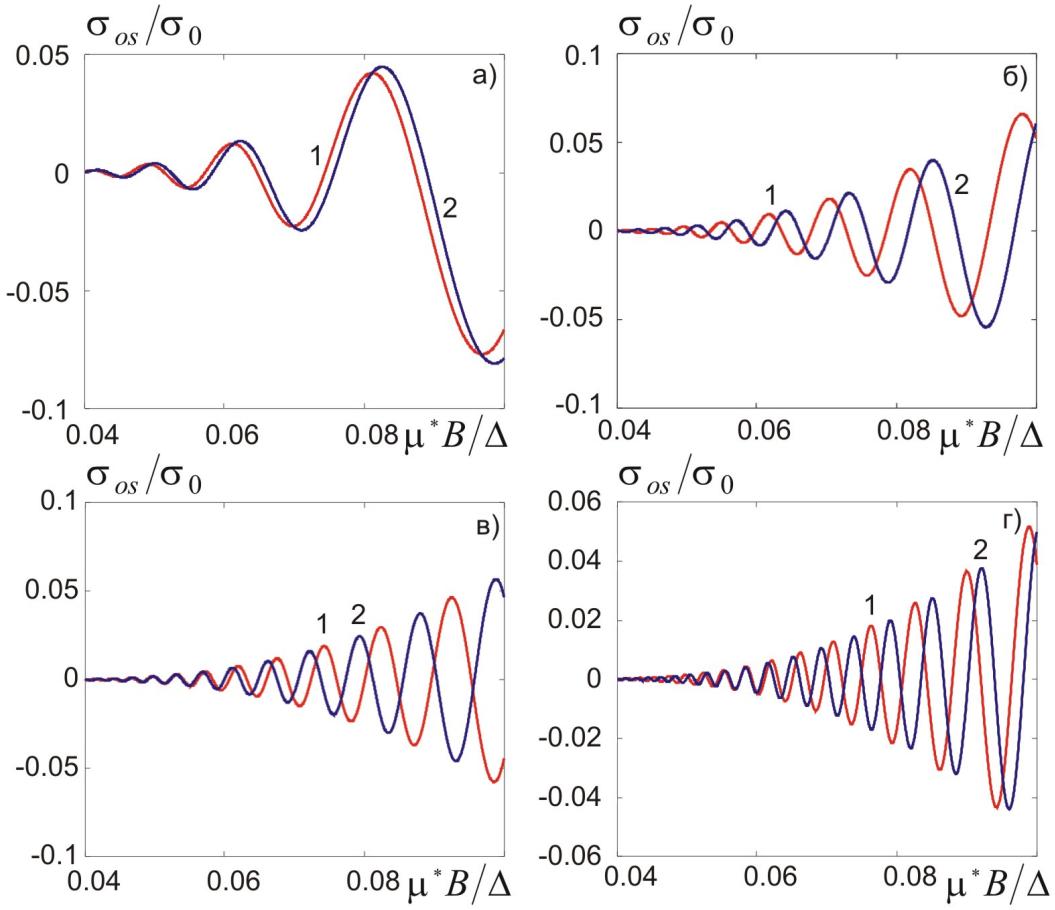

Fig. 2. Field dependence of the oscillating part of electric conductivity of thermoelectric material with closed Fermi surface in the framework of the Lifshits-Kosevich theory with ζ/Δ value equal to: a) – 0.5;b) – 1;c) – 1.5;d) – 2. In each figure curves 1 (red) are plotted in the framework of the Fivaz model, curves 2 (blue) – in the effective mass approximation.

From comparison of Figures 1 and 2 it is seen that with each value of the ratio ζ/Δ curves 1 and 2 constructed by precise formulae differ much wider than the same curves plotted in the framework of the Lifshits-Kosevich theory. This takes place because the Lifshits-Kosevich theory takes into account only an indirect effect of nonparabolicity described by the Fivaz model on the longitudinal electric

conductivity of thermoelectric material. This effect is produced through the value of the Fermi energy, i.e. through the frequency of Shubnikov-de Haas oscillations and through the Dingle factor, as long as it depends on the density of states on the Fermi level, and, other things equal, it reduces the amplitude of oscillations the greater, the greater is this density. Whereas shrewd formulae take into account not only an indirect, but also a direct effect of nonparabolicity on the oscillations of conductivity through the Bessel functions. Moreover, shrewd formulae explicitly take into account finite extension of the Fermi surface along the direction of a magnetic field. With the stipulated problem parameters the relative contribution of the oscillating part of electric conductivity reaches 5 – 7 %. This is much higher than in typical metals where this contribution rarely exceeds 0.1 %. The latter fact simplifies considerably the process of investigation of band structure of such functional, including thermoelectric, materials.

Moreover, from Figure 1 it is seen that with increasing the ratio ζ/Δ, i.e. charge carrier concentration, the difference between curves plotted with and without regard to nonparabolicity described by the Fivaz model is increased. The greatest difference between said curves is traced at $\zeta/\Delta = 2$, i.e. for a "transient" Fermi surface. This takes place because the above surface has no tangential planes perpendicular to magnetic field direction, while with any positive value $\zeta/\Delta < 2$ there are two such planes parallel to plane $k_z = 0$ and symmetric with respect to it.

In conclusion, it is necessary to note a series of additional factors determining the validity and the range of application of the results obtained in this paper. First, the results of this paper are valid when the oscillating part of electric conductivity is a small value as compared to the permanent part. Second, in [8] where the oscillating part of electric conductivity was considered for the case of strongly open Fermi surfaces, it is noted that in this case, apart from the phase shift determined by the relations (17), there is an additional shift of electric conductivity oscillation phases of the order kT_D/Δ. Comparison between the calculations by the author of [8] and the experiment shows that this shift is considerable enough. But then it appears that analysis performed by the author of [8] in the field when the contribution of the oscillating part of electric conductivity is small, is not correct, because in the case of $kT_D/\Delta \geq 1$ the length of electron mean free path is small or, at least, insufficiently large as compared to the distance between translation equivalent layers, and, hence, it is necessary to use other approaches, such as described in [7, 9]. However, discussion of this point is beyond the scope of this paper.

Conclusions and recommendations

1. Under conditions of oscillating dependence of relaxation time on a magnetic field, the nonparabolicity of band spectrum of functional, including thermoelectric, materials described by the Fivaz model, is manifested in phase delay of longitudinal electric conductivity oscillations and their amplitude reduction. These peculiarities become apparent with closed Fermi surfaces.
2. Band spectrum nonparabolicity is the more prominent the greater is charge carrier concentration. Peculiarities of nonparabolicity manifestation are mainly due to fundamental differences between the electronic density of states in the Fivaz model and in the effective mass approximation.
3. The results obtained in the paper can be used for the diagnostics of band structure of materials described by the Fivaz model with closed Fermi surfaces.

The Author is grateful to academician L.I.Anatychuk for the approval of the research issue, as well as for helpful and constructive discussion of the results that contributed to quality improvement of this paper.

References

1. A.A.Nikolaeva, L.A.Konopko, and D.V.Gitsu, Effect of Magnetic Field, Elastic Extension and Dimensions on the Thermoelectric Properties of Bismuth Nanowires, *J.Thermoelectricity* **2,** 21-37 (2008).
2. A.A.Nikolaeva, L.A.Konopko, A.K.Tsurkan, and T.E.Huber, Thermoelectric Properties of Single-Crystal *Bi-Sn* Wires with Different Crystallographic Orientation under Elastic Deformations, *J.Thermoelectricity* **3**, 44-62 (2009).
3. P.Bodiul, D.Gitsu, G.Ivanov, A.Nikolaeva, and G.Para, Peculiarities of Impurity States in Bismuth and Doping Anomaly of Some Transport Phenomena, *J.Thermoelectricity* **1**, 13-21 (1999).
4. D.Shenberg, *Magnetic Oscillations in Metals* (Moscow: Mir, 1986), 680p.
5. R.F.Fivaz, Theory of Layer Structures, *J.Phys.Chem.Sol*. **28** (5), 839-845 (1967).
6. P.V.Gorskyi, Can Layered Structure Effects Be Observed if Fermi Surface is Closed? *Ukr.Phys.J.* **55**(12), 1296-1304 (2010).
7. B.Laikhtman, D.Menashe, Resistance Magneto-Oscillations of Superlattices, *Phys.Rev.B* **52** (12), 8974-8979 (1995).
8. P.D.Grigoriev, Theory of the Shubnikov-de Haas Effect in Quasi-Two-Dimensional Metals, *Phys.Rev.B* **67**, 144401-1-144401-8 (2003).
9. V.M.Gvozdikov, Incoherence, Metal-to-Insulator Transition and Magnetic Quantum Oscillations of Interlayer Resistance in an Organic Conductor, *Phys.Rev.B* **76**, 23125-1-23125-12 (2007).

Submitted 10.06.2014

O.Yu. Titov, Yu.G. Gurevich

O.Yu. Titov

Departamento de Física, CINVESTAV-IPN, Apdo. Postal 14740, Distrito Federal, Mexico

THERMOELECTRIC HEATING AND COOLING IN SEMICONDUCTOR STRUCTURES: NONEQUILIBRIUM CHARGE CARRIERS. (Review)

Yu.G. Gurevich

The paper is dedicated to the analysis of thermoelectric cooling phenomena in semiconductors containing potential barriers at the p-n-junction interface. The formulation of an adequate self-consistent theoretical model describing the effect is presented. The role of the recombination rate as a new source of heat in linear approximation of the electric current is discussed, leading to a reformulation of the heat balance equations. The presented recombination of the nonequilibrium carriers always depends on the temperature heterogeneity connected with thermoelectric cooling. Therefore, the nonequilibrium carrier concentrations do not disappear even at very short life times. The importance of redistribution of nonequilibrium charge carriers which has been ignored in most publications on this subject is also shown. The conventional theory of thermoelectric cooling, not taking into account the influence of the nonequilibrium charge carriers, is shown to be inadequate. Besides, when the recombination rate decreases, cooling changes to heating.

Key words: Joule effect, Peltier effect, Thomson effect, Seebeck effect.

Introduction

Traditionally, researchers considered thermoelectric cooling (heating) in terms of the availability of sinks or sources of heat in a heterogeneous system through which the electric current flows [1]. However, in 2 – 4 it has been shown that the thermodynamic process of cooling (heating) can be explained by considering the Le Chatelier-Braun principle [5]. To summarize the content of 2 and 4, the change in the drift heat flux $q_{dr} = \Pi j$ (where Π is the Peltier coefficient and j the electric current density) in a heterogeneous system causes a thermodiffusion heat flux $q_{diff} = -\kappa \nabla T$ (where κ is the thermal conductivity and T the temperature) compensating this change. Due to this thermodiffusion heat flux, temperature heterogeneity arises that cools (heats) the system depending on the electric current direction and material properties. When the temperature in the system is below the equilibrium temperature, we have the effect of thermoelectric cooling, and when the temperature is above the equilibrium temperature, we have the thermoelectric heating effect.

A *p-n* structure is used to make the thermoelectric refrigerator, [1, 6 – 9] because of thermoelectric drift fluxes directed (at a corresponding direction of a current from the *n*-region to *p*-region) from the interface toward the edge in both layers of the *p-n* structure that strengthens the cooling phenomenon [2]. Traditionally studies of the Peltier effect do not consider the nonequilibrium charge carriers [1 – 4, 6 – 9], so that only majority charge carriers and their electric current are taken into account in the expressions for heat fluxes in *n*- and *p*-regions, in spite of the fact that the current of minority charge carriers near the *p-n* junction has the same order of magnitude as the current of

majority charge carriers [10]. In this way, the thermal generation and extraction of minority charge carriers must take place near the interface to allow the flow of electric current [10]. As a consequence, nonequilibrium charge carriers will arise. In Ref. 11 some aspects of this problem were discussed. On the other hand, the effect of nonequilibrium charge carriers on the generation of thermoelectromotive force (EMF) (Seebeck effect) has been studied in detail [12, 13]. In this work, an alternative approach to the physics of thermoelectric cooling in *p-n* junctions is presented [14-16].

Nonequilibrium Charge Carriers Effect On Thermoelectric Cooling (Heating)

In the linear approximation with respect to the electric current, the heat balance equation is given by [2], [17]:

$$\nabla \cdot q = \varepsilon_g R, \tag{1}$$

where $q = q_{dr} + q_{diff}$ is the heat flux, R is the recombination rate, ε_g is the band gap. In Section III we will show that, in linear approximation, for both strong and weak recombination rates the right hand side of Eq. (1) becomes null.

The expression for q_{dr} in bipolar semiconductors is as follows:

$$q_{dr} = P_n j_n + P_p j_p \tag{2}$$

Here q_{dr} are the drift heat fluxes in *n*- and *p*-type semiconductors, $j_{n,p}$ and $P_{n,p}$ are the electron and hole electrical currents and the Peltier coefficients.

The Peltier coefficients in nondegenerated semiconductors are defined by the following expressions [7]:

$$\Pi_{n,p} = \mp \frac{1}{e}\left(\left[r_{n,p} + 5/2 \right] T - \mu_{n,p} \right) \tag{3}$$

where $\mu_{n,p}$ are the Fermi quasi-levels for electrons and holes in *n*- and *p*-regions, *e* is the hole charge, and $r_{n,p}$ are the exponents in the momentum relaxation times [18]. It should be borne in mind that the absolute value of the Peltier coefficient of minority carriers can be much in excess of that of majority carriers.

Since the Fermi quasi-levels depend on the concentration of majority and minority charge carries, the Peltier coefficients will depend on the coordinate *x* (in the space-charge layer near the *p-n* junction ($-r_D^n < x < r_D^p$, where $r_D^{n,p}$ is the Debye radius in the *n*- and *p*-region)) even in linear approximation of Eq. (2) with respect to the current, due to the coordinate dependence of the equilibrium concentrations near the *p-n* junction.

The expression for diffusion heat fluxes $q_{diff}^{n,p}$ is as follows:

$$q_{diff} = -\left(\kappa_n + \kappa_p + \kappa_{ph} \right) \nabla T , \tag{4}$$

where κ_n, κ_p, and κ_{ph} are the electron, hole, and phonon heat conductivities in *n*- and *p*-regions.

Since $\kappa_{n,p} << \kappa_{ph}$ in nondegenerated semiconductors then Eq. (4) reduces to:

$$q_{diff}^{n,p} = -\kappa_{ph}^{n,p} \nabla T, \tag{5}$$

Taking into account the considerations given above, the heat balance Eq. (1) can be rewritten as follows:

$$-\kappa_{ph} \Delta T + \Pi_n \nabla \cdot j_n + \Pi_p \nabla \cdot j_p + j_n \nabla \Pi_n + j_p \nabla \Pi_p = \varepsilon_g R \tag{6}$$

Since the current densities can be calculated as [19]:

$$\begin{aligned} j_n &= -\sigma_n\left(\nabla\phi - \nabla\mu_n/e + \alpha_n\nabla T\right), \\ j_p &= -\sigma_p\left(\nabla\phi + \nabla\mu_p/e + \alpha_p\nabla T\right), \end{aligned} \tag{7}$$

then the calculation of μ_n, μ_p, and ϕ is required. Here $\sigma_{n,p}$ are the electric conductivities, $\alpha_{n,p}$ the Seebeck coefficients ($\Pi_{n,p} = \alpha_{n,p}T$), and ϕ the electric potential.

The macroscopic description of the transport of nonequilibrium charge carriers is performed using the continuity equations for the electron and hole current densities and the Poisson equation [20]:

$$\nabla \cdot j_n = eR, \tag{8a}$$

$$\nabla \cdot j_p = -eR, \tag{8b}$$

$$\Delta\phi = 4\pi\frac{\rho}{\varepsilon} \tag{9}$$

where ρ are the space charges, ε the permittivities, and R the recombination rates in n- and p-regions.

The recombination rate in the presence of temperature gradient was obtained in [20], [21]:

$$R = \tau^{-1}\left[\left(n(x) - n_0\right) + A\left(p(x) - p_0\right) + \beta\left(T(x) - T_0\right)\right], \tag{10}$$

where n and p are the concentrations of electrons and holes, n_0 and p_0 the equilibrium concentrations of electrons and holes, and T_0 the equilibrium temperature. Expressions for τ, A, and β can be found in [20], [21]. It must be emphasized that τ, A and β only depend on the semiconductor properties. It is important to note that τ varies in inverse proportion to the capture coefficients, whereas A and β are finite at any magnitude of the capture coefficients. Let us emphasize that the chemical potentials of electrons and holes ($\mu_{n,p}$) and their concentrations (n and p) are connected by simple algebraic expressions [13]. Let us note that $\mu_n + \mu_p = -\varepsilon_g$ at equilibrium. Hence the system of four equations (7) – (9) describes the behaviour of four unknown functions δn, δp, $\delta\phi$, and δT (or $\delta\mu_n$, $\delta\mu_p$, $\delta\phi$, and δT), where $\delta n = n - n_0$, $\delta p = p - p_0$, $\delta\phi = \phi - \phi_0$, $\delta T = T - T_0$, $\delta\mu_{n,p} = \mu_{n,p} - \mu^0_{n,p}$ (T_0, $\mu^0_{n,p}$, and ϕ_0 are the temperature, chemical potentials, and electric potential of the p-n structure at equilibrium respectively). Nonequilibrium temperatures appear in our linear problem from Peltier effect [2-3]. In linear approximation, $\delta n = (n_0/T_0)\delta\mu_n$, $\delta p = (p_0/T_0)\delta\mu_p$ [13].

The charge density in Eq. (9) may be written as $\rho = \rho_0 + \delta\rho$,where ρ_0 and $\delta\rho$ are the equilibrium and non equilibrium densities of charge that are composed of electrons, holes and the carriers (both electrons and holes) captured on impurity levels, therefore [14, 23]

$$\delta\rho = e(B\delta p - C\delta n + D\delta T) \tag{11}$$

An approximation commonly used to solve the system of equations (8 – 9) in p-n junctions is the assumption of quasineutrality out of the space charge region [24]. The use of the quasineutral approximation is acceptable if the quasi-neutral region length and the minority carrier diffusion lengths are both larger than the Debye length. In this case [13, 23] instead of the Poisson equation we have (see Eq. (11)):

$$\delta\rho = 0 \tag{12}$$

Eq. (7) may be rewritten as:

$$R = R_n = R_p = 1/\tau[E\delta n + F\delta T] \tag{13}$$

Boundary Conditions

The system of Eqs. (1) and (8-9) which defines the thermoelectric cooling must be complemented with the appropriate boundary conditions, which describe the electric currents, the heat flux, and the electric potential through the interface. A very important question is the choice of the boundary conditions used when solving the carrier-transport equations. It should be noted that the expressions commonly used are valid only for semiconductor devices operating in open-circuit conditions (see, for instance Ref. 10). Since in normal operation a current flows at the terminals, the widespread use of boundary conditions for open-circuit conditions is incorrect. For closed-circuit conditions, a different set of boundary conditions needs to be derived. This problem has only been addressed in the last few years [19, 22].

Let us assume that in the *y*- and *z*- direction the *p*-*n* junction is adiabatically isolated. Then the boundary conditions in the remaining direction (i.e. the *p*-*n* junction interface is orthogonal to the *x*-axis and assuming that the interface is located at $x = 0$, the n region located between $x = -l_n$ and $x = 0$, the p region between $x = 0$ and $x = l_p$) are given below.

Assuming that an ideal metal-semiconductor contact is placed at $x = -l_n$ we can write the following boundary conditions for the excess of temperature and carrier densities (hereafter a superscript *n* or *p* in a magnitude refers to the *n* or *p* region respectively):

$$\delta T^n(-l_n) = 0 \tag{14}$$

$$\delta n(-l_n) = 0 \tag{15}$$

$$\delta\phi(-l_n) = 0 \tag{16}$$

These boundary conditions are justified because of the high value of the thermal conductivity of metals and intense recombination at the metal-semiconductor interface. Similar boundary conditions may be written at the metal-semiconductor interface at $x = l_p$:

$$\delta T^p(l_p) = 0 \tag{17}$$

$$\delta p(l_p) = 0 \tag{18}$$

$$\delta\phi(l_p) = -V \tag{19}$$

where V is the applied voltage. These boundary conditions assume that the semiconductor is at the equilibrium in $x = -l_n$ and in $x = l_p$, in other situation, the electric potential (i.e. Eqs. (16) and (19) cannot be rigorously defined [25].

At the *p*-*n* junction interface we can introduce three additional boundary conditions [19], [22]:

$$\begin{aligned}
&\delta\phi^n(0) - \frac{\delta\mu_n^n(0)}{e} - \frac{1}{e}\frac{\partial\mu_{n_0}^n}{\partial T}\delta T^n(0) = \\
&\delta\phi^p(0) - \frac{\delta\mu_n^p(0)}{e} - \frac{1}{e}\frac{\partial\mu_{n_0}^p}{\partial T}\delta T^p(0) \\
&\delta\phi^n(0) + \frac{\delta\mu_p^n(0)}{e} - \frac{1}{e}\frac{\partial\mu_{n_0}^n}{\partial T}\delta T^n(0) = \\
&\delta\phi^p(0) + \frac{\delta\mu_p^p(0)}{e} - \frac{1}{e}\frac{\partial\mu_{n_0}^p}{\partial T}\delta T^p(0)
\end{aligned} \tag{20}$$

$$Q^n(0) = Q^p(0) \tag{21}$$

$$j_n^n(0) = j_n^p(0) \tag{22}$$

$$\delta T^n(0) = \delta T^p(0) \tag{23}$$

These boundary conditions are obtained, assuming respectively continuity of the electrochemical potential at the interface that both heat and electrical conductivities are very large at the junction, and absence of surface recombination. In fact, because the p-n interface is inside the depletion region, this assumption is not realistic and boundary conditions with finite conductivities need to be used [19], in this work we use Eq. (20) – (23) for the sake of simplicity. Finally, it should be noted that in the regions where quasi-neutrality condition holds $\delta\rho = 0$ and the Poisson equation becomes algebraic adopting the form $\delta n = -A'\delta p - B'\delta T$ where A' and B' are constants.

Simplification of the Model of Thermoelectric Cooling in two Limiting Cases

In this Section we will analyse the thermoelectric cooling in a p-n junction in the two limiting cases: strong and weak recombination.

A. Weak Recombination

Let us now consider that the volume recombination is weak. In this case, the conditions $l_D >> l_{n,p} >> r_D$ are fulfilled, which means that the weak recombination is correct for thin film *p-n* structures. Formally $R = 0$ when $\tau \to \infty$. Under this condition the right-hand side of Eq. (1) becomes trivially null and Eq. (1) along with Eqs. (4) and (5) transforms into:

$$\Delta T = 0 \tag{24}$$

and Eqs. (8) into:

$$\nabla \cdot j_{n,p} = 0. \tag{25}$$

From Eqs. (25) it follows that $j_{n,p}$ are not dependent on the coordinates and $j_n^n + j_p^n = j_n^p + j_p^p = j_0$, where j_0 is the whole of current through *p-n* structure. From the boundary conditions for currents [19] it follows that $j_n^n + j_n^p = j_0^n$, $j_p^n + j_p^p = j_0^p$ $(j_0^n + j_0^p = j_0)$.

It is not difficult to understand that the concentrations of the nonequilibrium carriers (δn and δp) are maximal in this case.

It may seem that the calculation of the thermoelectric cooling does not require the use of Eqs. (25) in the absence of recombination because there are no other unknown functions in Eq. (24). So, it would look like that the thermoelectric cooling does not depend on the nonequilibrium carrier concentrations. However, the boundary conditions to Eq. (24) must be formulated for heat fluxes (Eqs. (2) and (5)). The drift heat fluxes depend on the current of majority and minority carriers (Eq. (2)). The latter essentially depends on the distribution of nonequilibrium carrier concentration because of the terms $(\nabla\mu_{n,p})/e$. Therefore there are no reasons to assume a priori that $j_n^n >> j_p^n$ and $j_p^p >> j_n^p$.

The problem is reduced to the calculation of currents in the electrical circuit composed of two circuits connected in parallel. One of them is composed of two *n*-type semiconductors connected in series with the concentrations n^n and n^p, whereas the other is composed of two *p*-type semiconductors connected in series with the concentrations p^n and p^p. At a chosen direction of current (from *n*- to *p*-region) heating instead of cooling takes place at weak recombination [2, 11].

With respect to what was said above, let us notice that the classic theory for current-voltage characteristic through the *p-n* junction [26] obeys the following expression:

$$j_0 = j_s\left(\exp\left(\frac{eV}{T}\right)-1\right), \tag{26}$$

where the saturation current (j_s) varies in direct proportion to the capture coefficients. It follows from Eq. (26) that the current j_0 through the *p-n* junction is equal to zero when the recombination is absent under any voltage.

It means that the model (Eq. (26)) is not correct when the recombination is weak. At the same time, Eq. (25) (together with Eq. (24)) will give the correct expression for current j_0 (at least under weak voltage). The main result is that the temperature deviation from equilibrium at the junction may be obtained:

$$\begin{aligned}
\delta T^n(0) = {} & j_0 l_n\left[\left(\Pi_n^p+\Pi_p^n\right)^2\left(\left(\Pi_n^p\right)^2\frac{l_p}{\sigma_p^p}+\left(\Pi_p^n\right)^2\frac{l_n}{\sigma_n^n}\right)\right]+\\
& +j_0 l_n H\left[\left(\Pi_n^p\right)^2\left(\frac{l_p}{\sigma_n^p}+\frac{l_n}{\sigma_p^n}\right)\left(\frac{l_n}{\sigma_p^n}+\frac{l_p}{\sigma_p^p}\right)\right]+\\
& +j_0 l_n H\left[\left(\Pi_p^n\right)^2\left(\frac{l_p}{\sigma_n^p}+\frac{l_n}{\sigma_p^n}\right)\left(\frac{l_p}{\sigma_n^p}+\frac{l_p}{\sigma_n^n}\right)\right]+\\
& +j_0 l_n H\left[\left(\Pi_p^n+\Pi_n^p\right)^2\left(\frac{l_p}{\sigma_n^p}+\frac{l_n}{\sigma_p^n}\right)\frac{l_n l_p}{\sigma_n^p\sigma_p^n}\right]
\end{aligned} \tag{27}$$

The expression of H is:

$$H = \frac{T_0}{l_n l_p}\left(\kappa_{ph}^n l_p + \kappa_{ph}^p l_n\right) \tag{28}$$

From this expression it follows that a positive current will generate heat instead of cooling at the junction in strong contrast with the conventional results.

B. Strong Recombination

Let us assume that the recombination is very strong. The physical meaning is that $l_{n,p} >> l_D \to 0 >> r_D \to 0$. From a mathematical point of view we have $\tau \to 0$ in Eq. (10).

Since the recombination rate (R) cannot be infinite at $\tau \to 0$, then from Eq. (10) it follows that:

$$\delta n = -A\delta p - \beta\delta T. \tag{29}$$

At the same time, the magnitude R is finite but not defined. Adding Eqs. (8a) and (8b) we have:

$$\nabla\cdot\left(j_n^n + j_p^n\right) = 0,\ \ \nabla\cdot\left(j_n^p + j_p^p\right) = 0. \tag{30}$$

It is important to emphasize that the nonequilibrium charge carrier concentrations (δn and δp) are not equal to zero in the considered approximation. Therefore, there is no reason to state that $j_n^n >> j_p^n$ and $j_p^p >> j_n^p$.

Therefore, the volume Eq. (1) transforms again into:

$$\Delta T = 0. \tag{31}$$

Once again, just like in the weak recombination case, the right-hand side of Eq. (1) also becomes zero, but for very different physical reasons. But, as in the case of weak recombination, the heat flux depends on the nonequilibrium carrier concentrations. The latter are defined by Eqs. (29), (30), and (31) with the corresponding boundary conditions.

In the previous case, it was noted that Eq. (26) is not correct when the recombination is weak enough. Also, it is not difficult to understand that Eq. (26) is not correct in the case of strong recombination. It follows from the expression for j_s that $j_s \to \infty$ when $\tau \to 0$ at any applied voltage V. The last statement is not correct from the physical point of view. The method described above allows the calculation of the current-voltage characteristic of the *p-n* junction in the case of the strong recombination in the linear regime with respect to the applied voltage V.

The temperature deviation at the junction has been analytically obtained:

$$\delta T^n(0) \propto j_0 l_n \left[\sigma_n^n \sigma_p^p \left(\Pi_n^n - \Pi_p^p \right) + \sigma_p^n \sigma_p^p \Pi_p^n - \sigma_n^n \sigma_n^p \Pi_n^p \right] \tag{32}$$

This expression clearly differs from that commonly used:

$$\delta T^n(0) \propto j_0 \sigma_n^n \sigma_p^p \left(\Pi_n^n - \Pi_p^p \right) l_n \tag{33}$$

The differences are not only in magnitude but also in sign. Contrary to Eq. (33), that for the positive values of j_0 only predicts increases in temperature with j_0, Eq. (32) predicts that a *p-n* junction under the same bias conditions (positive values of j_0) may be heated or cooled depending on the values of the Peltier coefficients and electrical conductivities in the *p-n* junction. Moreover, Eq. (32) clearly shows the paramount importance of the nonequilibrium carriers at both sides of the junction (neglected in Eq. (33)) since they control the sign of $\delta T^n(0)$.

Finally, let us emphasize that only when the following two criteria are simultaneously met:

$$\frac{\Pi_n^n}{\Pi_n^p} \gg \frac{\sigma_n^p}{\sigma_p^p} \quad \frac{\Pi_p^p}{\Pi_p^n} \gg \frac{\sigma_p^n}{\sigma_n^n} \tag{34}$$

Eq. (32) reduces to Eq. (33).

When is the Conventional Theory of the Thermoelectric Cooling Correct?

The equations used to describe the thermoelectric cooling in conventional theory are [1 – 4, 6 – 9] Eq. (31) and

$$q_n = -\kappa^n{}_{ph} \nabla T + \Pi^n{}_n j^n{}_n \tag{35}$$

$$q_p = -\kappa^p{}_{ph} \nabla T + \Pi^p{}_p j^p{}_p \tag{36}$$

and it is assumed that $j^n{}_n = j^p{}_p = j_0$ and do not depend on the coordinates. Also $\Pi^n{}_n$ and $\Pi^p{}_p$ are assumed to be constant in space.

However, the question "when is the appointed model correct?" is not discussed in any of the references cited above (and it is absent from all the works concerned with the problem of the thermoelectric cooling). Only in Ref. 11 was the previous question considered from physical (but not mathematical) point of view. Therefore, the following question arises: "can Eqs. (31), (35), and (36) be correct?" and if the answer is "yes", then "under what conditions?"

As it was shown in the previous section, the heat balance equation has the form of Eq. (31) in the two limit cases (strong and weak recombination) if the quasineutrality condition is assumed. Eqs.

(35), (36) do not apply to the weak and intermediate recombination cases. Therefore, we focus our attention only on the strong recombination case. We observe that Eqs. (2) and (5) can be reduced to Eqs. (35)-(36), if the following conditions are fulfilled:

$$j^n{}_n >> j^n{}_p, j^p{}_p >> j^p{}_n \tag{37}$$

These conditions are satisfied only when δn, $\delta p \to 0$. However, as it can be seen from Eqs. (12) and (29), δn, $\delta p \to 0$ only when $\beta \to 0$. From physical point of view it would mean that the charge carrier concentrations do not depend on local temperature $T(x)$. However, this situation will never occur.

Therefore, the thermoelectric cooling described by Eqs.(31), (35) and (36) in the conventional theory is not correct.

Finally, let us emphasize that one of the main assumptions in this work is that the lateral surfaces of the $p-n$ structure are thermally isolated (adiabatic isolation, adiabatic Peltier effect [2]). In this situation the $p-n$ structure, which is being investigated, does not have energy interaction with the surroundings, thus the Peltier effect shows itself "clearly".

However, in practice, there is another situation of great interest, namely the ideal thermal interaction of the *p-n* structure with the surroundings (isothermal Peltier effect [1, 9]). It is clear that $\nabla T = 0$ inside of the structure under these conditions. In this case, the problem of thermoelectric cooling is reduced to the calculation of the amount of heat, absorbed (released) by the *p-n* structure from (to) the surroundings, in order to satisfy the condition imposed by $\nabla T = 0$. From our point of view, such problem formulation is too artificial.

Finding the heat flux in the conventional theory is easy, from Eqs. (35) – (36), and imposing $\nabla T = 0$, we directly have

$$q_{ext} = (\Pi^n{}_n - \Pi^p{}_p) j_0 \tag{38}$$

In the model presented in this article, the calculation of q_{ext} demands the solution of the system of Eqs. (8), (12), and (31) with $\nabla T = 0$ and the corresponding boundary conditions.

For the isothermal Peltier effect the condition $\tau \to 0$ (strong recombination) assures the disappearance of the nonequilibrium charge carrier concentrations $\delta n = \delta p = 0$ and the conversion to conventional theory.

Conclusions

It was shown that the theory of thermoelectric cooling (adiabatic Peltier effect) can not be created without taking into account the existence of nonequilibrium electron and hole concentrations. The presented recombination of the nonequilibrium carrier always depends on the temperature heterogeneity connected with the thermoelectric cooling. Therefore, the nonequilibrium carrier concentrations do not disappear even at very short life times. The simplifications related to the quasineutrality approximation for both weak and strong recombination were analyzed. In the present work it is demonstrated that the Peltier effect strongly depends on the recombination rate. In particular, it is shown that the sign of the Peltier effect changes with the value of the recombination rate.

Acknowledgment. The authors wish to thank CONACYT-Mexico for partial financial support.

References

1. *Thermoelectrics Handbook: Macro to Nano*, edited by D.M. Rowe (Taylor & Francis, London/CRC, Boca Raton, FL, 2006).
2. Yu.G. Gurevich and G.N. Logvinov, *Semicond. Sci. Technol*. **20**, R57 (2005).
3. G.N. Logvinov, J.E. Velásquez, I.M. Lashkevych, and Yu.G. Gurevich, *Appl. Phys. Lett*. **89**, 092118 (2006).
4. Yu.G. Gurevich and G. N. Logvinov, *Rev. Mex. Fis*. **53**, 337 (2007).
5. R. de Groot and P. Mazur, *Non-Equilibrium Thermodynamics* (Dover, New York, 1984).
6. A.F. Ioffe, *Semiconductor Thermoelements and Thermoelectric Cooling* (Infosearch, London, 1957).
7. J. Tauc, *Photo and Thermoelectric Effects in Semiconductors* (Pergamon, Oxford, 1962).
8. L.I. Anatychuk, *Physics of Thermoelectricity* (Institute of Thermoelectricity, Kyiv, Chernivtsi, 1998).
9. G.S. Nolas, J. Sharp, and H.J. Goldsmid, *Thermoelectrics. Basic Principles and New Materials Development* (Springer, Berlin, New York, 2001).
10. K. Seeger, *Semiconductor Physics* (Springer, Berlin, 1985).
11. Yu.G. Gurevich, G.N. Logvinov, O.Yu. Titov, and J. Giraldo, *Surf. Rev. Lett*. **9**, 1703 (2002).
12. Yu.G. Gurevich, O.Yu. Titov, G.N. Logvinov, and O.I. Lyubimov, *Phys. Rev*. B **51**, 6999 (1995).
13. Yu.G. Gurevich, G.N. Logvinov, G. Espejo, I.N. Volovichev, O.Yu. Titov, and A. Meriuts, *Phys. Status Solidi B* **231**, 278 (2002).
14. Igor Lashkevych, Carlos Cortes, and Yuri G. Gurevich, *Journal of Applied Physics* **105**, 053706 (2009).
15. Yu.G. Gurevich, J.E. Velázquez-Pérez, *Journal of Applied Physics* **114**, 1033704 (2013).
16. Yu.G. Gurevich, J.E. Velazquez-Perez, *Peltier Effect in Semiconductor*, Wiley Encyclopedia of Electrical and Electronics Engineering (John Wiley and Sons, p. 1 – 21, 2014), DOI:10.1002/047134608X.W8206
17. L. Villegas-Lelovsky, G. Gonzalez de la Cruz, and Yu.G. Gurevich, *Thin Solid Films*, **433**, 371 (2003).
18. V.F. Gantmakher, I.B. Levinson, *Carrier Scattering in Metals and Semiconductors*, Vol. 19 of Modern Problems in Condensed Matter Science (Amsterdam, Netherlands: North-Holland, 1987).
19. I.N. Volovichev, J.E. Velazquez-Perez, Yu.G. Gurevich, *Solid-State Electronics* **52**, 1703 (2008).
20. I.N. Volovichev, G.N. Logvinov, O.Yu. Titov, and Y.G. Gurevich, *J. Appl. Phys*. **95**, 4494 (2004).
21. Yu.G. Gurevich and I.N. Volovichev, *Phys. Rev. B* **60**, 7715 (1999).
22. O.Yu. Titov, J. Giraldo, Yu.G. Gurevich, *Applied Physics Letters* **80**, 3108 (2002).
23. Yu.G. Gurevich, J.E. Velazquez-Perez, G. Espejo-Lopez, I.N. Volovichev, O.Yu. Titov, *Journal of Applied Physics* **101**, 023705 (2007).
24. J.N. Chazalviel, *Coulomb Screening by Mobile Charges* (Boston: Birkhauser, 1999).
25. Yu.G. Gurevich, V.B. Yurchenko, *Sov. Phys. Semicond*. **25**, 1268 (1991).
26. C.T. Sah, R.N. Noyce, W. Shockley, *Proc. IRE* **45**, 1228 (1957).

Submitted 16.07.2014

D.M. Freik, B.S. Dzundza, V.I. Makovyshyn, L.Yo. Mezhylovska, V.I. Bachuk

[1]Vasyl Stefanyk Precarpathian National University, 57, Shevchenko Str.,
Ivano-Frankivsk, 76018, Ukraine

THERMOELECTRIC PROPERTIES OF VAPOUR-PHASE CONDENSATES BASED ON DOPED LEAD TELLURIDE *SnTe*:*Bi*

Thermoelectric properties of vapour-phase condensates based on doped tin telluride SnTe:Bi of different composition obtained in open vacuum on glass ceramic and mica substrates are investigated. It is shown that thin films on fresh (0001) cleavages of muscovite mica with the content of ~ 0.3 mol.% Bi are characterized by maximum values of thermoelectric power ~ 42 μW/K²cm.
Key words: thin films, tin telluride, doping, thermoelectric properties.

Introduction

Tin telluride is widely used in semiconductor engineering. It also offers great promise as thermoelectric material for medium-temperature range (500 – 750 K) [1, 2, 3]. Preparation of thin film material extends considerably the limits of practical application. The problem of temporal stability of electrical parameters remains to be solved. Moreover, on exposure to air, a layer enriched with *p*-type conductivity carriers is formed on the film surface due to the acceptor effect of oxygen [4].

This paper studies the thickness dependences of thermoelectric parameters of films based on pure and bismuth doped *SnTe* obtained from the vapour phase on glass ceramic and mica substrates.

Experimental procedure

Films for investigation were prepared by vapour deposition of synthesized *SnTe* material in vacuum onto the substrates of fresh (0001) cleavages of muscovite mica and glass ceramic. The temperature of evaporator was T_{ev} = 870 K, and substrate temperature T_{sub} = 470 K. Film thickness was assigned by deposition time within (5 – 480 s) and measured by interference microscope MII-4.

The electric parameters of the films were measured in the air at room temperatures in constant magnetic fields on the elaborated automated installation assuring both the process of electric parameters measurement and recording and primary data processing, with the possibility of constructing the plots of time and temperature dependences. The sample being measured had four Hall and two current contacts. As the ohmic contacts, silver films were used. Current through the samples was ≈ 1 mA. Magnetic field was directed perpendicular to the surface of films at induction of 1.5 T.

The results of investigation and the thickness dependences of electric conductivity σ, the Hall concentration of current carriers n_H and the Seebeck coefficient *S* are represented in Figs. 1 – 2.

Analysis of the results of investigation

The introduction of *Bi* leads to donor effect in tin telluride which is manifested in decreasing hole concentration in the bulk of the films. The results of investigation of thermoelectric parameters of vapour-phase condensates based on doped tin telluride for different compositions are given in the Table. With increasing content of doping impurity, the thermoelectric power is first increased, and

then drastically decreased, which is due to overrunning of *Bi* solubility region in *SnTe*. Maximum thermoelectric power is achieved with impurity content about 0.3 mol.%, but for condensates prepared on fresh (0001) cleavages of muscovite mica it is much higher than for samples on glass ceramic.

Table

Thermoelectric parameters of vapour-phase condensates based on doped tin telluride of different composition

mol.% *Bi*	σ, $\Omega^{-1}cm^{-1}$	μ, $cm^2/V\cdot s$	*n*, cm^{-3}	*S*, μV/K	$S^2\sigma$, $\mu W/K^2\cdot cm$
Films 0.1 μm thick on fresh (0001) cleavages of muscovite mica					
0	2790	32	$5.44\cdot10^{20}$	55	8.4
0.3	3900	146	$1.67\cdot10^{20}$	90	31.2
1.5	3904	278	$8.78\cdot10^{19}$	65	16.3
2	852	56	$9.56\cdot10^{19}$	131	14.6
Films 0.5 μm thick on fresh (0001) cleavages of muscovite mica 0.5 μm					
0	1414	61	$1.44\cdot10^{20}$	31	1.3
0,3	2780	221	$7.87\cdot10^{19}$	54	8.1
1,5	5501	318	$1.08\cdot10^{20}$	56	17.5
2	674	68	$6.18\cdot10^{19}$	123	10.2
Films 2 μm thick on fresh (0001) cleavages of muscovite mica					
0	1156	74	$9.71\cdot10^{19}$	20	0.5
0,3	2570	242	$6.63\cdot10^{19}$	44	4.9
1,5	5800	323	$1.12\cdot10^{20}$	55	17.7
2	641	71	$5.62\cdot10^{19}$	121	9.3
Films 0.05 μm thick on glass-ceramic substrates					
0	4815	19	$1.55\cdot10^{21}$	64	19.8
0.3	5776	102	$3.54\cdot10^{20}$	62	22.3
1.5	1390	82	$1.05\cdot10^{20}$	80	8.8
Films 0.3 μm thick on glass-ceramic substrates					
0	1844	47	$2.44\cdot10^{20}$	34	2.1
0.3	4129	257	$1.01\cdot10^{20}$	30	3.7
1.5	4398	170	$1.62\cdot10^{20}$	15	0.9
Films 1 μm thick on glass-ceramic substrates 1 μm					
0	1428	60	$1.48\cdot10^{20}$	19	0.5
0.3	3899	289	$8.43\cdot10^{19}$	23	2.1
1.5	4819	174	$1.73\cdot10^{20}$	12	0.7

Figs. 1 – 2 show the thickness dependences of thermoelectric parameters of vapour-phase *SnTe*

condensates with the content of bismuth 0.3 mol.%. It is seen that with reduction of condensate thickness d, irrespective of composition, conductivity grows considerably, and for thicknesses more than $d \approx 0.5$ μm it is practically unvaried. This is related to growth of the concentration of current carriers in the range of small film thicknesses, due to the acceptor effect of surface-adsorbed oxygen. And current carrier concentration for pure telluride is higher than for doped one due to the donor effect of bismuth. With decreasing thickness of films prepared on mica substrates, the Seebeck coefficient is increased as well, which results in considerable increase of thermoelectric power (Fig. 1, *d*).

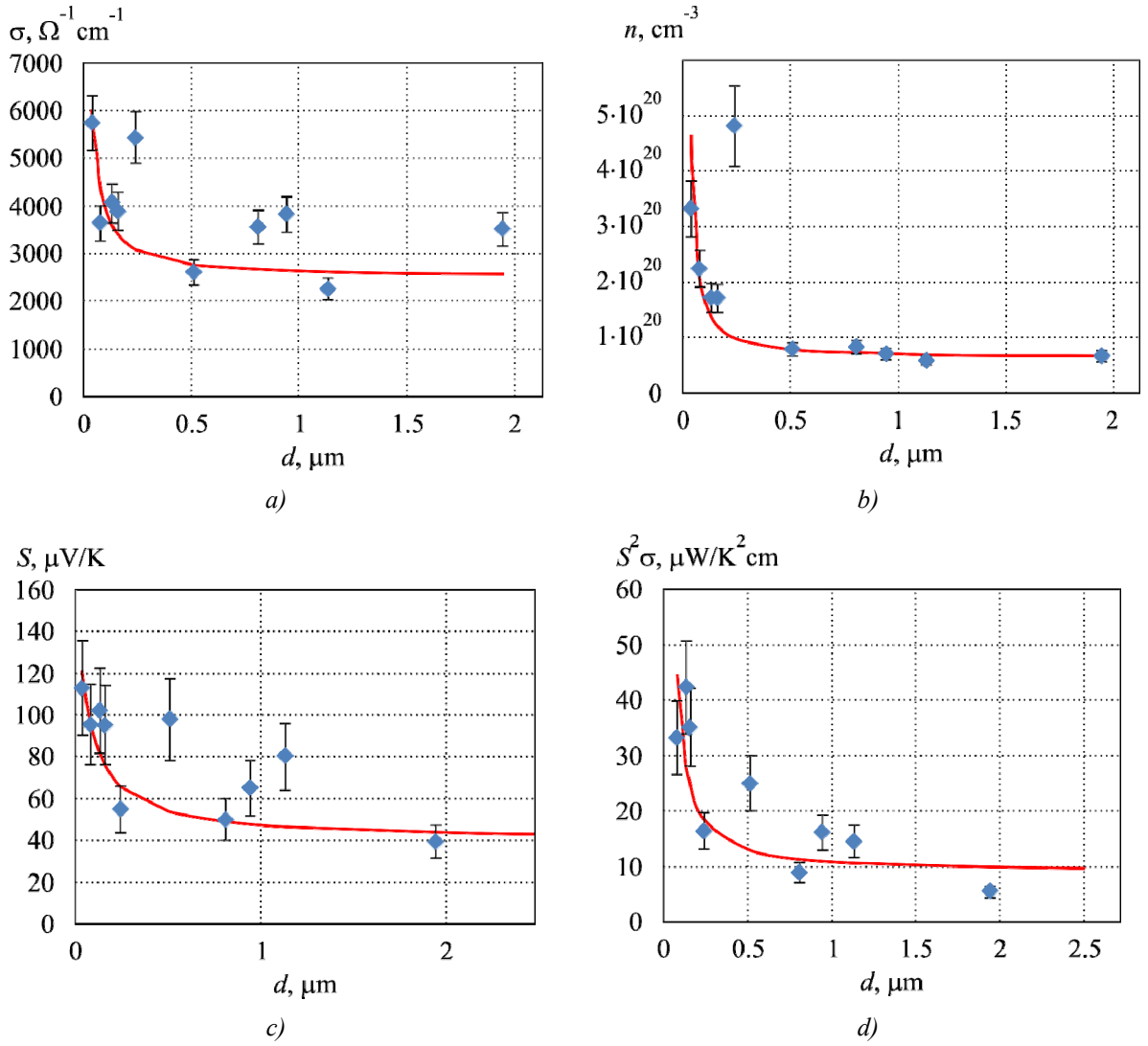

Fig. 1. Dependences of electric conductivity σ (a), the Hall concentration n (b), the Seebeck coefficient S (c) and thermoelectric power $S^2\sigma$ (d) on thickness d of SnTe:Bi films on fresh (0001) cleavages of muscovite mica. The content of Bi is 0.3 mol.%.

Films prepared on fresh (0001) cleavages of muscovite mica are characterized by considerably higher thermoelectric power due to double Seebeck coefficient than samples prepared on glass ceramic (Figs. 1 – 2, *d*), owing to better structural order at the cost of orientation effect of the substrate. For condensates obtained on glass ceramic substrates the thickness dependences of the Seebeck coefficient and thermoelectric power have a distinct maximum in the range of thicknesses ~ 0.6 μm (Fig 2, *c*, *d*) which is due to manifestation of size effects with small condensate thicknesses.

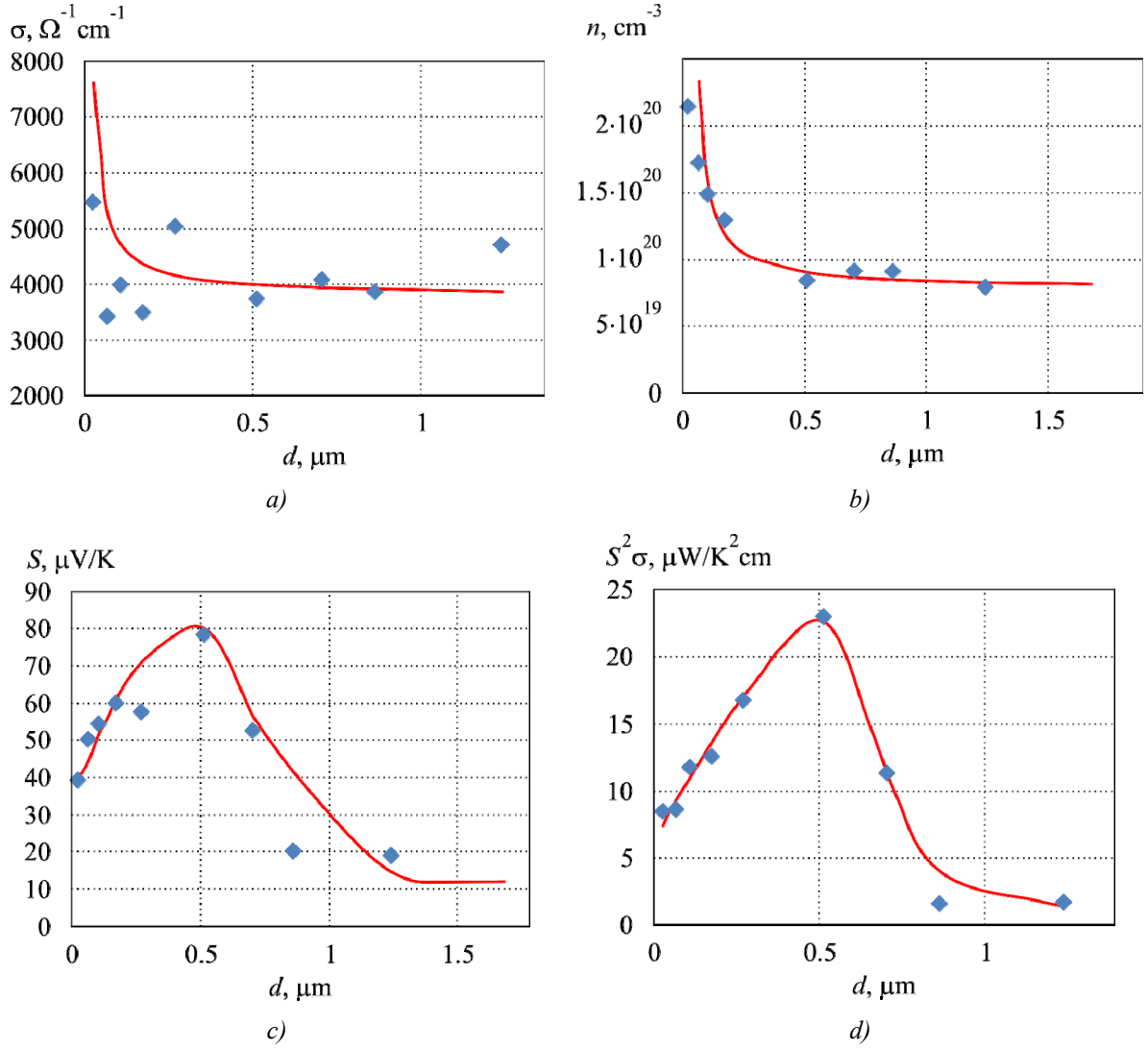

Fig. 2. Dependences of electric conductivity σ (a), the Hall concentration n (b), the Seebeck coefficient S (c) and thermoelectric power $S^2\sigma$ (d) on thickness d of SnTe:Bi films on glass-ceramic substrates. The content of Bi is 0.3 mol.%.

On the whole, high conductivity values combined with considerable Seebeck coefficient value of *SnTe*:*Bi* films yield thermoelectric material of *p*-type conductivity which is promising for construction of film micromodules for thermoelectric power conversion.

Conclusions

1. Thermoelectric properties of vapour-phase thin films of lead telluride doped with bismuth, prepared by vapour-phase methods on glass-ceramic and mica substrates have been studied.
2. It has been shown that *p*-type *SnTe* thin films have improved thermoelectric parameters as compared to the bulk samples.
3. Doping of tin telluride with bismuth, despite some reduction of conductivity allows improving thermoelectric power due to the Seebeck coefficient increase.

The work has been performed in conformity with a comprehensive scientific project of Ukrainian State Foundation for Basic Research (state registration number 0113U003689) and the NAS of Ukraine (state registration number 0110U006281).

References

1. V.M. Shperun, D.M. Freik, and R.I. Zapukhlyak, *Thermoelectricity of Lead Telluride and its Analogs* (Ivano-Frankivsk: Plai, 2000), 250 p.
2. D.M. Freik, M.A. Haluschak, and L.I. Mezhylovska, *Physics and Technology of Thin Films* (Lviv: Vyschaya Shkola, 1988), 182 p.
3. D.M. Freik, I.V. Gorichok, N.I. Dykun, and Yu.V. Lysyuk, Effect of manufacturing technique on the thermoelectric properties of nonstoichiometric and doped lead telluride and solid solutions on its basis, *J. Thermoelectricity* **2**, 42 – 49 (2011).
4. R.L. Petritz, Theory of an Experiment for Measuring the Mobility and Density of Carriers in the Space-Charge Region of a Semiconductor Surface, *Phys. Rev.* **110**, 1254 (1958).

Submitted 30.05.14

A.A. Nikolaeva[1,2], L.A. Konopko[1,2], P.P. Bodiul[1], A.K. Tsurkan[1]

[1]D. Gitsu Institute of Electronic Engineering and Nanotechnologies of the Academy of Sciences of Moldova, 3/3, Academiei Str., Kishinev, MD-2028, Republic of Moldova;
[2]International Laboratory of High Magnetic Fields and Low Temperatures, 95, Gajowicka Str., Wroclaw, 53-421, Poland

PECULIARITIES OF DIFFUSION THERMOPOWER WITH IMPURITY ELECTRON TOPOLOGICAL TRANSITION IN HEAVILY DOPED BISMUTH WIRES

This paper presents a series of investigations of differential thermopower and resistance in the temperature range of 4.2 – 300 K of samples shaped as glass-coated single-crystal Bi wires heavily doped with Sn acceptor impurity. An anomaly in the form of a triple sign change in the temperature dependences of thermopower $\alpha(T)$ is detected. The effect is treated in terms of impurity electron topological transition (ETT), i.e. origination of Σ-band by doping bismuth wires with Sn acceptor impurity. The method of measuring Shubnikov-de-Haas oscillations in the main crystallographic directions in parallel ($H \parallel I$) and perpendicular ($H \perp I$) directions was used to calculate the basic parameters of hole Fermi surfaces at points T and L of the Brillouin zone, which made it possible to estimate the concentration and energy position of Σ-band in Bi and confirm that anomalies observed on traditional dependences of diffusion thermopower are specific features of ETT. The effect can be used for the discovery of ETT in the cases when research on the Fermi surface by oscillation methods is impossible, for instance, with heavy doping and in high-temperature region.

Key words: electronic topological transitions, Shubnikov-de-Haas oscillations, diffusion thermopower, doped bismuth wires.

Introduction

Knowledge of the Fermi surface shape allows determination of many thermodynamic and kinetic characteristics of solids.

The kinetic and thermodynamic characteristics of solids are largely determined by the Fermi surface (FS) shape, since current carriers located in the Fermi layer are nearest to unoccupied states owing to which they are most efficient.

On application of various extreme external influences, namely introduction of isovalent and doping impurities, uniform compression and uniaxial deformations, etc., the Fermi surface can vary not only quantitatively, shrinking or expanding, but also qualitatively. Then the topology of this surface becomes radically different. Qualitative changes in the topology of the Fermi surface can result from change in the composition, for instance, at doping, and with constant composition, for instance, under pressure.

The density of energy states $\nu(\varepsilon) = dN(E)/dE$ of conduction electrons is due to the shape of constant-energy surfaces in momentum space $E(p) = E$. As was demonstrated by Lifshitz [1], the root peculiarity in the density of energy states of conduction electrons $\nu(E) = dN/dE$, occurring at certain

critical values of energy $E = E_k$, whereby FS topology is changed results in the appearance at low temperatures of anomaly in the series of thermodynamic and kinetic characteristics of metals.

In the majority of metals the value of critical energy E_k, where changes of FS topology take place is located sufficiently far from electron chemical potential μ, and the presence of particular points E_k can be judged by *X*-ray spectra. However, if there is any ever changing parameter with a change of which the difference (μ-E_k) passes through zero, i.e. the topology of the boundary Fermi surface is changed, then the peculiarities of spectral density $\nu(E)$ and the dynamics of electrons close to "critical" surface $E(p) = E_k$ lead to peculiar anomalies of thermodynamic and kinetic characteristics of electron gas in metal. Such a continuous parameter can be the level of doping with donor or acceptor impurities.

In [2], using pseudopotential method, calculations were performed for ETT of the type "formation of cavity" and "formation of jumper" in the system of $Li_{1-x}Mg_x$ alloys. It was emphasized that at critical point E_k, alongside with the root peculiarity in the density of states $\nu(E)$, there is a similar peculiarity of electron mean free path *l*. According to [3], this peculiarity occurs in relaxation time τ, so when considering the anomalies of kinetic characteristics, it is necessary to speak of relaxation time, rather than of electron mean free path peculiarities.

Various kinetic coefficients, in particular, electric conductivity σ_e and thermal conductivity χ, are equal to integrals of vector mean free path length $\vec{l}(\vec{p})$ along FS with different weight functions, hence, all of them comprise a peculiarity of the form $(\pm Z)^{1/2}\Theta(\pm Z)$, where $\Theta(Z) = 0$ at $Z < 0$ and $\Theta(Z) = 1$ at $Z > 0$.

Taking into account the expression for the electron part of thermopower α_e [4]:

$$\alpha_e = \frac{\pi^2 T}{3e} \cdot \frac{\partial \ln \sigma_e(E)}{\partial E}\Big|_{E=E_F} \tag{1}$$

the authors of [2, 5] were the first to point to the fact that the anomaly in α_e should be most strongly pronounced:

$$\alpha_e \sim (\pm Z)^{-1/2} \cdot \Theta(\pm Z) \tag{2}$$

At $Z \to 0$ the thermopower at point of ETT is very much increased, and this growth is restricted only by transition blurring.

The characteristic energies of *Bi* are very small. Having small characteristic energies, *Bi* is a representative of substances whose energy spectrum is extremely sensitive to various external influences, namely magnetic field, uniform compression, uniaxial deformations, introduction of doping and isovalent impurities. With the aid of external influences, one can realize in *Bi* various unique cases of mutual arrangement of *L* and *T* bands relative to each other and to the boundary filling energy.

For the bulk samples of *Bi* and $Bi_{1-x}Sb_x$ with impurities, in [6] it was shown that in conformity with theory the kinetic characteristics, namely resistance and thermopower, show an abnormal behaviour at ETT, the anomaly of thermopower, shaped as asymmetric peak, being particularly pronounced. All-round investigation of the anomalies of thermopower and resistance at ETT of all possible types was reliably recorded by means of Shubnikov-de-Haas (SdH) quantum oscillations. It was of interest to study the peculiarities of diffusion thermopower at ETT in *Bi* wires heavily doped with acceptor impurities with a view to discover heavy Σ-band.

Samples, experiment

Thin single-crystal wires were obtained by liquid phase casting by the Ulitovsky method [7, 8].

When casting thin wires of bismuth and its alloys, a single-crystal ingot prepared by zone re-crystallization method served as a source material.

To obtain *Sn*-doped *Bi* wires, the alloys of *Bi*-0.3 at.%, 0.07 and 0.05 at. % *Sn* were synthesized. The wires with concentrations of 0.1 at%, 0.15 at% and 0.2 at% *Sn* were obtained by dilution of alloys comprising 0.3 at% *Sn*. For this purpose, a glass tube with a sealed bottom was filled with several grams of *Bi*-0.3 at% *Sn* alloy, to which pure bismuth was added in estimated quantity necessary for obtaining the required concentration of donor impurity.

Crystallization of microwire strand of bismuth and its alloys occurs with strong overcooling of melt on crystallization front. Thus, for instance, for bismuth, maximum overcooling depth appears at casting rate 10 m/sec and achieves 40 – 50 °C. Strong overcooling and high crystallization rates contribute to growth of single-crystal strand.

Wire diameter $d > 1$ μm was measured by optical microscope Biolam with magnification 1350, as well as calculated by the resistance value at room temperature and the respective resistivity obtained for thicker samples according to expression: $d = \sqrt{\frac{4l}{\pi R_{300}\sigma_{300}}}$, where l is sample length, σ_{300} is conductivity of thick ($d > 1$ μm) wire of corresponding composition of this crystalloghraphic orientation at 300 K, R is sample resistance at 300 K. The error in diameter determination by the calculated method was ≈ 5 – 10 %.

Control diameter measurements were made on scanning electron microscope Vega Tescan 5130 MM.

Test measurements of crystallographic orientation of glass-coated wires were performed with the use of *X*-ray diffraction method. *X*-ray diffraction was performed in diffractometer Xcalibur of company Oxford Diffraction. Diffraction pattern showed that in the area of glass-coated wire illumination (*X*-ray beam diameter 0.5 mm) the nanowire is single-crystal. The instrument permitted to determine orientation of crystal crystallographic planes relative to its external faceting, which made it possible to determine lattice parameters and prove that direction (001) coincides with the wire axis (Fig. 1, insert).

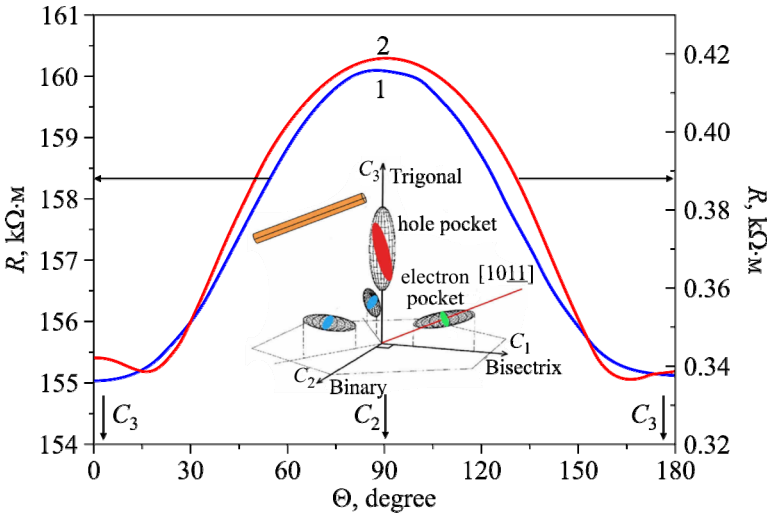

Fig. 1. Diagram of revolution of transverse magnetoresistance of Bi wires doped with Sn: 1. Bi – 0.05at.% Sn, d = 0.6 μ, 2. Bi – 0.1 at.% Sn, d = 1.5 μ, B = 0.5 T, T = 4.2 K. Insert: Schematic of bismuth Fermi surface with respect to wire axis.

Investigations of angular diagrams of revolution of the transverse magnetoresistance (Fig. 1) have confirmed the crystallographic orientation of wires under study, and permitted to orient wire-shaped samples in a magnetic field in such a way that vector $\vec{B}$ coincides with the principal crystallographic axes of the sample. Then Shubnikov-de-Haas oscillations were investigated in the respective direction. At θ = 0 (Fig. 1) magnetic field B is directed along axis C_3, and at θ = 90°, B || along the binary axis C_2.

Measurements were performed in the temperature range of 1.5 – 300 K. Studies of magneto-resistance $R(B)$ and derivative $\delta R/\delta H(B)$ in magnetic fields up to 14 T at temperatures 1.5 – 4.2 K were performed in the International Laboratory of High Magnetic Fields and Low Temperatures, Wroclaw, Poland.

Results and discussion

This paper studies the longitudinal and transverse magnetoresistance and SdH effect in a series of samples shaped as *Bi* wires doped with donor impurity of tin ≥ 0.3 at% *Sn*.

Fig. 2 shows the field dependences of longitudinal magnetoresistance (B || I) at 4.2 K of *Bi* wires with different degree of doping with *Sn*.

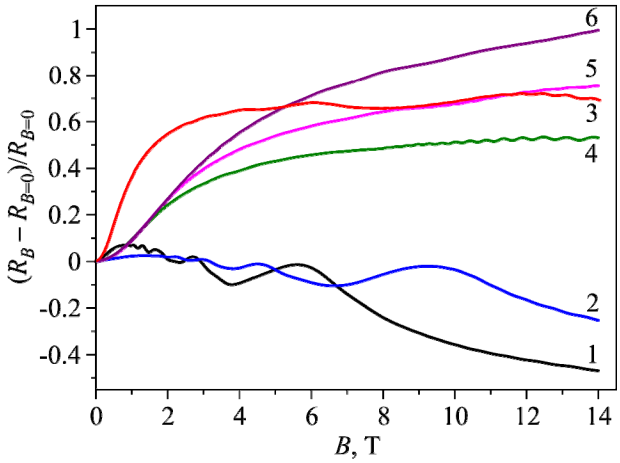

Fig. 2. Field dependences of reduced longitudinal magnetoresistance ΔR/R(B) (B || I) at T = 2.1 K of Bi-Sn wires of various composition: 1. Bi – 0.05 at% Sn, d = 0.6μm; 2. Bi – 0.07 at% Sn, d = 0.6 μm; 3. Bi – 0.1 at% Sn, d = 1.5 μm; 4. Bi – 0.15 at% Sn, d = 0.4 μm; 5. Bi – 0.2 at% Sn, d = 0.2 μm; 6. Bi – 0.3 at% Sn, d = 1.7 μm.

Monotone curves of longitudinal magnetoresistance $\Delta R/R(B)$ are essentially dependent on doping degree. In the wires *Bi* – 0.05 at% *Sn* and *Bi* – 0.07 at% *Sn* one can see the effect of negative magnetoresistance, when wire diameter is less than 1 μm (curves 1, 2, Fig. 2). The presence of negative magnetoresistance in combination with maximum formation on $R(B)$ in weak magnetic fields is primarily due to manifestation of galvanomagnetic size effect discovered earlier in thin wires of pure *Bi* and in *Bi-Sn* alloys with *Sn* concentration up to 0.025 at% [8, 9].

With further doping of N > 0.07 at% *Sn,* the effect of negative magnetoresistance disappears and is not manifested even at diameters 200 nm (curve 5, Fig. 1).

In heavily doped $Bi_{1-x}Sn_x$ wires in the area of weak magnetic fields there is a quadratic growth of resistance followed by saturation area in high magnetic fields up to 14 T with achievement of weak linear growth only in the wires with maximum degree of doping with *Sn* – 0.3 at% (curve 6, Fig. 2).

In all the wires investigated in a longitudinal magnetic field there were registered Shubnikov oscillations due to charge carriers at points *L* and *T* of reduced Brillouin zone in the range of magnetic fields up to 14 T and temperature range of $2.1 < T < 4.2$ K. In the wires *Bi* – 0.05 at% *Sn* and *Bi* – 0.07 at% *Sn* on *R*(*B*), just as on *dR*/*dB*(*B*) (Fig. 3) the amplitude of SdH oscillations due to light *L* holes in weak magnetic fields is sufficiently high even on *R*(*B*), despite the reduction of relaxation time at doping.

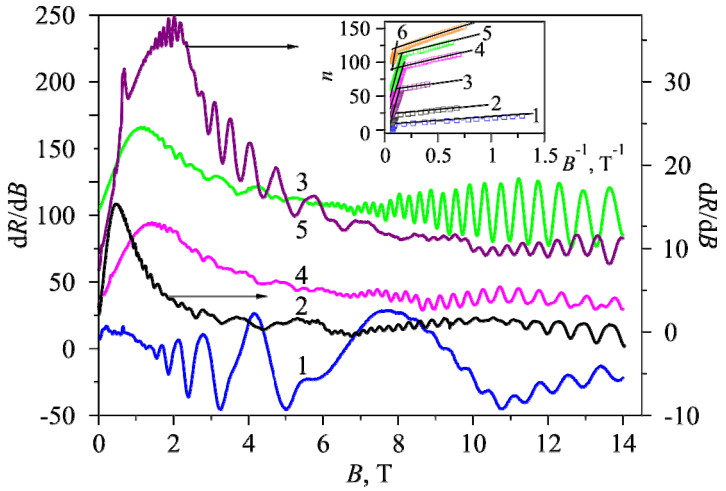

Fig. 3. Field dependences of longitudinal magnetoresistance derivative dR/dB(B) (B || I) at T = 2.1 K of Bi-Sn wires of various composition: 1. Bi – 0.07 at% Sn, d = 0.6 μm; 2. Bi – 0.1 at% Sn, d = 1.5 μm; 3. Bi – 0.15 at% Sn, d = 0.4 μm; 4. Bi – 0.2 at% Sn, d = 0.2 μm; 5. Bi – 0.3at% Sn, d = 1.7 μm. Insert: Dependences of conventional quantum number n of maxima and minima of SdH oscillations of longitudinal magnetoresistance on reverse magnetic field n(B^{-1}).

Insert in Fig. 3 illustrates the dependences of periods of SdH oscillations $\Delta_1(B^{-1})$ and $\Delta_2(B^{-1})$ due to *T*- and $L_{2,3}$-holes, calculated from the linear dependences of quantum number *n* of SdH oscillations due to inverse field $n(B^{-1})$ at different concentrations of *Sn* (in at%).

Period of SdH oscillations due to *T* holes is changed practically by an order from the value $\Delta(B^{-1}) = 0.58 \cdot 10^{-5}$ Oe^{-1} for pure *Bi* to the value $0.055 \cdot 10^{-5}$ Oe^{-1} for the composition *Bi* – 0.05 at% *Sn*. As a result of further increase of *Sn* impurity to 0.3 at%, the period of SdH oscillations is smoothly reduced to $0.032 \cdot 10^{-5}$ Oe^{-1} for the wire *Bi* – 0.3 at% *Sn*.

Similar investigations of the field dependences of the transverse magnetoresistance and SdH oscillations of the wires of all compositions under study were performed in perpendicular magnetic fields when $B \parallel C_2$ ($B \perp I$) and $B \parallel C_3$ ($B \perp I$) (Fig. 4).

In a transverse magnetic field at $B \parallel C_2$ in weak magnetic fields there is a quadratic resistance increase passing to saturation in strong magnetic fields on *R*(*B*) in weakly doped *Bi* wires and to a linear resistance increase in heavily doped *Bi* wires (curves 4, 5, 6 Fig. 4). Maximum resistance increase by 140 – 150 % in magnetic fields up to 14 T occurs in the wires of alloys *Bi* – 0.15 at% *Sn* – *Bi* – 0.2 at% *Sn* (curves 4, 5) which is decelerated at further doping to 0.3 at% *Sn* (curve 6).

In high magnetic fields there are oscillations due to maximum section of *T* holes. With increase in the concentration of *Sn*, the area of existence of SdH oscillations is drastically shifted towards to area of high magnetic fields, reflecting the fact of concentration growth of *T* holes. And for the compositions > 0.1 at% *Sn* the magnetic fields up to 14 T are insufficient to detect SdH oscillations due to maximum section of *T* holes, the area of their existence is shifted to magnetic fields > 14 *T*.

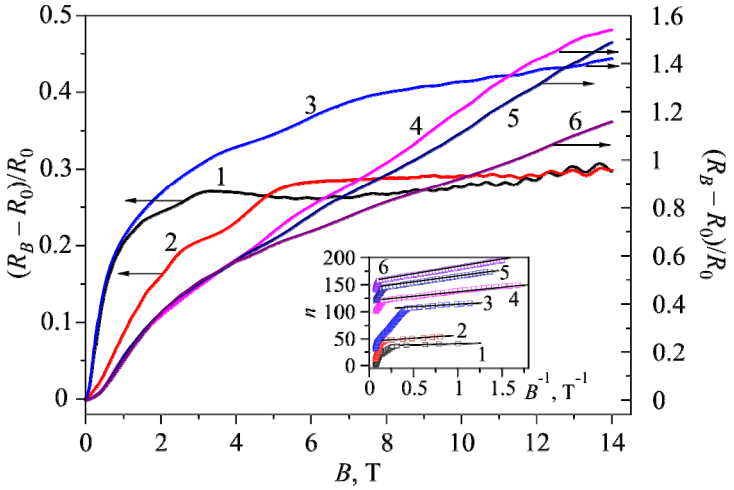

Fig. 4. Field dependences of reduced transverse magnetoresistance ΔR/R(B) (B || C_2) at T = 2.1 K of Bi-Sn wires of various composition: 1. Bi – 0.05 at% Sn, d = 0.6 μm; 2. Bi – 0.07 at% Sn, d = 0.6 μm; 3. Bi – 0.1 at% Sn, d = 1.5 μm; 4. Bi – 0.15 at% Sn, d = 0.4 μm; 5. Bi – 0.2 at% Sn, d = 0.2 μm; 6. Bi – 0.3 at% Sn, d = 1.7 μm. Insert: Dependences of conventional quantum number n of maxima and minima of SdH oscillations on reverse magnetic field n(B^{-1}).

In this direction one can easily see SdH oscillations due to maximum section of L_1-holes and average sections of $L_{2,3}$-hole ellipsoids located symmetrically with respect to a magnetic field $B \parallel C_2$.

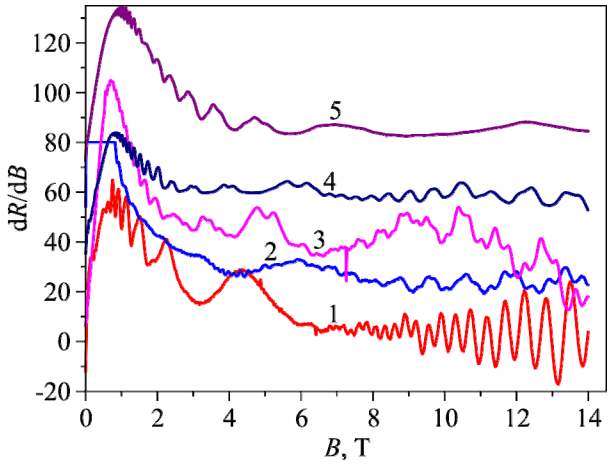

Fig. 5. Field dependences of transverse magnetoresistance derivative dR/dB(B) (B || C_2) at T = 2.1 K of Bi-Sn wires of various composition: 1. Bi – 0.07 at% Sn, d = 0.6 μm; 2. Bi – 0.1 at% Sn, d = 1.5 μm; 3. Bi – 0.15 at% Sn, d = 0.4 μm; 4. Bi – 0.2 at% Sn, d = 0.2 μm; 5. Bi – 0.3 at% Sn, d = 1.7 μm.

As for the case of $B \parallel I$, the greatest change in the periods of SdH oscillations due to both from *L*-holes and *T*-holes was observed in the range of concentrations from pure *Bi* to 0.05 at% *Sn*. A change in the period of SdH oscillations due to maximum section of *L*-holes occurs more smoothly.

At $B \parallel C_3$ ($B \perp I$) there were SdH oscillations due to extreme section of the Fermi surface of *T*-holes close to minimum and the section of *L*-holes close to maximum (Fig. 6, 7).

The specific feature of the field dependences of transverse magnetoresistance at $B \parallel C_3$ at 4.2 K is a drastic quadratic growth of resistance in weak magnetic fields and a transition to linear dependence in high fields. With increase in *Sn* concentration, the area of linear growth of resistance *R*(*B*) is shifted to the area of weaker magnetic fields (curves 3, 4, 5 Fig. 6). As in the case of $B \parallel C_2$, maximum growth of *R*(*B*) was observed in *Bi* wires with the concentration 0.15 – 0.2 at% *Sn*.

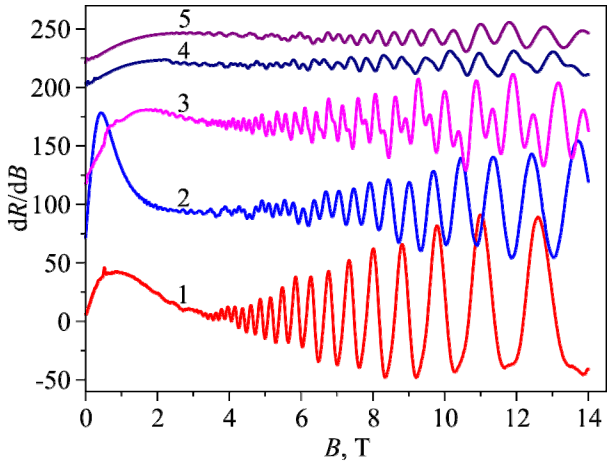

Fig. 6. Field dependences of reduced transverse magnetoresistance ΔR/R(B) (B || C_3) at T = 2.1 K of Bi-Sn wires of various composition: 1. Bi – 0.05 at% Sn, d = 0.6 μm; 2. Bi – 0.07 at% Sn, d = 0.6 μm; 3. Bi – 0.1 at% Sn, d = 1.5 μm; 4. Bi – 0.15 at% Sn, d = 0.4 μm; 5. Bi – 0.2 at% Sn, d = 0.2 μm; 6. Bi – 0.3 at% Sn, d = 1.7 μm. Insert: Dependences of conventional quantum number n of maxima and minima of SdH oscillations on reverse magnetic field n(B^{-1}).

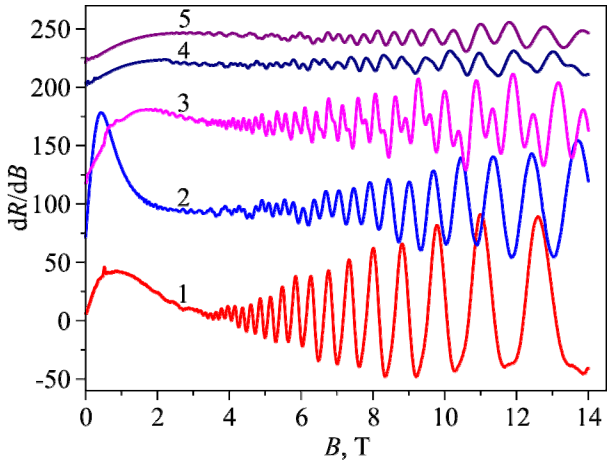

Fig. 7. Field dependences of transverse magnetoresistance derivative dR/dB(B) (B || C_3) at T = 2.1 K of Bi-Sn wires of various composition: 1. Bi – 0.07 at% Sn, d = 0.6 μm; 2. Bi – 0.1 at% Sn, d = 1.5 μm; 3. Bi – 0.15 at% Sn, d = 0.4 μm; 4. Bi – 0.2 at% Sn, d = 0.2 μm; 5. Bi – 0.3 at% Sn, d = 1.7 μm.

Increase in *Sn* concentration to 0.3 at% results in the reduction of periods of SdH oscillations by a factor of 4 – 5.

A combination of investigations of SdH oscillations in *Sn* doped wires in principal crystallographic directions at temperatures 4.2 – 2.1 K allowed calculating the main parameters of the hole surface at *T* and electron surface at *L* at doping with *Sn* donor impurity of *Bi* wires.

For the investigated wires of alloys $Bi_{1-x}Sn_x$ cyclotron masses of extreme maximum and close to minimum sections of the Fermi surface in *T*, were calculated from the temperature dependence of the amplitude of oscillations *R*(*B*) at $B \parallel C_2$ and $B \parallel C_3$ in magnetic fields far from the field of quantum limit where harmonic composition of oscillations is restricted by the first harmonic.

In the case when final temperature T_2 is twofold the initial temperature T_1: $T_2 = 2T_1$, for the cyclotron mass m_c in the quasi-classical range of magnetic fields the following expression was used:

$$m_c = \frac{e\hbar B}{2\pi^2 k T_1 c} \cdot Arcch \frac{A(T_1, B)}{A(T_2, B)}. \quad (3)$$

At T_D = const, ε_F = const: $A(T_1, B)$ is the amplitude of oscillations in field B at $T = T_1$ [10].

The results of calculation of $(m_c^T)_{\max}$ ($B \parallel C_2$) and $(m_c^T)_{\min}$ ($B \parallel C_3$), as well as of mass m_c of sections close to maximum at point T are given in Table 1.

Table 1

The main parameters of the hole Fermi surface at T and the hole Fermi surface at L of investigated Bi-Sn wires with standard orientation (1011) along wire axis in a parallel magnetic field (B || I)

Composition	d, μm	$R_{300}/R_{4.2}$	η_{Sn}	*T*-holes					*L*-holes			
				$\Delta_1(B^{-1})$, 10^{-5} Oe^{-1}	f_1^T, T	m_c^T / m_0	ε_F^T, meV	p^T, 10^{17} cm^{-3}	$\Delta_2(B^{-1})$, 10^{-5} Oe^{-1}	$f_2^{L_{2,3}}$, T	m_c^L/m_0	p^L, 10^{17} cm^{-3}
Bi – 0.05 at% *Sn*	0.6	4.7	0.85	0.055	181.8	0.195	100	116	1.8	5.5	0.033	7.47
Bi – 0.07 at% *Sn*	0.6	4.14	0.7	0.052	194.1	0.224	103.6	120	1.15	8.7	0.034	14.9
Bi – 0.1 at% *Sn*	1.5	8.8	0.6	0.042	240	0.299	117	160	0.85	11.6	0.054	23.1
Bi – 0.2 at% *Sn*	0.2	6.4	0.4	0.041	243	0.311	122	178	0.42	23.8		67.4
Bi – 0.3 at% *Sn*	1.7	7	0.33	0.036	277	0.336	134	210	0.35	28.5	0.0687	88.3

$\Delta_1(B^{-1})$ and f_1^T is period and frequency of SdH oscillations due to close to maximum section $S^T_{\max}$ of the hole Fermi surface at point T ($B \parallel I$); $\Delta_2(B^{-1})$ and $f_2^{L_{2,3}}$ is period and frequency of SdH oscillations due to two equivalent average sections $S^L_{2,3}$ of the hole Fermi surfaces at point L; m_c^T is close to maximum cyclotron mass of holes at point T; m_c^L is cyclotron mass of charge carriers at point L corresponding to average sections $S^L_{2,3}$ of the Fermi surface; ε_F^T is the Fermi energy of holes at point T, calculated in the two-band approximation at ε_g^T = 200 meV; p^T and p^L is hole carrier concentration at points T and L; η_{Sn} is efficiency factor.

Similar calculations were also performed for holes at point L of the Brillouin zone. In some cases, in particular, in the wires of alloys *Bi* – 0.2 at% *Sn* and *Bi* – 0.3 at% *Sn* at $B \parallel C_3$ due to abnormal temperature dependence of the amplitude of SdH oscillations, we did not manage to calculate the cyclotron masses of holes corresponding to minimum section of the Fermi surface of holes at T.

The Dingle temperature T_D for T-holes, as well for L-holes, was determined from the amplitude ratio of SdH oscillations of two consecutive values B_n and B_{n+1}, whereby there are minima and maxima of magnetoresistance according to expression [4].

The calculated values of T_D made 5 – 7 K and did not show a distinct dependence on the composition in the concentration range > 0.05 at% *Sn*.

It was established that the cyclotron masses of T-holes and L-holes grow with increased doping with *Sn* donor impurity. This fact points to spectrum nonparabolicity of not only L-holes, but also T-holes. A similar effect was observed in the bulk samples of *Bi* on doping with tin to concentrations

corresponding to position of the Fermi level of *T*-holes $\varepsilon^T_F = 90$ meV [10].

The Fermi energy ε^T_F of *T*-holes was calculated by the two-band model (ellipsoidal nonparabolic model) by means of expression [11]:

$$\varepsilon^T_F = \varepsilon_{nap} - \frac{1}{2}\varepsilon^T_g + \left[\varepsilon^2_{nap} + \left(\frac{1}{2}\varepsilon^T_g\right)^2\right]^{1/2} \tag{4}$$

$\varepsilon_{nap} = \dfrac{eh\cdot\Delta_T^{-1}}{2\pi c\cdot m^T_c}$, where ε_{nap} is the energy in the approximation of a parabolic band, $\varepsilon_F{}^T$ is the Fermi energy of *T*-holes counted down from the band ceiling at *T*, $m_c{}^T$ is small cyclotron mass of *T*-holes; $\varepsilon_g{}^T$ is a gap at point *T* of the Brillouin zone which according to [11, 12] is equal to 200 meV; $\Delta_T{}^{-1}$ is the value of reverse period of SdH oscillations from the smallest section of hole ellipsoid at *T* point of the Brillouin zone.

From the calculated values of $\varepsilon_F{}^T$ it follows that on doping of *Bi* wires with tin to 0.3 at%, the position of the Fermi level of holes $\varepsilon_F{}^T$ achieves the value ≈ 134 meV, i.e. practically increased by an order as compared to pure bismuth ($\varepsilon_F{}^T = 12$ meV).

The concentration of *T*-holes was calculated by the experimental data of periods of SdH quantum oscillations using the relation [13]:

$$p^T = \frac{1}{3\pi^2}\left(\frac{2e}{\hbar c}\right)^{3/2}\cdot\left(\frac{1}{\Delta_1\Delta_2\Delta_3}\right)^{1/2} \tag{5}$$

where Δ_1, Δ_2, Δ_3 are periods of SdH oscillations in the three main directions of ellipsoid.
Due to the fact that in the investigation of SdH oscillations at $B \parallel C_3$ there were registered oscillations from sections close to minimum (since wire axis makes an angle ~ 20° with the bisector axis $C_{1/2}$), the value of minimum inverse period of *T*-holes in the wires was determined from the ratio $\left(\Delta_T\right)^{-1}_{\min} = \dfrac{\left(\Delta_T^{-1}\right)^d}{2.5}$, where $\left(\Delta_T^{-1}\right)^d$ is the frequency of Shubnikov oscillations of holes in T wires with orientation (10$\underline{1}$1) along the axis in a longitudinal magnetic field. In so doing, it was taken into account that the anisotropy of hole Fermi surface in *T* makes $\dfrac{S_{\max}}{S_{\min}} = 3.2$, and as was shown by the authors of [11] on the bulk *Bi* samples, it is changed at doping with *Sn* to concentration 10^{19} cm^{-3}.

The concentration of carriers of *L*-holes was calculated from the expression:

$$\frac{p^L_{Bi}}{p^L_{alloy}} = \frac{\left(\Delta_1^{-1}\cdot\Delta_2^{-1}\cdot\Delta_3^{-1}\right)^{1/2}_{Bi}}{\left(\Delta_1^{-1}\cdot\Delta_2^{-1}\cdot\Delta_3^{-1}\right)^{1/2}_{Bi-Sn}} = \left(\frac{\Delta^{-1}_{i\ (Bi)}}{\Delta^{-1}_{i\ (Bi-Sn)}}\right)^{3/2}. \tag{6}$$

using as a reference point the concentration of electrons in bismuth at 4.2 K $p = 3\cdot10^{17}$ cm^{-3}. [13] Here, the nonspecularity of hole and electron spectra at point *L* was disregarded. Such inaccuracy has a slight impact on the value of tin efficiency factor η_{Sn}, since η_{Sn} is largely determined by the concentration of impurity holes in *T* ellipsoid.

It is known that total concentration of holes in multiband alloys is determined by the concentration of doping tin impurity C_{Sn} (at%):

$$\Sigma p_i = N_A\cdot\rho_{BiSn}\cdot C_{Sn}\cdot\frac{\eta}{A_{BiSn}}\cdot 100 \tag{7}$$

where N_A is the Avogadro number, ρ and A is the density and atomic weight of *BiSn* alloy.

Comparison of the concentration of holes found from SdH oscillations and calculated by the concentration of doping impurity C_{Sn} for the wires of corresponding composition allowed to determine the efficiency factor η of tin doped wires under study. Factor η is equal to the ratio between excess concentration of charge carriers created by impurity atoms and total concentration of introduced impurity atoms. It turned out that the efficiency factor of tin in glass-coated $Bi_{1-x}Sn_x$ wires obtained by the Ulitovsky method is reduced with increase in *Sn* concentration from the value 0.85 for the wires *Bi* – 0.05 at% *Sn* to 0.3 for the wires *Bi* – 0.3 at% *Sn* and is much in excess of the value η_{Sn} obtained on the bulk samples of $Bi_{1-x}Sn_x$ of respective composition [14-18]. The latter is apparently related to peculiarities of pulling glass-coated single-crystal wires by the Ulitovsky method. Owing to high rates of wire crystallization from the melt which is maintained at high temperature and intensively agitated by electromagnetic field of high-frequency inductor, *Sn* impurity is uniformly distributed, eliminating the possibility of clusters formation in the bulk of the wire pulled from the melt. Therefore, homogeneous single-crystal wires of $Bi_{1-x}Sn_x$ were obtained to concentration 0.3 at% *Sn*. As was shown in [19], the presence of impurity states in doped *Bi* samples leads to a reduction of efficiency factor with a rise in temperature, and at 4.2 K $\eta \approx 1$ and does not depend on concentration, though in the experiments in the bulk samples $\eta << 1$.

The temperature dependences of relative resistance $R_T/R_{300}(T)$ of tin doped bismuth wires in the temperature range of 4.2 – 300 K are illustrated in Fig. 8. With increase in *Sn* concentration above 0.07 at%, the curves $R(T)$ are smooth and identical up to concentration $2.1 \cdot 10^{19}$ cm^{-3}. At *Sn* concentrations 0.07 at%, the size effect in dependences $R_T/R_{300}(T)$ is manifested in displacement of maximum on $R(T)$ to higher-temperature region.

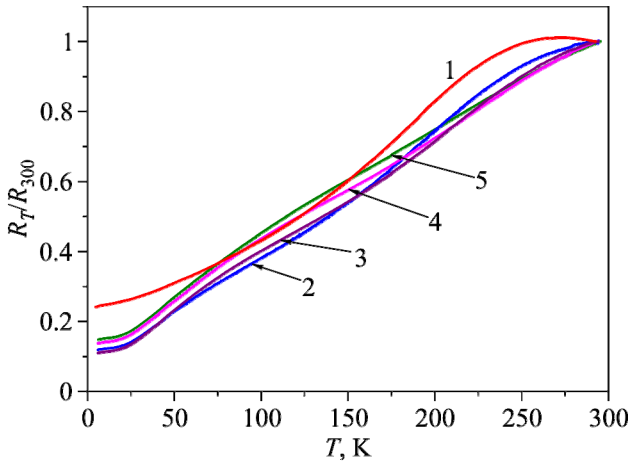

Fig. 8. Temperature dependences of relative resistance $R_T/R_{300}(T)$ of Bi-Sn wires:
1. Bi – 0.07 at% Sn d = 0.3 μm, 2. Bi – 0.1 at% Sn d = 0.9 μm, 3. Bi – 0.15 at% Sn d = 1.1 μm,
4. Bi – 0.2 at% Sn d = 0.6 μm, 5. Bi – 0.3 at% Sn d = 0.9 μm.

The temperature dependences of thermopower α(T) of *Sn* doped bismuth wires are represented in Fig. 9.

For the first time, essential non-monotonous dependence of α(T) with a triple change of thermopower sign in heavily doped alloys (0.1; 0.15; 0.2 at% *Sn*) was discovered. In the alloys with concentration $2.1 \cdot 10^{19}$ cm^{-3} (*Bi* – 0.3 at% *Sn*) the thermopower has positive meaning in the entire temperature range, though curve α(T) is non-monotonous, retaining the peculiarities of curves 2, 3, 4 including change of sign α (Fig. 9).

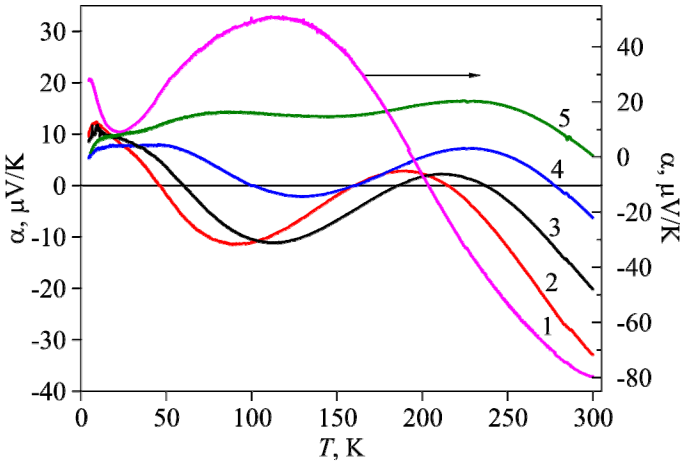

Fig. 9. Temperature dependences of thermopower α(T) of BiSn wires of various composition: 1. Bi – 0.07 at% Sn d = 1.5 μm, 2. Bi – 0.1 at% Sn d = 0.9 μm, 3. Bi – 0.15 at% Sn d = 1.1 μm, 4. Bi – 0.2 at% Sn d = 0.6 μm, 5. Bi – 0.3 at% Sn d = 0.9 μm.

The temperature dependence $\alpha(T)$ for the wires with concentration 0.07 at% *Sn* has a positive maximum in the temperature region 80 – 140 K, following which the thermopower is reduced, remaining in the positive region with temperature reduction to 4.2 K (Fig. 9).

Similar temperature dependences were observed on the bulk samples of $Bi_{1-x}Sn_x$ at concentrations up to 0.26 at% *Sn* [16]. However, on the bulk samples there was no double change of thermopower sign, though the general tendency of thermopower sign change from (–) to (+) with increase in *Sn* concentration took place.

The most interesting effect is a triple change of thermopower sign that was observed in $Bi_{1-x}Sn_x$ wires in the concentration range of $1.6 \div 1.78 \cdot 10^{19}$ cm^{-3} with formation of negative polarity extreme on $\alpha(T)$ in the temperature range of 80 to 100 K. Here it must be emphasized that only holes (light at *L* and heavy at *T*) take part in transition phenomena, and thermopower should be positive. While the first change of sign with temperature reduction from 300 K (in high temperature region) is logical and reflects the fact of intensification of hole contribution to α on doping, the following abnormal change calls for special consideration.

With the contribution to thermopower of two groups of holes: light *L* and heavy *T* or Σ, the total thermopower is determined by the expression:

$$\alpha = \frac{\alpha_L \cdot \sigma_L + \alpha_{T,\Sigma} \cdot \sigma_{T,\Sigma}}{\sigma_L + \sigma_{T,\Sigma}} \qquad (8)$$

where α_L, $\alpha_{T,\Sigma}$, σ_L, $\sigma_{T,\Sigma}$ are partial values of thermopower and electric conductivity of light and heavy holes. The conductivity of heavy *T* or Σ-holes as compared to conductivity of light *L*-holes in the first approximation can be neglected, since mobilities $\mu_{T,\Sigma} << \mu_L$. Therefore, total thermopower for $Bi_{1-x}Sn_x$ alloys is mainly determined by partial thermopower α_L whose value at investigated temperatures is due to operating mechanisms of charge carrier scattering. If hole scattering in *p*-type alloys is only intraband, then, according to theory, the sign of thermopower should be positive.

Thermopower behaviour (change of sign from (+) to (–) and then from (–) to (+) with temperature reduction) allows concluding that thermopower anomaly is related to additional nonintraband scattering mechanism. For light L_S-holes in multi-band alloys such additional scattering mechanism can be elastic scattering of carriers from *L*-band to Σ-band appearing with a displacement of $\varepsilon_F{}^T$ at doping with *Sn*. Further increase in the concentration of impurity holes in the wires of $Bi_{1-x}Sn_x$

alloys leads to anomaly reduction (curve 4), and with heavy doping levels thermopower has a positive meaning and the anomaly disappears (curve 5), which is typical of electron topological transition.

In this case, with electron topological Lifshitz transition $\alpha \sim Z^{-1/2}$, where $Z = (\varepsilon - \varepsilon_k)$ is transition parameter according to theory, thermopower anomaly should be negative, since in the presence of additional scattering channel for the "hot" carriers such as holes in *L* and *T*-bands, thermopower must reduce and can even change sign (negative anomaly).

Thus, electron topological transition occurs when doping *Bi* wires with *Sn* acceptor impurity at concentration $N_c = 1.6 \div 1.8 \cdot 10^{19}$ cm^{-3}, and the estimated energy position of Σ-band corresponds to the Fermi energy value of *T*-holes $\varepsilon_F^T = 115$ to 120 meV.

Note that a similar topological transition with a change of thermopower sign on $\alpha(T)$ was observed in $Bi_{1-x}Sb_x$ alloys doped with *Sn* impurity [12, 20, 21]. The authors also treated this effect from the standpoint of electron topological transition with the origin of Σ-band.

Conclusions

Integrated research of SdH oscillations in the main crystallographic directions of the electrical and thermoelectric properties of single-crystal glass-coated bismuth wires doped with *Sn* acceptor impurity in the temperature range of 1.5 to 300 K is performed. The $\alpha(T)$ dependences are essentially non-monotonous with a triple change of sign in the temperature range of 4.2 – 300 K. Effect of formation of a negative polarity extremum and a double change of sign on $\alpha(T)$ at lower than 200 K temperatures in *Bi-Sn* wires is treated in terms of impurity electron topological Lifshitz transition with heavy doping of bismuth wires with tin. Calculations of the basic parameters of the Fermi surfaces at points *L* and *T* of the Brillouin zone from SdH oscillations allowed estimating the concentration $N_p = 1.6 \div 1.8 \cdot 10^{19}$ cm^{-3} and the energy position of Σ-band $\varepsilon_F^T = 115 - 120$ meV.

This work was performed with support of grant Moldova-Belarus 13.820.05.12/BF.

References

1. I.M. Lifshitz, On the Anomalies of Electronic Characteristics of Metals in the Area of High Pressures, *JETF* **38** (5), 1569 – 1576 (1960).
2. V.G. Vaks, A.V. Trefilov, and S.V. Fomichev, On the Peculiarities of Electric Resistance and Thermopower of Metals with 2 ½ Order Phase Transitions, *JETF* **80** (4), 1613 – 1621 (1981).
3. A.A. Abrikosov, A.V. Pantsulaya, On the Peculiarities of Thermopower with the Lifshits Topological Transition, *Physics of the Solid State* **28** (7), 2140 – 2144 (1986).
4. E.M. Lifshits, L.P. Pitayevsky, *Physical Kinetics* (Moscow: Nauka, 1979), 527 p.
5. A.A. Varlamov, A.V. Pantsulaya, Gigant Thermoelectric Power in Metals in the Vicinity of 2 1*2 Order Phase Transition, *Solid State Communications* **56** (9), 787 – 790 (1985).
6. N.B. Brandt, V.S. Yegorov, M.Yu. Lavreniuk, N.Ya. Minina, and A.M. Savin, Peculiarities of Thermopower and Resistance with Electronic Topological Transitions in Bismuth and its Alloys, *JETF* 89, **6** (12), 2257 – 2269 (1985).
7. D. Gitsu, L. Konopko, A. Nikolaeva, and T. Huber, Pressure Dependent Thermopower of Individual Bi Nanowires, *Applied Physics Letters* **86**, 10210 (2005).
8. A.A. Nikolaeva, L.A. Konopko, A.K. Tsurkan, and T.E. Huber, Thermoelectric Properties of Single-Crystal *Bi-Sn* Wires with Different Crystallographic Orientation at Elastic Strains, *J. Thermoelectricity* **3**, 41 – 59 (2009).

9. N.B. Brandt, D.V. Gitsu, A.A. Nikolaeva, and Ya.G. Ponomarev, Investigation of Size Effects of Thin Cylindrical Bismuth Single Crystals Located in a Magnetic Field, *JETF* **72** (6), 2332 – 2344 (1977).
10. N.B. Brandt, S.M. Chudinov, *Experimental Methods of Research on the Energy Spectra of Electrons and Phonons in Metals* (Moscow: Moscow University Publ., 1983), 408 p.
11. N.B. Brandt, R. Muller, and Ya.G. Ponomarev, Study of the Law of Carriers Dispersion in Bismuth Doped with Acceptor-Type Impurities, *JETF* **71**, 6 (12), 2268 – 2277 (1976).
12. N.A. Redko, N.A. Rodionov, *Letters to JETF* **42** (6), 246 (1985).
13. V.S. Edelman, Properties of Electrons in Bi, *Advances in Physical Sciences* **123**, 257 – 281 (1977).
14. J. Heremans, O.P. Hansen, Temperature Dependence of Excess Carrier Density and Thermopower in Tin-Doped Bismuth. Pseudo-Parabolic Model, *J. Phys. C: Solid State Phys*. **16**, 4623 – 4636 (1983).
15. P.P. Bodiul, A.S. Fedorko, and D.V. Gitsu, Thermo- and Magnetothermoemf in *Bi-Sn* Alloys, *Phys. Stat. Sol.* **1a** (2), p. K77 – K80 (1970).
16. J. Boxus, J. Heremans, J.-P. Michenaud, and J.-P. Issi, The Low-Temperature Thermoelectric Properties of Tin-Doped Bismuth, *J. Phys. F: Met. Phys*. **9** (12), 2387 – 2398 (1979).
17. C. Uher, J.L. Opsal, *Phys. Rev. Lett.* 40, 1518 (1978).
18. J.M. Noothoven van Goor, Donors and Acceptors in Bismuth, *Phil. Res. Rep. Suppl*. 4, 91 (1971).
19. V.F. Garabazhiu, On the Theory of the Impurity Structural Transitions in Weakly Degenerate Systems, *Phys. Lett. A* **112** (1, 2), 38 – 39 (1985).
20. N.A. Redko, N.A. Rodionov, Topological Phase Transitions in $Bi_{1-x}Sb_x$ Alloys and Position of Heavy-Hole Band Versus Composition, *Letters to JETF* **42** (6), 246 – 249 (1985).
21. N.A. Redko, V.I. Belitsky, V.V. Kosarev, N.A. Rodionov, and V.I. Polshin, Heavy-Hole Bands and Thermopower Sign in *Bi-Sb* Alloys, *Physics of the Solid State* **28** (12) (1986).
22. O.S. Griaznov, G.A. Ivanov, B.Ya. Moyzhes, V.N. Naumov, V.A. Nemchinsky, N.A. Rodionov, and N.A. Redko, Influence of Interband Scattering Mechanism on the Kinetic Effects in *p*-$Bi_{1-x}Sb_x$, *Physics of the Solid State* **24** (8), 2335 – 2343 (1982).

Submitted 18.06.14

E.M. Godzhayev, J.I. Guseinov

E.M. Godzhayev

[1]Azerbaijan Technical University, 25, Huseyn Javid Ave., Baku, AZ1073, Republic Azerbaijan
[2]Azerbaijan State Pedagogical University, Uzeir Hajibeyov Str., 34, Baku, Azerbaijan

PHYSICO-CHEMICAL ANALYSIS AND THERMOELECTRIC PROPERTIES OF $(SnSe)_{1-x}(ErSe)_x$ SYSTEM ALLOYS

J.I. Guseinov

In this paper, a diagram of state of SnSe-ErSe system has been constructed, and SnSe based solubility in this system has been established. Atomic-force microscope has been used to study surface microrelief of SnSe single crystal, X-ray phase analysis has been performed and the temperature dependences of the electric conductivity, the Hall coefficient, the Seebeck coefficient and the thermal conductivity of $(SnSe)_{1-x}(ErSe)_x$ *system alloys have been investigated.*

Key words: $(SnSe)_{1-x}(ErSe)_x$ system, atomic-force microscope, thermoelectric figure of merit, X-ray phase analysis.

Introduction

Chalcogenides of *SnX* type hold a special place among semiconductor compounds. These compounds possess switching properties, are high pressure sensors and valuable thermoelectric materials [1-3].

Selenium and tin solid solutions also possess high thermoelectric figure of merit and photosensitivity [3-5]. Information is found in the literature on the research of *Sn-Ln-X* (*Ln = La – Lu*; *X = S*, *Se*, *Te*) systems, where it is revealed that substitution solid solutions are formed in these systems close to *SnX* [6, 7]. In particular, physicochemical and X-ray phase analyses in the concentration range of 0 – 10 *ErSe* have established that in this system the solubility of *ErSe* in *SnSe* at 600 °C makes 6.3 mol. %, and at 900 °C - 5 mol. %. However, phase analysis in a wider concentration range and investigation of alloy properties has not been performed. In this connection, the purpose of this paper is physicochemical analysis, study of surface microrelief, research on the thermoelectric properties of *SnSe – ErSe* system alloys.

Experimental

In the synthesis of ternary alloys of *SnSe-ErSe* system, special purity elements were employed as the source components, namely “B4-000” tin, “OC417-4” selenium and chemically pure elemental erbium “ER-2”.

To construct a diagram of state, alloys were prepared that comprised components in different ratios (with the interval 5 mol.%) of weight 2 g.

Calcined aluminium oxide was used as a reference for differential recording. The rate of samples heating and cooling was 0.5 K/s. The temperatures in the construction of the diagram of state were determined to an accuracy of 2 – 2.5 K.

The alloys of *SnSe-ErSe* system were synthesized of the source components in evacuated to 0.1333 Pa quartz ampoules. Synthesis took place in two steps: at first the ampoules with the substance were heated at a rate of 4 – 5 degrees/min to selenium melting point and held at this temperature for 3 – 4 hours, following which the temperature was increased to 950 – 1000 °C depending on the composition and held for 8 – 9 hours. Homogenizing annealing of the resulting samples was performed at 580 °C for 120 hours.

Synthesized samples for differential thermal analysis and electrophysical investigations were subject to homogenizing annealing for 100 – 110 hours depending on the composition, namely annealing was increased with increasing erbium content.

Differential thermal analysis of the samples was done on a low-frequency thermal recorder NTR- 73 with a chromel-alumel thermocouple. Heating rate was 8 degrees/min.

X-ray phase analysis was done on a diffractometer DRON-3 with CuK_α-radiation and nickel filter.

The microhardness of alloys was determined by metallographic method on PMT-3 under the loads selected as a result of studying microhardness measurement for each phase as a function of load. The density of alloys was determined by picnometer and X-ray methods, with toluene used as filler.

Discussion of the results

The resulting alloys are compact, with metallic lustre, and with increasing erbium content their colour becomes dark grey and changes to black. The alloys are resistant to air and water. They are decomposed by concentrated mineral acids (*HCl*, HNO_3, H_2SO_4) and alcali (*NaOH*, *KOH*), whereas organic solvents have no effect on them.

The results of differential thermal analysis of *SnSe-ErSe* system alloys have shown that all fixed effects on heating and cooling curves are reversible.

As a result of microstructure study, a restricted solubility area was detected close to *SnSe.* To confirm the area boundary of solid solutions based on *SnSe*, extra alloys comprising 3, 4, 5 and 6 mol.% *ErSe* were synthesized. The alloys were annealed at 760 °C for 160 hours, and then hardened.

According to the results of microstructural analysis, the solubility of *ErSe* in *SnSe* at room temperature is 5 mol.%, and at temperature close to eutectic point it comes to 10 mol.%. In the range of 5 – 40 mol.% of *ErSe* all the alloys are two-phase. X-ray phase analysis of the alloys (Table 1) has shown that on the diffractograms in the concentration range of 0 – 5 mol.% *ErSe* the diffraction maxima are identical.

With increasing erbium content in *SnSe*, on the diffractograms of alloys there appear new, uncharacteristic of *SnSe,* maxima that are related to *ErSe*.

Table 2 gives some data of physicochemical analysis. As can be seen from the table, in the alloys from solid-solution range, with increase in erbium concentration, the microhardness is increased (480 – 620MPa). The density of alloys from solid-solution range is monotonously increased.

Based on the results of integrated physicochemical analyses, a microdiagram of *SnSe-ErSe* system was constructed (Fig. 1) As it follows from Fig. 1, the system liquidus consists of two parts. In the concentration range of 0 – 10 mol.% *ErSe,* α-phase is primarily crystallized from the liquid (*SnSe* based solid solutions). Then *ErSe* phase is crystallized from the liquid. Two-phase alloys (α + *ErSe*) are crystallized below the liquidus line.

Table 1

Results of X-ray phase analysis of $Sn_{1-x}\varepsilon_{rx}Se$ alloys

Hkl	Θ	d_{theor}, Å	d_{exp}, Å	I/I_0	Θ	d_{theor}, Å	d_{exp}, Å	I/I_0	Θ	d_{theor}, Å	d_{exp}, Å	I/I_0	Θ	d_{theor}, Å	d_{exp}, Å	I/I_0	Θ	d_{theor}, Å	d_{exp}, Å	I/I_0
	SnSe $a = 4.46$; $b = 4.19$; $c = 11.57$ Å				$Sn_{0.99}\varepsilon_{r0.01}Se$ $a = 4.468$; $b = 4.206$; $c = 11.59$ Å				$Sn_{0.98}\varepsilon_{r0.02}Se$ $a = 4.471$; $b = 4.221$; $c = 11.60$ Å				$Sn_{0.97}\varepsilon_{r0.03}Se$ $a = 4.477$; $b = 4.229$; $c = 11.61$ Å				$Sn_{0.96}\varepsilon_{r0.04}Se$ $a = 4.481$; $b = 4.236$; $c = 11.62$ Å			
1	2	3	4	5	6	7	8	9	10	11	12	13	14	15	16	17	18	19	20	21
101	$10^0 42`$	4.1615	4.1605	10	$10^0 41`$	4.1691	4.1604	9	$10^0 39`$	4.1718	4.1724	8	$10^0 39`$	4.1775	4.1782	7	$10^0 37`$	4.1810	4.1822	5
102	$12^0 36`$	3.5321	3.5316	68	$12^0 35`$	3.5388	3.5391	59	$12^0 34`$	3.5411	3.5432	56	$10^0 39`$	3.5458	3.5466	53	$12^0 33`$	3.5487	3.5496	49
110	$14^0 12`$	3.0537	3.0534	3	$14^0 35`$	3.0625	3.0611	3	$14^0 32`$	3.0692	3.0704	3	$10^0 39`$	3.0743	3.0749	3	$14^0 30`$	3.0782	3.0794	3
111	$15^0 08`$	2.9526	2.9523	16	$15^0 3`$	2.9609	2.9700	11	$15^0 3`$	2.9671	2.9402	9	$10^0 39`$	2.9717	2.9727	7	$15^0 01`$	2.9757	2.9763	5
004	$15^0 27`$	2.8925	2.8924	100	$15^0 26`$	2.8985	2.8974	93	$15^0 24`$	2.9002	2.9016	90	$10^0 39`$	2.904	2.9016	87	$15^0 23`$	2.9060	2.9069	85
113	$18^0 47`$	2.3941	2.3939	11	$18^0 43`$	2.4002	2.4032	8	$18^0 42`$	2.4040	2.4048	6	$10^0 39`$	2.4077	2.4085	5	$18^0 38`$	2.4102	2.4114	4
201	$20^0 37`$	2.1897	2.1907	2	$20^0 34`$	2.1936	2.1944	2	$20^0 33`$	2.1951	2.1960	2	$10^0 39`$	2.1980	2.1988	2	$20^0 29`$	2.2000	2.2041	2
202	$21^0 45`$	2.0807	2.0814	5	$21^0 41`$	2.0845	2.0863	3	$21^0 41`$	2.0859	2.0866	3	$10^0 39`$	2.0887	2.0896	3	$21^0 38`$	2.0905	2.0912	2
105	$21^0 58`$	2.054	2.0611	2	$21^0 59`$	2.0581	2.0592	2	$21^0 59`$	2.0594	2.0591	2	$10^0 39`$	2.0620	2.0634	2	$21^0 56`$	2.0636	2.0642	2
006	$23^0 34`$	1.9283	1.9280	4	$23^0 32`$	1.9323	1.9909	3	$23^0 29`$	1.9335	1.9346	3	$10^0 39`$	1.9360	1.9371	3	$23^0 26`$	1.9373	1.9382	2
115	$24^0 43`$	1.8443	1.8435	14	$24^0 39`$	1.8486	1.8481	12	$24^0 36`$	1.8508	1.8514	10	$10^0 39`$	1.8535	1.8549	8	$24^0 33`$	1.8551	1.8559	6
204	$25^0 58`$	1.7660	1.7609	2	$25^0 49`$	1.7694	1.7704	2	$25^0 48`$	1.7705	1.7712	2	$10^0 39`$	1.7729	1.7738	2	$25^0 44`$	1.7743	1.7751	2
213	$26^0 8`$	1.7533	1.7516	5	$26^0 2`$	1.7572	1.7563	3	$25^0 59`$	1.7592	1.7599	3	$10^0 39`$	1.7617	1.7624	3	$25^0 54`$	1.7635	1.7649	3
205	$28^0 37`$	1.6057	1.6094	3	$28^0 43`$	1.6088	1.6043	2	$28^0 36`$	1.6098	1.6104	2	$10^0 39`$	1.6120	1.6194	2	$28^0 25`$	1.6132	1.6134	2
008	$32^0 12`$	1.4462	1.4462	39	$32^0 7`$	1.4492	1.4499	36	$32^0 4`$	1.4501	1.4518	34	$10^0 39`$	1.4520	1.4529	31	$32^0 3`$	1.4531	1.4542	27

Table 2

Results of differential thermal and X-ray phase analysis of the density and micro hardness of SnSe-ErSe system alloys

№	Molecular composition, %		Unit cell volume, V, Å^3	Density, 10^3kg/m^3		Phase micro hardness, MPa	Unit cell parameters, Å		
	SnSe	*ErSe*		ρ_{peak}	$\rho_{X\text{-}ray}$		*a*	*b*	*c*
1	100	0	216.21	6.18	6.28	480	4.460	4.190	11.570
2	99	1	217.88	6.20	6.38	520	4.468	4.206	11.594
3	98	2	218.93	6.20	6.40	540	4.471	4.221	11.601
4	97	3	219.93	6.21	6.42	570	4.477	4.229	11.616
5	96	4	220.64	6.23	6.42	620	4.481	4.236	11.624

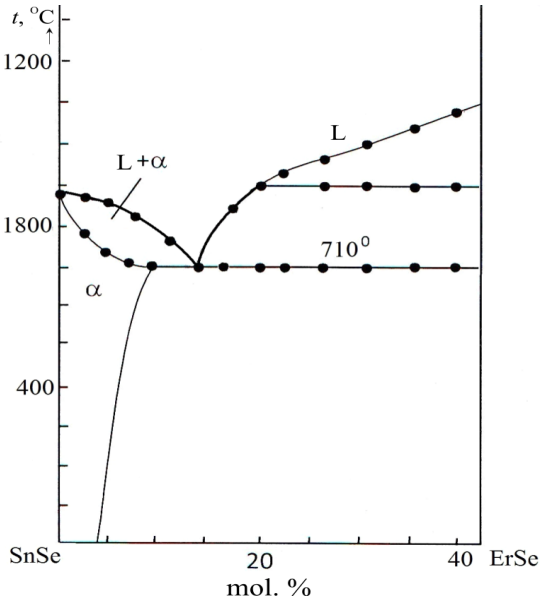

Fig. 1. Diagram of state of SnSe-ErSe system.

We have investigated the surface relief of *SnSe* single crystal using scanning probe microscope method in atomic-force mode (AFM) [8].

As a result, we obtained plane surface images of *SnSe* single crystal of size $5\cdot10^3 \times 5\cdot10^3$ nm (Fig. 2, *b*). The AFM image resulted from increasing the most homogeneous surface part. From Fig. 2, *a* showing 3-D images of the same parts it is seen that surface relief of a single crystal is uniform enough. The analysis of AFM image histogram (Fig. 2, *c*) shows that surface uniformity varies within 25 nm. It is obvious that though *SnSe* belongs to layered semiconductors with a natural surface cleavage, in the near-boundary layer there is still some roughness which is most likely due to the fact that at destruction of bonding forces not individual atoms, but their groups – clusters, remain on crystal surface.

This is also proved by the Fourier spectrum obtained by the AFM method (Fig. 2, *d*). Concentration of spectrum in the image centre shows that surface particles have about identical dimensions, i.e. they are commensurable.

The paper investigated the temperature dependences of the electric conductivity, the Hall coefficient, the thermoelectric figure of merit in the temperature range of 77 – 900 K, and the thermal conductivity in the temperature range of 77 – 350 °K of $Sn_{1-x}Er_xSe$ alloys. The results of investigation are given in Fig. 3. As it follows from Fig. 3 *a*, a change in the electric conductivity of the source compound *SnSe* and $Sn_{1-x}Er_xSe$ solid solutions on its basis with temperature are similar, i.e. at low temperatures there is a relatively weak electric conductivity increase at the cost of electrons

that passed from impurity levels to conduction band. At room temperature the number of carriers that passed from impurity levels to conduction band is stabilized and, hence, the electric conductivity is reduced due to a reduction of the Hall mobility, and with the onset of intrinsic conductivity it is increased due to increase in the concentration of intrinsic carriers.

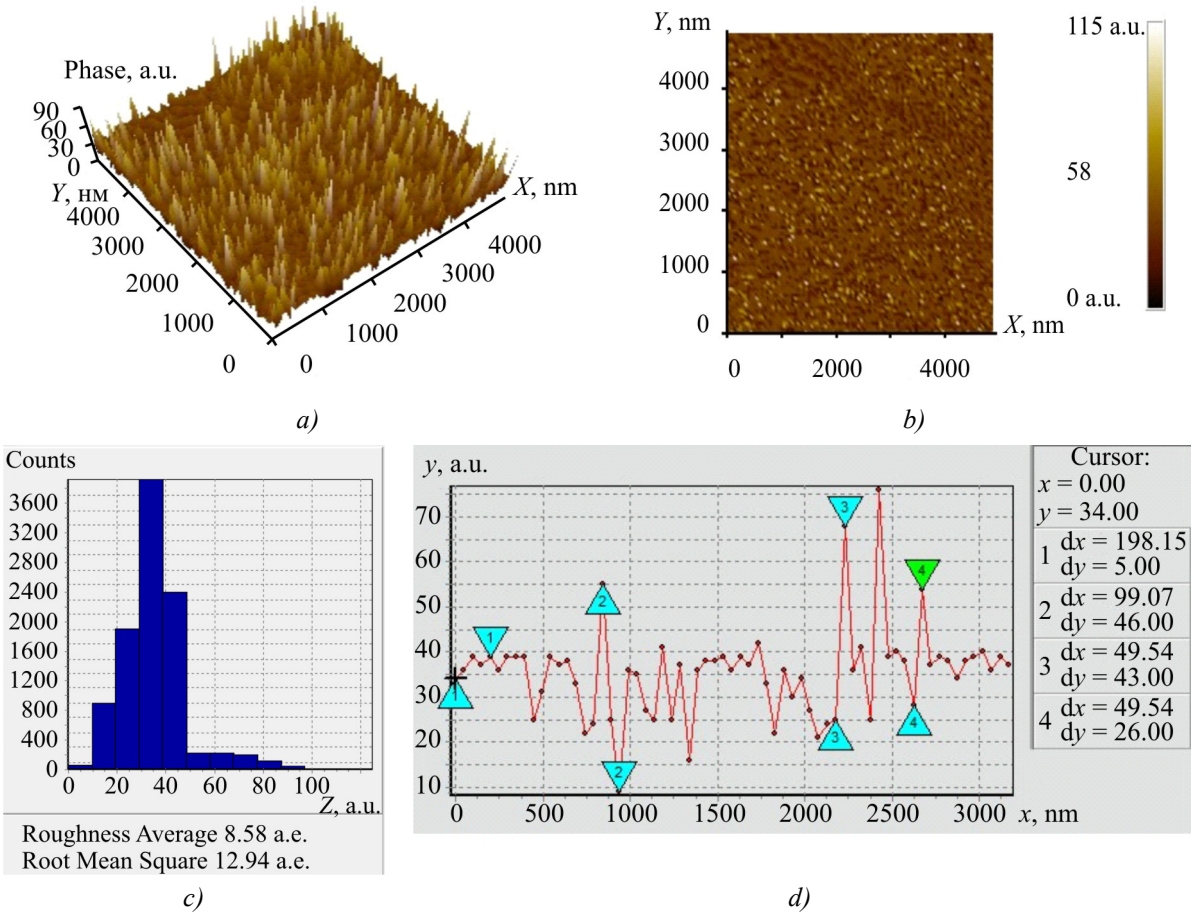

Fig. 2. (a) – 3D, (b) – two-dimensional AFM image of surface, (c) – surface histogram, (d) –Fourier spectrum of SnSe single crystal of size 5 μm.

A change in the Hall coefficient with temperature agrees well with the temperature change of the electric conductivity of $Sn_{1-x}Er_xSe$ crystals (Fig. 3, *b*), i.e. at low temperatures *R* remains constant, and with the onset of intrinsic conductivity it is reduced with a rise in temperature. The Seebeck coefficient of crystals at low temperatures in the field of impurity conductivity is increased, and with the onset of intrinsic conductivity it is reduced (Fig. 3, *c*), which is typical of semiconductor compounds and solid solutions with a complex band structure. The energy gap width of $Sn_{1-x}Er_xSe$ crystals was determined to an accuracy of 0.004 eV. The values of energy gap width calculated from the temperature dependences of the electric conductivity and the Hall coefficient correlate well. This testifies to the fact that all investigated samples are characterized by one predominant impurity level.

It is established that with a substitution of erbium atoms for tin atoms in *SnSe* lattice the energy gap width is reduced, i.e. for *SnSe* it was 0.86 eV, and for $Sn_{0.075}Er_{0.025}Se$ and $Sn_{0.095}Er_{0.05}Se$ compositions - 0.83 and 0.81 eV, respectively.

The thermal conductivity of solid $Sn_{1-x}Er_xSe$ was measured by a steady-state method. Investigations were pursued in the temperature range of 80 – 330 K. The results of research are given

in Fig. 3, *d*. As it follows from Fig. 3, *d*, the thermal conductivity of *SnSe* with a variation of cation composition along the direction of increasing atomic weights of substitution cations is regularly decreased. However, when passing from *SnSe* with the ordered arrangement of atoms to substitution solid solutions on its basis, there are deviations from a regular change in the thermal conductivity as a function of atomic weight. Apparently, this is due to the fact that for $Sn_{1-x}Er_xSe$ crystals prevalent is phonon scattering from local point defects, and the main factor that affects thermal resistance is local density variation and change in elastic properties of the medium. Local density variation mainly depends on the difference in average atomic weights, and local changes in elastic properties – on the difference in atomic radii of the solvent and dissolved material.

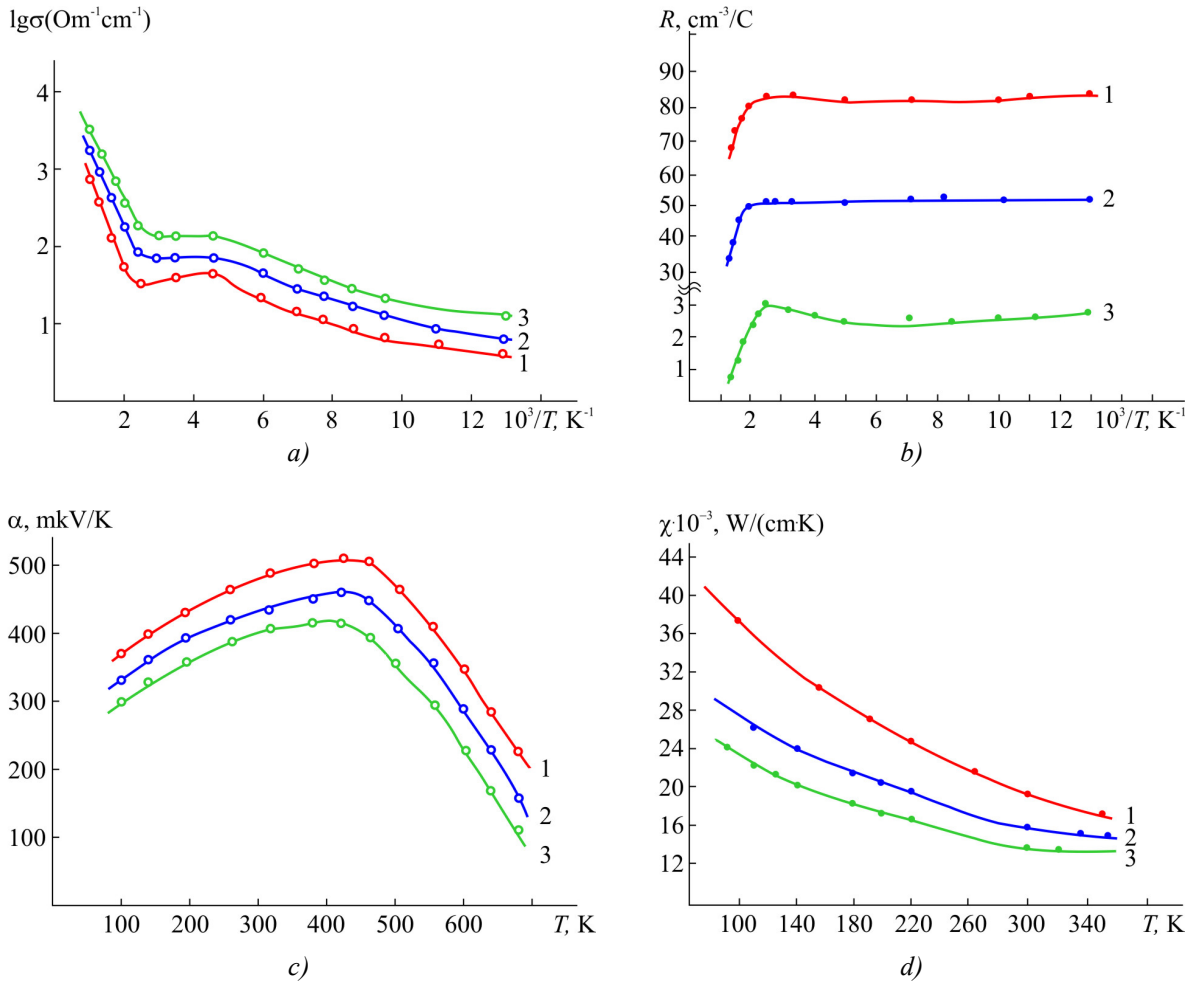

Fig. 3. Temperature dependences of the electric conductivity (a), the Hall coefficient (b), the Seebeck coefficient (c) and the thermal conductivity of $Sn_{1-x}Er_xSe$ crystals where 1 – x = 0; 2 – x = 0.02; 3 – x = 0.04.

Our experimental results suggest that with increasing erbium content in $Sn_{1-x}Er_xSe$ solid solutions, their electric conductivity is increased and thermal conductivity is decreased. Therefore, one would expect that in this system in certain compositions and in certain temperature range the thermoelectric figure of merit will reach the value which is of practical significance. The results of calculation are given in Table 3. As it follows from the table, for $Sn_{0.96}Er_{0.04}Se$ composition in the temperature range of 250 – 300 K the thermoelectric figure of merit proves to be high $(1.36 – 1.81)\cdot10^{-3}$ K^{-1} and is of practical interest.

Table 3

Thermoelectric parameters of $Sn_{1-x}Er_xSe$ alloys

T, K	*SnSe*				$Sn_{0.98}Er_{0.02}Se$				$Sn_{0.96}Er_{0.04}Se$			
	σ_1, $Ohm^{-1}\cdot cm^{-1}$	α_1, μV/K	χ_1, W /(cm·K)	$Z_1\cdot10^3$, K^{-1}	σ_2, $Ohm^{-1}\cdot cm^{-1}$	α_2, μV/K	χ_2, W/(cm·K)	$Z_2\cdot10^3$, K^{-1}	σ_3, $Ohm^{-1}\cdot cm^{-1}$	α_3, μV/K	χ_3, W/(cm·K)	$Z_3\cdot10^3$, K^{-1}
100	56.23	370	37	0.21	11.2	330	27.5	0.44	17.8	300	23.2	0.69
125	10	390	34.6	0.44	22.4	350	25.4	0.11	35.5	320	21.2	0.17
167	20	403	29.4	0.11	44.7	375	22.4	0.28	79.4	335	19	0.47
250	44.67	460	22.2	0.43	79	420	17.6	0.79	141.3	380	15	1.36
300	31.6	480	19.6	0.37	63.1	435	15.8	0.76	158.5	400	14	1.81

Conclusion

Physicochemical analysis methods have been used to construct the diagram of state of *SnSe*-40 mol.% *ErSe* section, and it has been established that in this system *SnSe* based solid solutions are formed in the region of ($0 \le x \le 0.04$). Surface microrelief and the temperature dependences of the electric conductivity, the Hall coefficient, the Seebeck coefficient, and the thermal conductivity have been investigated and the thermoelectric figure of merit of $Sn_{1-x}Er_xSe$ alloys has been calculated.

References

1. N.Kh.Abrikosov, V.F.Bankina, A.V.Poretskaya, and E.D.Skudnogo, *Semiconductor Compounds, their Preparation and Properties* (Moscow: Nauka, 1967), 220 p.
2. *P.S.Yerofeev, O.V.Salamatnikova, V.S.Gaidukova, and S.I.Repenko,* On the Issue of Interaction between Monochalcogenides of Bivalent IV Group Elements and Rare-Earth Metals, *Chalcogenides, Issue 3* (Kyiv: Naukova Dumka, 1974), p.87.
3. *N.Kh.Abrikosov, L.E.Shelimova, Semiconductor Materials Based on $A^{IV}B^{VI}$ Compounds* (Moscow: Nauka, 1975), 195 p.
4. *N.Bouad, M.-C.Record, J.-C.Tedenac, and R.-M.Marin-Ayral,* Mechanical Alloying of a Thermoelectric Alloy: $Pb_{0.65}Sn_{0.35}Te$, *J. Solid State Chem*. **177** (1), 221-226 (2004).
5. *A.E.Klimov, V.N.Shumskiy, Photosensitivity of $Pb_{1-x}Sn_xTe$ <İn> Films in the Intrinsic Absorption Range, Semiconductors* **42**(2), 147-152 (2008)
6. *A.P.Gurshumov, B.B.Kuliev, A.M.Akhmedov,* Diagrams of State of Metal Systems, Ed. by L.A.Petrova (Moscow, 1986, issue 29), p.429-430.
7. A.P.Gurshumov, B.B.Kuliev, A.M.Akhmedov, D.M.Safarov, and V.B.Lazarev, Interaction between Tin Monoselenide and Monoselenides of Rare-Earth Materials, *Izvestiya AN SSSR, Inorganic Materials* **20** (7), 1090-1093 (1984).
8. *V.Mironov, Fundamentals of Scanning Probe Microscopy* (Moscow: Technosphera, 2004), p. 197-201.

Submitted.25.02.14

E.I. Rogacheva[1], O.S. Vodorez[1], O.N. Nashchekina[1], M.S. Dresselhaus[2]

[1]National Technical University "Kharkov Polytechnic Institute", 21 Frunze St., Kharkov 61002, Ukraine
[2]Massachusetts Institute of Technology, 77 Massachusetts Ave., Cambridge, MA 02139, USA

PECULIARITIES OF CONCENTRATION DEPENDENCES OF THERMAL CONDUCTIVITY IN $(PbTe)_{1-x}$ $(Bi_2Te_3)_x$ SEMICONDUCTOR SOLID SOLUTIONS

For the semiconductor $(PbTe)_{1-x}$ $(Bi_2Te_3)_x$ solid solutions, the temperature (T = 250 – 670 K) and concentration (x = 0 – 0.07) dependences of the total λ and lattice λ_p thermal conductivities were obtained. It was established that the dependences $\lambda(x)$, $\lambda_p(x)$ and $\beta(x)$ (where β is the exponent in the $\lambda_p \sim T^{-\beta}$ dependence) have a non-monotonic dependence on x in this range of x. While showing a general tendency to decrease with increasing x, the three variables λ, λ_p, and β exhibit maxima at x = 0.005, 0.015 and x = 0.03. The oscillatory character of these dependences is attributable to the changes in thermal transfer processes and the mechanisms of phonon scattering under transitions from the dilute to the concentrated and associated solid solutions, with the transitions due to spatial ordering processes. The effective cross-section σ_s for phonon scattering by impurity atoms was estimated on the basis of the experimental data and theoretical calculations in accordance with the Klemens theory. The mean σ_s value in the homogeneity region of PbTe (x = 0 – 0.05) found experimentally coincides with the theoretically calculated σ_s value. However, in the region of the dilute solid solutions (x < 0.005), the σ_s value considerably exceeds the mean σ_s value. Also long-term aging reduces λ by ~ 15%.

Key words: $(PbTe)_{1-x}(Bi_2Te_3)_x$ solid solutions, thermal conductivity, isotherms, concentration anomalies, percolation, self-organization, critical phenomena.

Introduction

A conventional method for enhancing the dimensionless thermoelectric (TE) figure of merit ZT ($ZT = S^2\sigma T/\lambda$, where S is the Seebeck coefficient, σ is the electrical conductivity, λ is the thermal conductivity, and T is the absolute temperature) of semiconductor compounds is the formation of the solid solutions. The purpose of using solid solutions is for decreasing the lattice thermal conductivity λ_p, and for their subsequent doping to obtain the optimal carrier concentration [1, 2]. It is usually assumed that in the range of solid solutions, the physical properties of materials change monotonically and that under doping, the lattice properties and λ_p practically do not change. However, in a number of solid solutions based on the semiconductor IV-VI compounds, in the region of small impurity content (less than ~1 at.%), we revealed concentration dependent anomalies of the mechanical, galvanomagnetic, and TE properties (see, for example, [3-7]) and attributed their existence to critical phenomena accompanying the transition to an impurity continuum [7,8]. Besides, in some concentrated solid solutions [9], we observed an oscillatory character of the property–composition dependences, which we attributed to ordering processes that occurred when the interaction between impurity atoms starts to make a significant contribution to the free energy of the crystal. These concentration anomalies must be taken into account when

developing more efficient TE materials and these anomalies call for further detailed studies in this direction, as are presented here.

IV-VI compounds and solid solutions based on these compounds are among the best medium-temperature TE materials, which at present are used extensively for energy generation [1, 2]. The PbTe-based solid solutions in the Pb – Bi – Te system have attracted special attention for a long time because, firstly, Bi is counted among the major donor impurities in PbTe for controlling the electron concentration and for obtaining the maximal ZT value, and, secondly, there is available information about a substantial λ reduction under the introduction of Bi in PbTe [1, 2, 10].

Bi can be introduced in PbTe in a variety of ways: one can for example introduce elementary Bi [11, 12], or BiTe [13, 14] and Bi_2Te_3 compounds [14-22], etc. In all cases, under the introduction of Bi into stoichiometric *p*-PbTe, an inversion of the sign of the conductivity takes place at a Bi concentration of less than 0.1 at.%. In most works the PbTe-based solid solutions along the quasi-binary $(PbTe)_{1-x}$ $(Bi_2Te_3)_x$ section of the Pb – Bi – Te ternary system [14-22] are studied (brief overviews of those works are given in [21,22]).

Recently, we have reported [21,22] the results of our detailed studies on the room temperature dependences of the *X*-ray diffraction line width, the microhardness H, σ, S, Hall coefficient R_H, and charge carrier mobility μ in the $(PbTe)_{1-x}$ $(Bi_2Te_3)_x$ solid solutions on composition in the concentration range $x = 0 – 0.06$, corresponding to the interval of PbTe-based solid solutions. According to [21,22], the concentration dependences of the properties exhibit a non-monotonic behavior that is unusual for solid solutions, indicating that qualitative changes in the defect subsystem take place under increasing the Bi_2Te_3 concentration. The observed peculiarities were attributed to the transition from the dilute to the concentrated solid solutions, and then to associated solid solutions, as well as to the pertinent ordering processes [21, 22].

The influence of small concentrations of Bi_2Te_3 on the PbTe thermal conductivity was studied in [16-18]. The authors of [16,17], who investigated the concentration range of $x = 0.002 – 0.0085$ in the $(PbTe)_{1-x}Bi_2Te_3)_x$ system, showed that at room temperature, with increasing x, the electronic component λ_e of the total thermal conductivity monotonically increases, λ_p decreases, and λ practically does not change. Almost similar results in terms of both the behavior of the concentration dependences of λ, λ_e and λ_p and the values of the thermal conductivity were obtained in [18], where a still narrower concentration range in the vicinity of PbTe (x = 0 – 0.13) was studied. Like in [17], no concentration anomalies were observed, and all alloys, including the initial compound PbTe, exhibited n-type conductivity.

The goal of the present work is to study the thermal conductivity of $(PbTe)_{1-x}$ $(Bi_2Te_3)_x$ solid solutions in the concentration range of $x = 0 – 0.07$ with the purpose of establishing whether or not the λ isotherms exhibit a non-monotonic behavior like the isotherms for the properties described above.

One of the important factors, which determine the operating efficiency of TE devices, is the device lifetime. That is why studying the influence of the material aging on its thermal conductivity is also of interest, and is reported in the present work.

Experimental details

$(PbTe)_{1-x}$ $(Bi_2Te_3)_x$ cylindrical samples with a height of 5 mm and a diameter of 15 mm for the thermal conductivity measurements were prepared by hot pressing at the temperature $T_p = 650$ K and loading $P = 0.4$ GPa from polycrystalline alloys, synthesized using a method described in [21,22].

After pressing, all samples were annealed at 720 K for 200 hours. The chemical composition and homogeneity of the samples were controlled by electron-probe microanalysis and by energy dispersive X-ray spectroscopy using a scanning electron microscope. It was shown that the chemical compositions of the samples corresponded to what was intended with an accuracy of not less than 5 % and the degree of the sample homogeneity was satisfactory. Besides, we investigated the pressed samples, prepared earlier by a similar method and these samples had been subjected to aging at room temperature for 25 years.

The thermal conductivity was measured by the dynamic calorimeter method [23] in the mode of monotonic heating in the temperature range 170 – 670 K. There were at least three measurements of λ for each sample. The shift of the $\lambda(T)$ curves for different measurements on the same samples (which resulted from a possible non-identical setting of a sample in the measuring cell) did not exceed ~ 3 %. The accuracy of the λ measurement was ± 5 %. The electrical conductivity σ was measured using the van der Pauw method with the accuracy not worse than ~ 5%. The lattice component λ_p of the total thermal conductivity λ was isolated by the subtraction of the electronic component λ_e determined using the Wiedemann - Franz law $\lambda_e = L\sigma T$, where L is the Lorentz number ($L = (\pi^2/3)(k/e)^2 \approx 2.47 \cdot 10^{-8}$ WΩK^{-2}).

Results and discussion

In Fig. 1, a, the temperature dependences of the total thermal conductivity of as-prepared $(PbTe)_{1-x}$ $(Bi_2Te_3)_x$ samples with different compositions are presented. All curves have a similar character: as the temperature increases up to ~ 450 - 500 K, λ decreases, but under further increase in temperature, λ starts to increase.

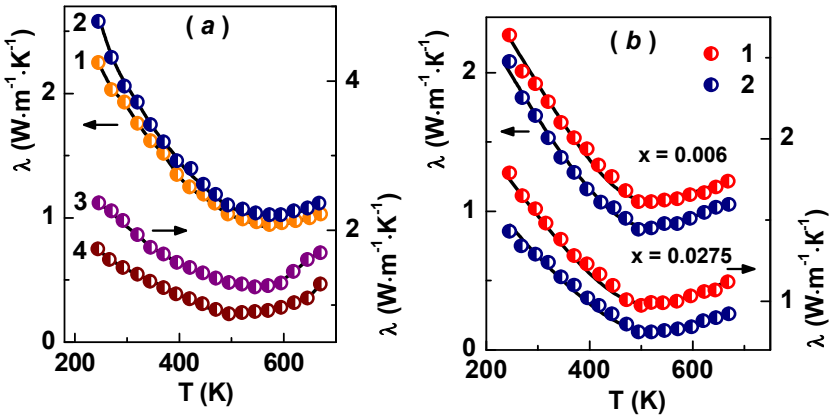

Fig.1. The temperature dependences of the total thermal conductivity λ for $(PbTe)_{1-x}$ $(Bi_2Te_3)_x$ solid solutions. a – as-prepared samples, 1 – PbTe (x = 0); 2 – x = 0.0035; 3 – x = 0.01; 4 – x = 0.025; b – as-prepared samples (1), and samples after aging (2).

It is known that heat in semiconductors can be transferred by crystal lattice vibrations, the electron gas, electromagnetic radiation, as well as by the bipolar diffusion of charge carriers; thus the equation for calculating the total thermal conductivity λ must include the lattice λ_p, electronic λ_e, photon λ_{ph}, and bipolar λ_b components [24-26]:

$$\lambda = \lambda_p + \lambda_e + \lambda_{ph} + \lambda_b \qquad (1)$$

Taking into account that the PbTe optical absorption coefficient α is rather high ($\alpha \sim 200$ cm^{-1} [26]), the heat transfer by electromagnetic radiation can be neglected. Indeed, the estimation of λ_{ph} using the formula: $\lambda_{ph} = 16\, n^2\, \sigma_0\, T^3/3\, \alpha$, where n is the refractive index, σ_0 is the Stefan–Boltzmann constant, α is the absorption coefficient, and T is the absolute temperature, shows that over the entire temperature range, the contribution of λ_{ph} from photons to λ does not exceed ~0.5 %. The increase in λ observed at temperatures above ~ 450 K can be explained, like in PbTe, by the appearance of a bipolar diffusion of charge carriers caused by the occurrence of the intrinsic conductivity [26]. Below ~ 450 K, the bipolar component practically does not make any contribution, and one can assume that λ is determined mainly by λ_p and λ_e.

In Fig. 1 (*b*), for comparison, the $\lambda(T)$ dependences for as-prepared samples and for the samples aged for 25 years at room temperature (x = 0.006 and x = 0.0275) are presented. It is seen that both curves have a similar character (running virtually in parallel), but after aging, the λ values decrease on average by ~ 15 %.

On the basis of the $\lambda(T)$ dependences for as-prepared samples, the λ isotherms in the temperature range 250 – 470 K were plotted (Fig. 2). It is seen that while exhibiting a general tendency to decrease in λ with increasing x, these dependences have a complex oscillatory character. At $x > 0.05$, λ does not depend on concentration x, which is explained by reaching the boundary of the solubility region for Bi_2Te_3 in PbTe and entering the two-phase region [21, 22].

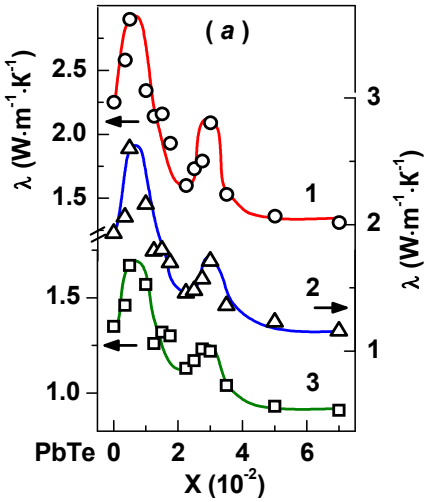

Fig.2. The isotherms of the total thermal conductivity λ for $(PbTe)_{1-x}$ $(Bi_2Te_3)_x$ solid solutions at various temperatures 1 – 250 K; 2 – 300 K; 3 – 450 K.

In Fig. 3 (a), the dependence of the room-temperature lattice thermal conductivity λ_p on composition is presented. Similar to the total thermal conductivity, λ_p shows a general trend to decrease under increasing Bi_2Te_3 concentration (in Fig. 3a the monotonic component of the $\lambda_p(x)$ dependence is shown with a dashed line), but at the same time, three distinct maxima near x = 0.005, 0.015 and 0.03 are observed in the $\lambda_p(x)$ curve.

Thus, the experimental results obtained in the present work demonstrate that the $\lambda_p(x)$ dependence exhibits a complex behavior, which can be treated as an overlapping of the monotonic and oscillatory λ_p components. The presence of three maxima in this dependence shows that at certain concentrations of the solid solution, phonon scattering decreases and the velocity of the propagation of elementary excitations increases.

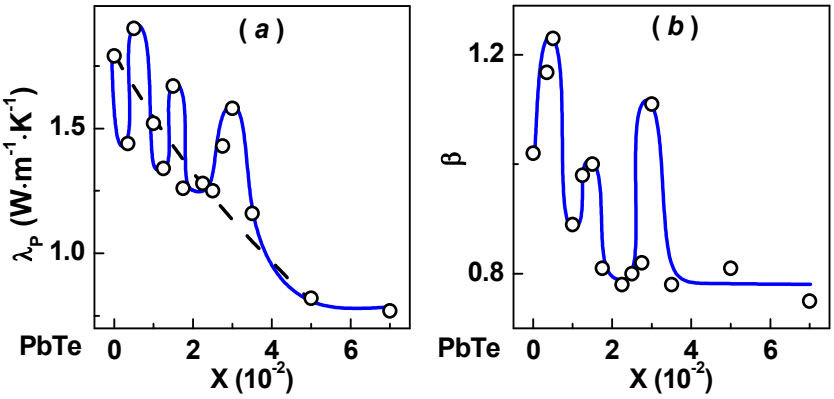

Fig.3. The dependences of the lattice thermal conductivity λ_p (a), and the exponent β in the temperature dependence of λ_p (b), on $(PbTe)_{1-x}$ $(Bi_2Te_3)_x$ solid solutions composition x.

It is known [24-26] that at temperatures above the Debye temperature Θ (for PbTe Θ = 130 K [27]), the phonon mean free path is limited mainly by three-phonon interactions and by the interaction of phonons with crystal lattice defects. In this case, in accordance with the Debye-Peierls theory of the thermal conductivity, at temperatures near and above Θ, the lattice thermal conductivity decreases inversely with temperature: $\lambda_p \sim 1/T$.

It was of interest to find out whether such a dependence of $\lambda_p(T)$ is also observed in the $(PbTe)_{1-x}$ $(Bi_2Te_3)_x$ solid solutions. Assuming a power law for the temperature dependence of the λ_p ($\lambda_p \sim T^{-\beta}$), we estimated the exponent β values for the alloys of different compositions in the temperature range 250 – 450 K, when the contribution of the bipolar diffusion is insignificant and can be neglected. In Fig. 3(b), the β (x) dependence is shown. It is seen that $\beta = 1 \pm 0.02$ only for PbTe (which is in good agreement with the Debye - Peierls theory and experimental results obtained by other authors for PbTe [26, 27]). However the introduction of Bi_2Te_3 in PbTe leads to a complex oscillatory dependence $\beta(x)$ with maxima near x = 0.005, 0.015 and 0.03. The most pronounced maxima correspond to x = 0.005 and x = 0.03. The change in the exponent β in the $(PbTe)_{1-x}$ $(Bi_2Te_3)_x$ solid solutions under changing x and the extreme character of the $\beta(x)$ dependences indicate a change in the heat transfer and phonon scattering processes at certain compositions x.

According to generally accepted concepts of the classical physicochemical analysis, the "property vs. composition" dependences of solid solutions should represent monotonic curves. It is assumed in the quasi-chemical approximation that the interaction energy between atoms does not depend on the solid solution concentration. Within the framework of these views, it is logical to suppose that with increasing impurity concentration in the range of the solid solution regime, λ_p will decrease due to an increase in phonon scattering by impurity atoms [24-26]. That is why the observed complex behavior of the λ, λ_p, and β isotherms requires explanations.

According to our views [7, 8], in any solid solution, independent of the nature of particles interactions, reaching the percolation threshold x_c corresponds to the formation of an impurity continuum and must be accompanied by critical phenomena, – anomalies in the concentration dependences of the physical properties. It is the concentration corresponding to the percolation threshold x_c that can be considered to be a boundary separating dilute and concentrated solid solutions.

In accordance with these views, the anomalous growth in λ_p in the concentration range x = 0.0035 - 0.005 can be attributed to critical phenomena accompanying a transition of a percolation type

taking place in the impurity subsystem of the crystal when the impurity concentration reaches the percolation threshold [28,29]. At small impurity concentrations, when the distance between impurity atoms is large and the deformational fields of nearest neighbor impurity atoms do not overlap, impurity atoms make an additive contribution to the lattice thermal resistivity ($1/\lambda_p$), either increasing $1/\lambda_p$ or decreasing λ_p. As the impurity concentration increases, the overlapping of the elastic fields of neighboring atoms starts to become important and produces a partial compensation of the impurity-imposed elastic stresses, thereby causing the oscillatory behavior observed at very low values of x. On reaching the percolation threshold, an «infinite cluster» (chain of interacting impurity atoms) is formed, thereby penetrating the entire crystal. Under further increase in x, the density of the «infinite cluster» increases over a sufficiently narrow concentration interval, and after that one can assume the formation of an impurity continuum. A percolation transition is similar to a type II (second order) phase transition, which is accompanied by critical phenomena [28, 29]. The increase in λ_p is associated with the compensation of stresses which take on a collective character, thereby facilitating the propagation of phonons, and reducing phonon scattering. After the process of elastic stress compensation spreads over the entire crystal volume, this entire crystal volume becomes filled with "impurity liquid". Further introduction of impurity atoms leads to new lattice distortions, and, consequently, to a decrease in the λ_p value. Taking into account the abrupt increase in λ_p near $x = 0.0035$, the possibility of impurity atom ordering on reaching the percolation threshold should not be excluded.

After the transition from the dilute to concentrated solid solution occurs (near $x = 0.0035$), when all the impurity atoms become connected, self-organization processes become possible. The observed increase in λ_p in the concentration ranges $x = 0.0125 – 0.015$ and $x = 0.025 – 0.03$ suggests that such self-organization processes take place, and with the highest probability they are caused by a possible short-range ordering, i.e. by the formation of groups of atoms (clusters) in a macroscopically homogeneous solution as a result of the interactions of atoms not only with their nearest neighbors but also with those in the next neighbor coordination range. Apart from the short-range order of a general type, which is present in any solid solution and is associated with the difference in the interaction energies of different atoms, there can exist a short-range ordering connected with the manifestation of a chemical interaction in the solid solution. The introduction of a dopant in the form of a stable chemical compound (in our case the Bi_2Te_3 compound) with the crystal structure differing from the matrix structure (in our case PbTe) stimulates the formation of regions with short-range ordering (complexes) and chemical bonds corresponding to the composition of that compound. In [30] on the basis of the analysis of experimental data on the concentration dependences of the various physical properties and the results of theoretical calculations using appropriate phenomenological methods for modeling cluster components, it was shown that in solid solutions formed by stable compounds, the chemical interaction between impurity and matrix atoms leads to the formation of neutral chemical complexes and microheterogeneous structures within the solid solution. Physico-chemical properties of a solution also depend on the type of neutral associates that are formed in the solid solution.

The oscillatory character of the λ, λ_p and β dependences that is observed in this work may indicate a change in the type of clusters formed under changing solid solution composition, i.e. a change in atomic configurations corresponding to minima of the potential energy.

If the concentration of complexes is so high that percolation channels linking complexes and penetrating the entire crystal are formed and if the crystal structure of complexes differs from the matrix structure, then in the percolation theory approximation one can suggest the existence of another percolation threshold x_k.

The anomalous increase in λ_p in the vicinity of $x = 0.03$, as well as earlier observed peculiarities in the isotherms of other properties near the indicated composition [21,22] (an increase in the electrical conductivity and charge carrier mobility, the constancy of the X-ray line width B for as-made samples and a sharp decrease in B after long-term aging, etc.), all allow us to suggest that the observed effects are connected with the formation of percolation channels linking not separate impurity atoms, but rather associates of the impurity atoms (i.e. molecules or clusters of molecules) are in this case reaching the percolation threshold x_k. With the highest probability, the composition of such associates corresponds to the composition of the precipitated phase that reaches the solubility limit (Bi_2Te_3 or the ternary $PbBi_2Te_4$ compound). The decrease in B at $x = 0.03$ almost down to the B value for the initial PbTe after long-term aging, indicates a high degree of local ordering and suggests that after the formation of the infinite cluster, short-range ordering (the formation of molecular complexes) is accompanied by long-range ordering of the molecular complexes within the solid solution [21,22].

From the concentration dependence of λ_p in the range $x = 0 – 0.0035$, i.e. in the region of PbTe-based dilute solid solutions, the effective phonon cross-section σ_s of scattering by Bi impurity atoms was estimated using the Ioffe formula [31]:

$$\frac{\lambda_{p_o}}{\lambda_p} = 1 + \Phi \cdot \frac{N}{N_o} \cdot \frac{l_o}{d} \tag{2}$$

where λ_{p0} and λ_p are, respectively, the lattice thermal conductivity of the crystal without impurities and with impurities, N_0 and N are, respectively, the total number of all atoms and the number of impurity atoms per unit volume, d is the distance between impurity atoms, l_0 is the phonon mean free path, which enters into the equation for the lattice thermal conductivity λ_{p0} of the undoped crystal:

$$\lambda_{p_o} = (1/3) \cdot l_o \cdot C_v \cdot V_g \tag{3}$$

where C_v is the heat capacity per unit volume, and V_g is the mean phonon group velocity, and Φ is a dimensionless coefficient which enters into the equation $\sigma_s = \Phi\, d^{\,2}$. From equation (2) one can easily determine Φ and σ_s.

However, there arises a problem, insofar as it is the phonon group velocity V_g that appears in equation (3), and not the sound phase velocity V_p. The latter can be experimentally measured relatively easily, but the difference between the two velocities V_g and V_p can be rather significant. For example, the calculation [33] performed for PbTe shows that $V_g = V_p/3$. Theoretical calculations of phonon group velocity V_g with frequency – and branch-dependent analysis have been performed in some other works too, for example in [34, 35], where the authors used first-principles-based anharmonic lattice dynamics simulations. The group velocity was averaged for transverse and longitudinal acoustic branches to be a function of frequency. There obtained very low values of the group velocity for the long-wave transverse acoustic phonons along the [100] direction. That is why, if when calculating Φ one uses the mean sound phase velocity, an error will be introduced, and to correct the result one should multiply the value of Φ thus obtained by $\alpha = V_g/V_p$ [36].

Since at present an accurate experimental value of the group velocity for PbTe is unknown, when calculating Φ we used a value of the mean sound phase velocity instead of V_g, which, in turn, was calculated as $V_p = (V_l + 2\ V_t)/3 = (3000+2\ 2430)/3 = 2620$ m/s, where V_l and V_t are the longitudinal and transverse components of the sound velocity of PbTe, respectively [26].

It should be also noted that numerical values of σ_s and Φ that are obtained in this way depend significantly on the particular range of Bi concentrations for which these values have been determined,

because in general the λ_p - composition dependences are not linear. It follows from the above discussion that any comparison of the calculated values of Φ with the literature data is possible only when the same concentration ranges are considered and the same values of the phonon group velocities are used for the pertinent calculations.

Substituting values of λ_{p0}, λ_p, N, N_0, as well as C_v [25]·and V_g into equation (2), we obtain that for the concentration range x = 0 – 0.05, Φ = 4.9 and σ_s= 4.9 d^2 at 300 K (Table 1). These values correspond to a drop in λ_p over the entire homogeneity range (x = 0 – 0.05). If we consider the interval x = 0 – 0.0035, i.e. the region of the initial drop in λ_p, we will obtain a considerably higher value Φ = 13 and σ_s = 13 d^2, which indicates a drastic increase in phonon scattering when the early introduction of the first portions of impurity atoms occurs. Such an increase can be explained by the fact that the introduction of the first portions of the impurity atoms leads to a sharp growth in the configuration entropy, denoting the probability of the impurity atoms being delocalized increases relative to their basic structural positions, specifically, allowing the impurity atoms to enter the interstices of the crystal lattice. The first portions of the impurity are introduced into the PbTe host material not as a neutral Bi_2Te_3 compound, but rather as separate Bi and Te atoms, which, with a high probability, occupy interstices in the PbTe crystal lattice.

According to the Klemens theory [37, 38], point defect scattering may be considered to be the combined effect of scattering due to the mass difference ΔM/M, the change in the force constants at the defect site ΔG/G, and the strain field caused by the dilation or contraction of the lattice around a defect resulting from the difference in the effective size of the host atom (ion) and the substituting defect ΔR/R. According to Klemens [37, 38], the total scattering cross-section can be expressed as follows:

$$\sigma_s = \frac{V_o^2 \cdot \omega^4}{4\pi \cdot V_g^4}\left\{\left(\frac{\Delta M}{M}\right)^2 + 2\left(\frac{\Delta G}{G} - \frac{b}{\sqrt{5}}\cdot\gamma\cdot\frac{\Delta R}{R}\right)^2\right\} \quad (4)$$

where ω is the frequency (we assume that ω is the Debye frequency: $\omega = \omega_D = k\Theta_D/\hbar$), V_g is the phonon group velocity, M is the molar mass, G is the elastic modulus, γ is the Grüneisen constant, R is the ionic radius, and V_o is the volume per atom. Assuming Θ_D = 130 K [27], γ = 2 [35], b = 14.2 [35], $V_g = (V_l + 2\,V_t)/3$ = 2620 m/s [28], we obtain σ_S =5.9 d^2, i.e. Φ = 5.9 (Table 1).

Table 1

Phonon scattering cross-sections σ_s and the multiplying dimensionless factors Φ for $(PbTe)_{1-x}$ $(Bi_2Te_3)_x$ alloys

Concentration range, x	σ_s (10^{-20} m^2)		Φ	
	Experiment	Theory	Experiment	Theory
0 – 0.0035	135	61.4	13	5.9
0 – 0.05	51	61.4	4.9	5.9

It is seen from Table 1 that the maximum scattering of phonons occurs in the range of the smallest impurity concentrations, i.e. in the region of the most dilute solid solutions, when the crystal has the broadest variety of defects, which is stimulated by a sharp growth in configurational entropy under the introduction of the first range of impurity concentration in the crystal. It is also seen from Table 1 that the results of the theoretical calculations are in good agreement with the experimental data if we consider the concentration range (x = 0 – 0.05) corresponding to the entire homogeneity

region and ignore the regions of x where the anomalous behavior occurs (the dashed line in Fig. 3a). This fact can be explained rather easily if we take into consideration that the calculation according to the formula (4) assumes an ordinary cation or anion substitution [37, 38] and does not take into account the existence of defects other than substitutional defects, as, for example, interstitial species.

Conclusions

1. In the isotherms of the lattice thermal conductivity λ_p for $(PbTe)_{1-x}$ $(Bi_2Te_3)_x$ solid solutions (x = 0 – 0.07), with λ_p exhibiting a general tendency to decrease with increasing x (monotonic component in the $\lambda_p(x)$ dependence), three maxima are revealed near x = 0.005, 0.015 and 0.03. The existence of the first maximum at x = 0.005 is attributed to the critical phenomena accompanying a percolation type transition to an impurity continuum when the crystal lattice perturbation becomes delocalized. This transition is accompanied by both a partial compensation of stresses in the crystal lattice and an increase in the velocity of phonon propagation. The second maximum at x = 0.015 is attributed to the formation of an intermediate structure with short-range ordering, and the third maximum is identified with the formation of percolation channels through the neutral chemical complexes, which are formed in the solid solution at the stage preceding the precipitation of the second phase inclusions where the precipitation starts after reaching the solubility limit. In the latter case, the reaching of the percolation threshold is accompanied by ordering processes, whose presence is supported by our earlier observations [21], specifically a sharp decrease in the X-ray line width almost down to the X-ray line width value in PbTe observed near x = 0.03 after long-term aging. It is also shown in the present study that long-term aging of the $(PbTe)_{1-x}$ $(Bi_2Te_3)_x$ solid solutions leads to an insignificant decrease in λ.

The study of the temperature dependences of the thermal conductivity showed that there are three maxima in the dependence of the exponent $\beta(x)$ in the $\lambda(T)$ dependences, corresponding to the same values of the composition x of the solid solution. The changes of β with x also indicates that there are qualitative changes in the processes of the heat transfer taking place in the phonon scattering mechanisms when changing the solid solution compositions.

2. The phonon effective scattering cross-section σ_s for Bi impurity atoms was estimated on the basis of the experimental data using the Ioffe formula and on the basis of the theoretical calculations using the Klemens theory. It is found that the mean σ_s value over the large range of compositions for the PbTe homogeneity region (x = 0 – 0.05) determined experimentally using the monotonic component of the $\lambda_p(x)$ dependence ($\sigma_s = 4.9\ d^2$) yields good agreement with the results of the theoretical calculations. However, in the region of the very dilute solid solutions (x = 0 – 0.0035), the abrupt increase in the σ_s value ($\sigma_s = 13\ d^2$) is here connected with the increasing assortment of possible structural defects and the rapidly increasing configuration entropy.

3. The observation of the concentration anomalies provides additional support for the idea of the existence of a percolation type transition in any solid solution in the range of very small impurity concentrations and indicates the non-monotonic behavior of the isotherms of specific properties within the more concentrated solid solutions region. The results obtained here suggest that when interpreting and predicting the expected properties (e.g. thermal conductivity) of solid solutions and doped semiconductors, it is necessary to take into account the existence of concentration anomalies connected with the interaction of impurity atoms among themselves within the matrix as well as with the matrix atoms.

The authors thank Shuang Tang for useful and fruitful discussions, as well as Dr. L.D. Ivanova and Yu. Granatkina for their help in measuring the thermal conductivity. This work was supported by the Ukrainian State Fund for Fundamental Research (grant # UU 42/006 2011) and by the U.S. Civilian Research and Development Foundation (grant # UKP2-7074-KK-12), as well by the NSF Materials World Network NSF/DMR-1107339 for M.S. Dresselhaus.

References

1. L.I. Anatychuk, *Thermoelements and Thermoelectric Devices: Reference Book* (Kyiv: Naukova Dumka Publishers, 1979) (in Russian].
2. *CRC Handbook of Thermoelectrics*, ed. D.M. Rowe (CRC Press: Boca Raton, London, New York, Washington, 1995).
3. E.I. Rogacheva, Concentration-Dependent Microhardness in Semiconductor Solid Solutions, *Izv. AN SSSR. Neorgan. Mater.,* **25**, 643-646 (1989).
4. E.I. Rogacheva, I.M. Krivulkin, V.P. Popov, and T.A. Lobkovskaya, Concentration Dependences of Properties in $Pb_{1-x}Mn_xTe$ Solid Solutions, *Phys. status solidi* A **148**, K65-K67 (1995).
5. E.I. Rogacheva, I.M. Krivulkin, Isotherms of Thermal Conductivity in PbTe-MnTe Solid Solutions, *Physics of the Solid State* **43**, 1000-1003 (2001).
6. E.I. Rogacheva, I.M. Krivulkin: The Temperature and Concentration Dependences of the Charge Carrier Mobility in PbTe-MnTe Solid Solutions, *Semiconductors*, 36, p. 966 – 972 (2002).
7. E.I. Rogacheva, Percolation Effects and Thermoelectric Materials Science, *J. Thermoelectricity* **2**, 61-72 (2007).
8. E.I. Rogacheva, Critical Phenomena in Heavily-Doped Semiconducting Compounds, *Jpn. J. Appl. Phys*, **32 S**, 775-777 (1993).
9. E.I. Rogacheva, O.S. Vodorez, Peculiarities of the Concentration Dependences of Structural and Thermoelectric Properties in Solid Solutions PbTe-PbSe, *J. Thermoelectricity*. **2**, 61-73 **(**2013).
10. L.E. Shelimova, O.G. Karpinskii, P.P. Konstantinov, E.S. Avilov, M.A. Kretova, I. Yu. Nikhezina, and V.S. Zemskov, *Perspektivnye Materialy* **5**, 5-13 (2009).
11. E.I. Rogacheva, S.G. Lyubchenko, Thermoelectric and Mechanical Properties of Lead Telluride Doped with Bismuth, *J. Thermoelectricity* **3**, 24-31 (2005)
12. L.D. Borisova, Thermoelectric Properties of Impurity Doped PbTe, *Phys. Stat. Sol.* **53 A**, K19-K22 (1979).
13. T.V. Tavrina, E.I. Rogacheva, V.I. Pinegin, Structural, Thermoelectric and Galvanomagnetic Properties of PbTe-BiTe Semiconductor Solid sSlutions, *Mold. J. Phys. Sci.* **4**, 430-434 (2005).
14. B.A.Efimova, G.F.Zakharyugina, and L.A.Kolomoyets, Thermoelectric Properties of Solid Solutions PbTe-Bi_2Te_3 and PbSe-Bi_2Se_3 *Izv. Akad. Nauk, SSSR. Neorgan. Mater.* **4**, 32-36 (1968).
15. E.I. Rogacheva, S.A. Laptev, V.S. Ploskaya, and B.A. Efimova, PbTe-based Solid Solutions in the Pb-Bi-Te System, *Izv. Akad. Nauk, SSSR. Neorgan. Mater.* **20**, 1350-1353 (1984).
16. P.W. Zhu, Yo. Imai, Yu. Isoda, Yo. Shinohara, X-P. Jia, and G-T. Zou, High Thermoelectric Properties of PbTe Doped with Bi_2Te_3 and Sb_2Te_3, *Chin. Phys. Lett.* **22**, 2103-2105 (2005).
17. P.W. Zhu, Yo. Imai, Yu. Isoda, and Yo.Shinohara, Composition-Dependent Thermoelectric Properties of PbTe Doped with Bi_2Te_3, *J. Alloys and Compounds* **420**, 233-236 (2006).
18. T. Su, P.W. Zhu, H. Ma, G. Ren, L. Chen, W. Guo, Y. Iami, and X. Jia, Electrical Transport and High Thermoelectric Properties of PbTe Doped with Bi_2Te_3 Prepared by HPHT, *Solid State Communs* **138**, 580-584 (2006).

19. T. Ikeda, M. Toussaint, K. Bergum, S. Iwanaga, and G.J. Snyder, Solubility and Formation of Ternary Widmanstatten Precipitates in PbTe in the Pseudo-Binary PbTe-Bi_2Te_3 System, *J. Mater. Sci* **46**, 3846-3854 (2011).
20. J.-H. Yim, K. Jung, H.-J. Kim, H.-H. Park, C. Park, J.-S. Kim, Ju-Hyuk Yim, Effect of Composition on Thermoelectric Properties in PbTe-Bi_2Te_3 Composites, *J. Electr. Mater.* **40**, 1010-1014 (2010).
21. E.I. Rogacheva, O.S. Vodorez, V.I. Pinegin, and O.N. Nashchekina, Evidence for Self-Organization Processes in PbTe-Bi_2Te_3 Semiconductor Solid Solutions, *J. Materials Research* **26**, 1627-1633 (2011).
22. E.I. Rogacheva, O.S. Vodorez, and O.N. Nashchekina, Oscillations of Transport Properties in PbTe - Bi_2Te_3 Solid Solutions, *J. Phys. Chem. Solids* **74**, 35-39 (2013).
23. E.S. Platunov, *Thermophysical Measurements in Monotonic Regime* (Moscow: Energiya, 1972) (in Russian).
24. R. Berman, *Thermal Conduction in Solids* (Oxford: Clarendon Press, 1976).
25. V.M. Mogilevskii, A.F. Chudnovskii, *Thermal Conductivity of Semiconductors* (Moscow: Nauka, 1972), 536 p. (in Russian).
26. Yu.I. Ravich, B.A. Efimova, and I.A. Smirnov, *Semiconducting Lead Chalcogenides* (New York: Plenum Press, 1970).
27. N.H. Abrikosov and L.E. Shelimova, *Semiconducting Materials Based on A^4B^6 compounds* (Moscow: Nauka, 1975) (in Russian).
28. B.I. Shklovskii, A.L. Efros, *Electronic Properties of Doped Semiconductors* (New York: Springer-Verlag, 1984).
29. D. Stauffer, *Introduction to Percolation Theory* (London/Philadelphia: Taylor and Francis, 1985).
30. E.I. Rogacheva, The Specificity of Structure and Electrical Behavior of Multinary Solid Solutions Formed by Chemical Compounds, *Phys. Status Solidi C* **6**, 1307-1311 (2009).
31. A.F. Ioffe, Heat Transfer in Semiconductors*, Canadian J. Phys*. **34**, 1342-1355 (1956).
32. A.V. Ioffe, A.F. Ioffe, Thermal Conductivity of Semiconductor Solid Solutions, *Solid State Physics* **2**, 781-792 (1960).
33. A.L. Efros, *Solid State Physics* **3**, 2065 (1961)
34. T. Shiga, J. Shiomi, J. Ma, O. Delaire, T. Radzynski, A. Lusakowski, K. Esfarjani, and G. Chen, Microscopic Mechanism of Low Thermal Conductivity in Lead Telluride, *Phys. Rev. B* **85**, 155203 (2012).
35. T. Hori, G. Chen, and J. Shiomi, Thermal Conductivity of Bulk Nanostructured Lead Telluride, *Appl. Phys. Lett.* **104**, 021915(1-5) (2014).
36. A.F. Ioffe, *Semiconducting Thermoelements,* (Moscow-Leningrad: Akad. Nauk SSSR, 1960)(in Russian).
37. P.G. Klemens, The Scattering of Low-Frequency Lattice Waves by Static Imperfections, *Proc. Phys. Soc*. **A68**, 1113-1128 (1955).
38. P.G. Klemens, Thermal Resistance due to Point Defects at High Temperatures, *Phys. Rev.* **119**, 507-509 (1960).

Submitted 24.07.14

L.I. Anatychuk[1,2], R.R. Kobylianskyi[1,2]

L.I. Anatychuk

[1]Institute of Thermoelectricity of the NAS and MES Ukraine, 1, Nauky Str., Chernivtsi, 58029, Ukraine;
[2]Yu. Fedkovych Chernivtsi National University, 2, Kotsyubinsky Str., Chernivtsi, 58000, Ukraine

R.R. Kobylianskyi

SOME SPECIFIC FEATURES OF DYNAMIC OPERATING MODES OF THERMAL GENERATOR USING HUMAN HEAT

The paper deals with the advisability of using dynamic operating modes of thermoelectric microgenerators for power supply to low-power equipment. The effect of connecting plate geometry and thermal generator dimensions on their energy characteristics is investigated. It is established that dynamic operating modes of short-life thermoelectric power sources are more expedient, since under certain conditions they afford an opportunity to produce twice as high electric power compared to steady-state modes.

Key words: thermoelectric microgenerator, dynamic mode, human heat release, computer simulation.

Introduction

Using human heat for power supply to various low-power electronic devices with the aid of thermoelectric microgenerators generates growing interest [1-6]. There are wrist watches with a thermoelectric power source [7-13], wireless autonomous pulse meters [3, 14], electronic medical thermometers [15-18], wrist oxymeters [19], wireless electroencephalographs [20-22], thermoelectric microgenerators for mounting into clothes [23-26], etc. They can be short-life, such as electronic medical thermometer with a thermoelectric power source measuring human body temperature within several minutes. Indeed, with such devices one does not need much time to get information on human temperature. And the sooner this information is obtained, the more efficient is thermometer operation. Under these conditions, the use of steady-state operating modes may prove to be unjustified. Naturally, steady-state operating mode of a thermoelectric generator after it touches human body generally occurs in several minutes, and to measure human body temperature with electronic medical thermometer it is enough to have several tens of seconds. Therefore, in such cases a thermoelectric microgenerator should be used in transient operating modes that are dealt with in this paper.

1. A physical model of biological tissue with a thermoelectric microgenerator and a heat sink

According to a physical model (Fig. 1), an area of human skin is a structure consisting of three layers (epidermis 1, dermis 2, subcutis 3) and internal tissue 4. This structure is characterized by thermal conductivity κ_i, specific heat C_i, density ρ_i, blood perfusion rate ω_b, blood density ρ_b, blood heat capacity C_b and specific heat release q_{met} due to metabolic processes (Table 1). The respective biological tissue layers 1 – 4 are regarded as the bulk sources of heat q_i, where:

$$q_i = q_{meti} + \rho_b \cdot C_b \cdot \omega_{bi} \cdot (T_b - T), \quad i = 1..4. \tag{1}$$

The geometric dimensions of each such layer are a_i, b_i and l_i. The temperatures at the boundaries of the respective biological tissue layers are T_1, T_2, T_3 and T_4.

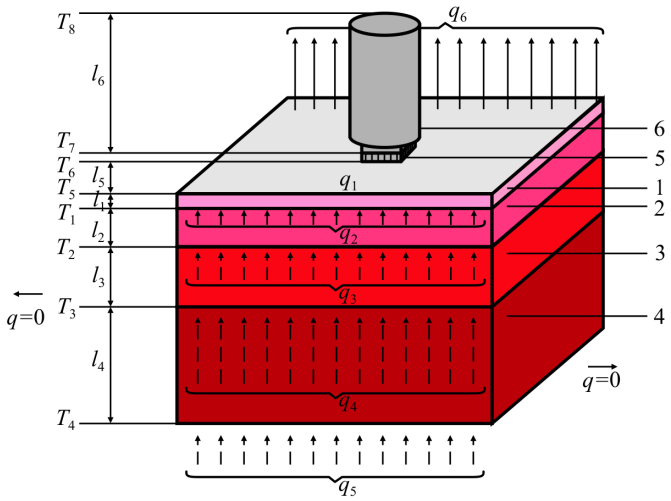

Fig. 1. A physical model of biological tissue with a thermoelectric microgenerator and a heat sink: 1 – epidermis, 2 – dermis, 3 – subcutis, 4 – internal tissue, 5 – thermoelectric microgenerator, 6 – heat sink.

A thermoelectric microgenerator 5 is a rectangular bar with dimensions a_5, b_5, l_5, characterized by thermal conductivity coefficient κ. The thermoelectromotive force of thermoelectric generator is known to be determined as [1, 2]:

$$E = \alpha \cdot N \cdot \Delta T, \tag{2}$$

where α is the Seebeck coefficient, N is the number of thermoelectric material legs, ΔT is temperature difference between the microgenerator's upper and lower surfaces. The number of thermoelectric material legs in the microgenerator is N = 1500 – 3000 pcs. Simulation of a thermogenerator with such a number of elements is an intricate problem even for modern personal computers.

Table 1

Thermophysical properties of human biological tissue [27-31]

Biological tissue layers	Epidermis	Dermis	Subcutis	Internal tissue
Thickness, l (mm)	0.08	2	10	30
Specific heat, S ($J \cdot kg^{-1} \cdot K^{-1}$)	3590	3300	2500	4000
Thermal conductivity, κ ($W \cdot m^{-1} \cdot K^{-1}$)	0.24	0.45	0.19	0.5
Density, ρ ($kg \cdot m^{-3}$)	1200	1200	1000	1000
Metabolism, q_{met} ($W \cdot m^{-3}$)	368.1	368.1	368.3	368.3
Tissue blood perfusion rate, ω_b ($m^3 \cdot s^{-1} \cdot m^{-3}$)	0	0.00125	0.00125	0.00125
Blood density, ρ_b ($kg \cdot m^{-3}$)	1060	1060	1060	1060
Blood heat capacity, C_b ($J \cdot kg^{-1} \cdot K^{-1}$)	3770	3770	3770	3770

At the same time, from formula (2) it is evident that the thermogenerator's EMF value is mainly influenced by temperature difference ΔT between its surfaces. Therefore, to reach the purpose set in this paper, it is quite sufficient to replace a thermoelectric microgenerator having a large number of elements by the bulk homogeneous sample of equivalent thermal conductivity κ. Then, on the basis of calculated ΔT, one can easily determine the microgenerator's EMF according to formula (2).

The thermoelectric microgenerator 5 with geometric dimensions a_5, b_5, l_5 and contact surface temperature T_6 is located on the surface of biological tissue (epidermis 1) with temperature T_5. The thermoelectric microgenerator 5 is in the state of heat exchange with heat sink 6 of high thermal conductivity material with geometric dimensions a_6, b_6, l_6 and contact surface temperature T_7.

Free surface of skin area (epidermis 1) is in the state of heat exchange with the environment with temperature T_8 which is taken into account by heat exchange coefficient α. The rest of free surfaces of thermoelectric micogenerator 5 and heat sink 6 are adiabatically isolated. The specific heat flux from the free skin surface is q_6, and the specific heat flux from the internal human bodies is q_5. Skin heat exchange due to radiation and perspiration is disregarded.

As long as a physical model is an area of a four-layered biological tissue, with identical biochemical processes occurring in adjacent layers, it can be assumed that there is no heat overflow through the lateral surface of biological tissue ($q = 0$).

2. Mathematical description of the model

As long as this research aims at studying the dynamics of physical processes in a thermoelectric microgenerator since the moment it is brought into thermal contact with the skin surface, one must know the steady-state distribution of temperature in biological tissue in the absence of microgenerator on its surface. Such temperature distribution should be chosen as the initial conditions in biological tissue in the process of thermal interaction between thermoelectric microgenerator and biological tissue. This, in turn, means that the research should be performed in two steps. At the first step it is necessary to find the steady-state temperature distribution in biological tissue in the absence of a microgenerator on its surface. At the second step – the dynamic temperature distribution in biological tissue and the thermoelectric microgenerator and heat sink located on its top, assuming as the initial conditions for biological tissue the temperature distribution found at the first step.

A general equation of heat exchange in biological tissue is as follows [27-31]:

$$\rho_i \cdot C_i \cdot \frac{\partial T}{\partial t} = \nabla(\kappa_i \cdot \nabla T) + \rho_b \cdot C_b \cdot \omega_{b_i} \cdot (T_b - T) + q_{met_i}, \tag{3}$$

where $i = 1...4$ are corresponding layers of biological tissue, ρ_i is the density of corresponding biological tissue layer (kg/m^3), C_i is specific heat of corresponding biological tissue layer (J/kg·K), ρ_b is blood density (kg/m^3), C_b is specific heat of blood (J/kg·K), ω_{bi} is blood perfusion rate of corresponding biological tissue layer (m^3·s^{-1}·m^{-3}), T_b is human blood temperature (°C), where $T_b = 37$ °C, q_{meti} is the amount of metabolic heat of corresponding biological tissue layer (W/m^3), T is absolute temperature (K), κ_i is thermal conductivity coefficient of corresponding biological tissue layer (W/m·K), t is time (s).

The summand in the left-hand side of equation (3) is the rate of change in thermal energy comprised in the unit volume of biological tissue. Three summands in the right-hand side of this equation are the rate of change in thermal energy due to thermal conductivity, blood perfusion and metabolic heat, respectively.

At the first step of research $\frac{\partial T}{\partial t} = 0$, so Eq.(3) is simplified as:

$$\nabla(\kappa_i \cdot \nabla T) + \rho_b \cdot C_b \cdot \omega_{b_i} \cdot (T_b - T) + q_{met_i} = 0. \tag{4}$$

Steady-state equation of heat exchange in biological tissue (4) is solved with the boundary conditions (5) yielding the distribution $T(x, y, z)$

$$\begin{cases} q\big|_{x=0}=0, \\ q\big|_{x=a}=0, \end{cases} \begin{cases} q\big|_{y=0}=0, \\ q\big|_{y=a}=0, \end{cases} \begin{cases} T\big|_{z=0}=37\ ^\circ\mathrm{C}, \\ q\big|_{z=b}=\alpha\cdot(T_0-T), \end{cases} \tag{5}$$

where q is heat flux density, T is absolute temperature, T_0 is ambient temperature, α is heat exchange coefficient.

At the second step, a dynamic temperature distribution in the biological tissue is found by solving Eq.(3) with the boundary conditions (5) and the initial temperature distribution $T(x, y, z)$. In so doing, in thermoelectric microgenerator and heat sink we solve a general equation of heat exchange [1, 2, 32]:

$$\rho_i \cdot C_i \cdot \frac{\partial T}{\partial t} = \nabla(\kappa_i \cdot \nabla T), \tag{6}$$

where $i = 5, 6$ is thermal generator and heat sink material, ρ_i is substance density, C_i is substance specific heat, κ_i is thermal conductivity coefficient. The boundary conditions for Eq.(6) include adiabatic insulation of surfaces of thermoelectric microgenerator and the initial temperature distribution $T = \text{const} = T_{amb.}$

3. Computer simulation

To study the dynamic operating modes of thermoelectric microgenerators using human heat, a three-dimensional computer model of biological tissue was created having on its top a thermoelectric microgenerator and a heat sink. The computer model was constructed with the aid of Comsol Multiphysics applied program package [33] allowing simulation of thermophysical processes in biological tissue with regard to blood circulation and metabolism.

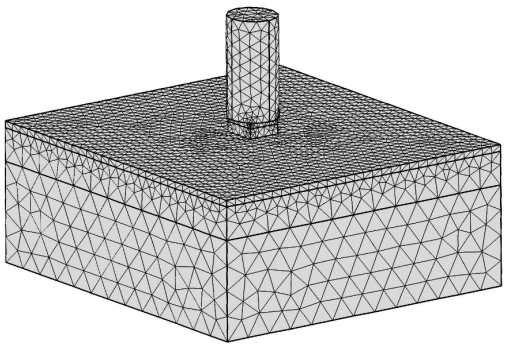

Fig. 2. Finite element method mesh.

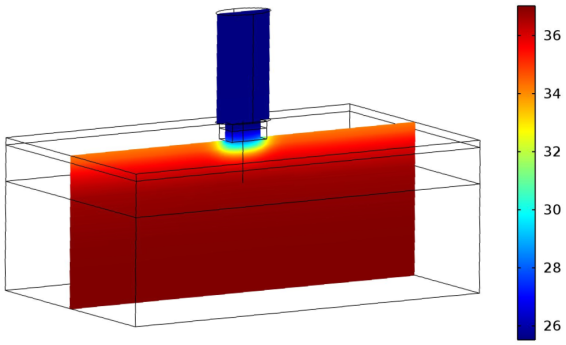

Fig. 3. Temperature distribution in the section of human biological tissue having on its top a thermoelectric microgenerator and heat sink.

The distribution of temperature and heat flux density in the biological tissue, thermoelectric microgenerator and heat sink was calculated by the finite element method (Fig. 2). According to this method, an object under study is split into a large number of finite elements, and in each of them the value of function is sought which satisfies given differential equations of second kind with the respective boundary conditions. The accuracy of solving the formulated problem depends on the level of splitting and is assured by using a large number of finite elements [33].

Object-oriented computer simulation was used to obtain the distributions of temperature (Fig. 3) and heat flux density lines in human biological tissue, thermoelectric microgenerator and heat sink.

4. Computer simulation results

Figs. 4, 5 represent a dynamics of change in EMF and electric power of thermoelectric microgenerators (with dimensions 10 × 10 mm, 15 × 15 mm, 20 × 20 mm) using human heat at ambient temperatures $T = (20 \div 36)$ °C with and without regard to blood circulation in biological tissue.

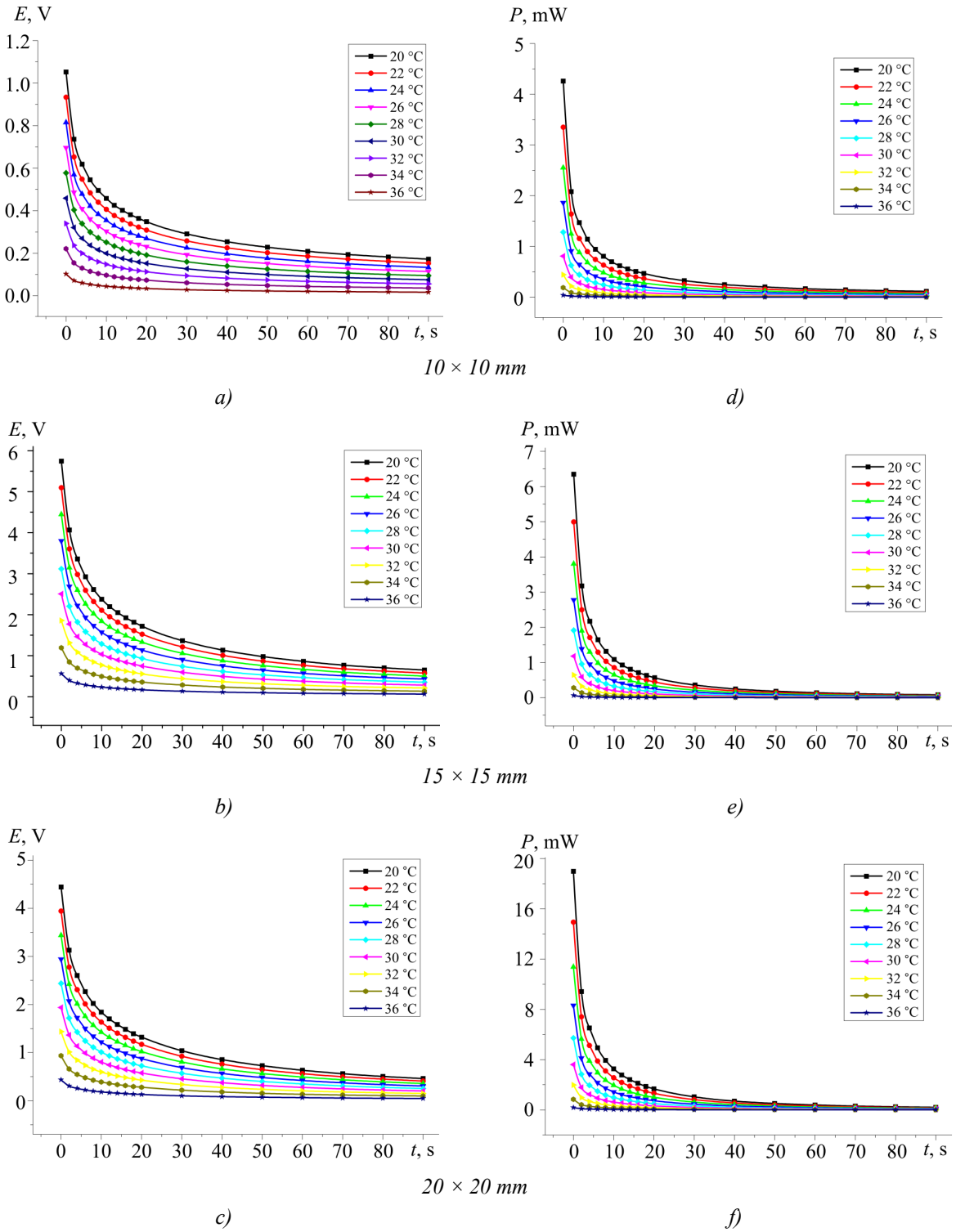

Fig. 4. Dynamics of change in EMF (a, b, c) and electric power (d, e, f) of thermoelectric microgenerator without regard to blood circulation in biological tissue: a), d) for microgenerator with dimensions 10 × 10 mm; b), e) for microgenerator with dimensions 15 × 15 mm; c), f) for microgenerator with dimensions 20 × 20 mm.

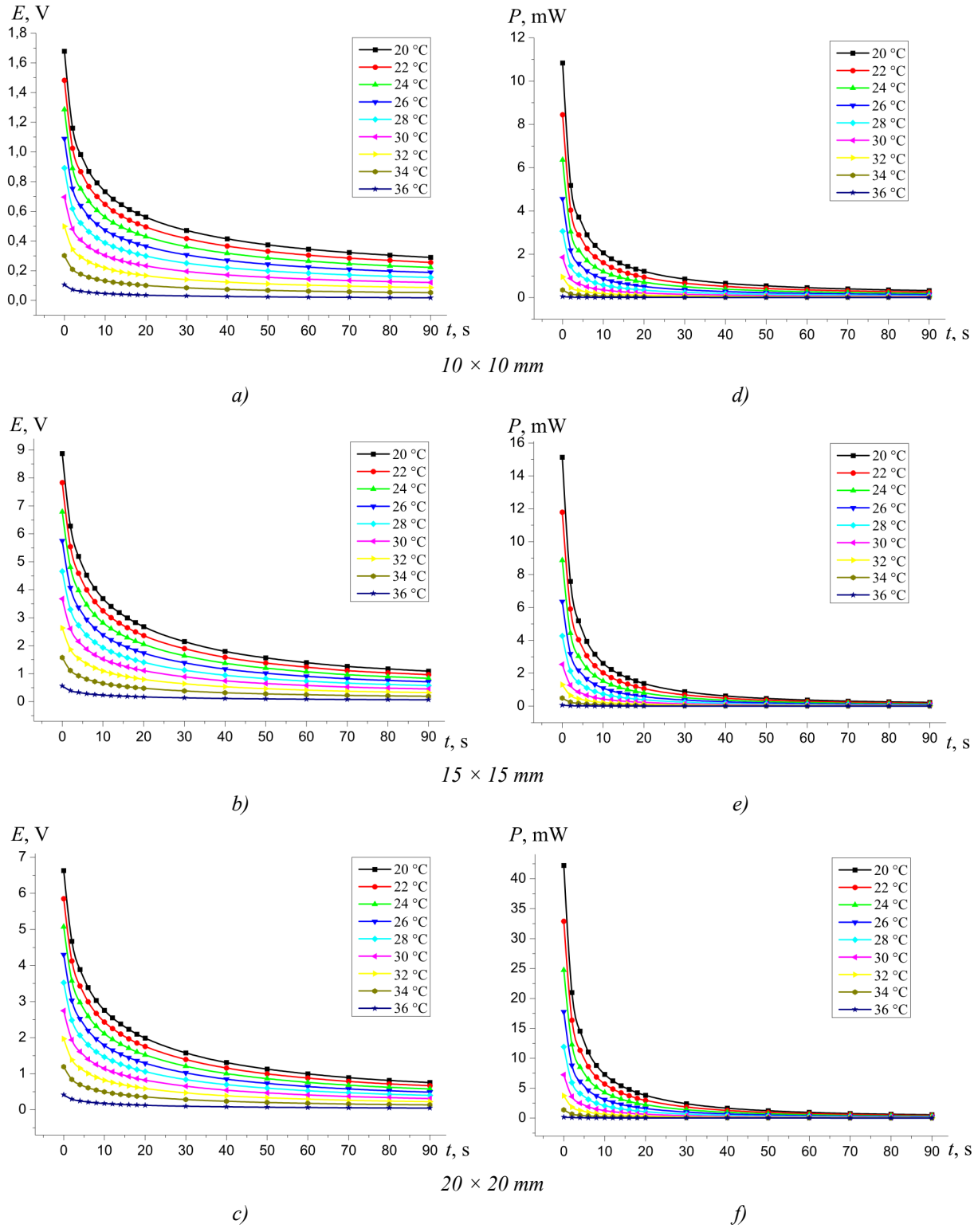

Fig. 5. Dynamics of change in EMF (a,b, c) and electric power (d, e, f) of thermoelectric microgenerator with regard to blood circulation in biological tissue: a), d) for microgenerator with dimensions 10 × 10 mm; b), e) for microgenerator with dimensions 15 × 15 mm; c), f) for microgenerator with dimensions 20 × 20 mm.

Analyzing Figs. 4, 5, we see that blood circulation in biological tisue affects considerably the energy charactertistics of thermoelectric microgenerators. Thus, for instance, for the case of a thermal generator with dimensions 10 × 10 mm the EMF differs by a factor of 1.6, and electric power P – by a

factor of 2.6; for the case of 15 × 15 mm the EMF differs by a factor of 1.55, and electric power P – by a factor of 2.4; and for the case of 20 × 20 mm the EMF differs by a factor of 1.5, and electric power P – by a factor of 2.2. Thus, with increasing dimensions of thermoelectric microgenerator, the influence of blood circuilation in biological tissue on its energy characteristics is reduced.

5. Experimental investigations

5.1. Experimental procedure

To perform experimental investigations of the dynamic modes of thermoelectric microgenerators, samples with dimensions 10 × 10 mm, 15 × 15 mm, 20 × 20 mm and their respective hollow copper heat sinks with pipes for pumping thermostated liquid through them were made. Characteristics of thermoelectric microgenerators are given in Table 2. For liquid thermostating a thermoelectric thermostat was used that allows keeping given liquid temperature to an accuracy of ± 0.1 °C. Thus, thermostated copper heat sinks imitate thermal effect of environment on thermoelectric microgenerator.

As a source of heat, the surface of human skin in armpit area was used (typical zone of human body temperature measurement).

Table 2

Characteristics of experimental samples of thermoelectric microgenerators

Characteristics of microgenerators	Sample 1	Sample 2	Sample 3
Microgenerator dimensions, mm	10 × 10	15 × 15	20 × 20
Number of legs, pcs	624	3440	2496
Electric resistance R, Ω	130	2600	520
Dimensions of legs, mm	0.35 × 0.35 × 3	0.2 × 0.2 × 3	0.35 × 0.35 × 3

Digital multimeter M3500A connected to a personal computer was used to register the dynamics of change in the EMF of thermoelectric microgenerators within 90 seconds since the moment of their application to skin surface. Based on the measured values of EMF E, full power P of thermoelectric microgenerators was calculated according to expression:

$$P = \frac{E^2}{2 \cdot R}. \tag{7}$$

5.2. Experimental results

Fig. 6 shows a dynamics of change in the EMF and electric power of experimental thermoelectric microgenerators at ambient temperatures $T = (24 \div 34)$ °C.

As a result of analysis of Figs. 4, 5 a feature common to all calculated curves has been revealed that is not typical of the dynamic operating conditions of experimental thermoelectric microgenerators. It lies in the fact that the calculated values of microgenerator energy characteristics are maximum at the initial time instant when thermoelectric generator makes contact with skin surface.

However, in fact it is clear that characteristics of microgenerator under isothermal conditions are equal to zero, including the moment of contact to skin surface, which is confirmed by experimental data (Fig. 6).

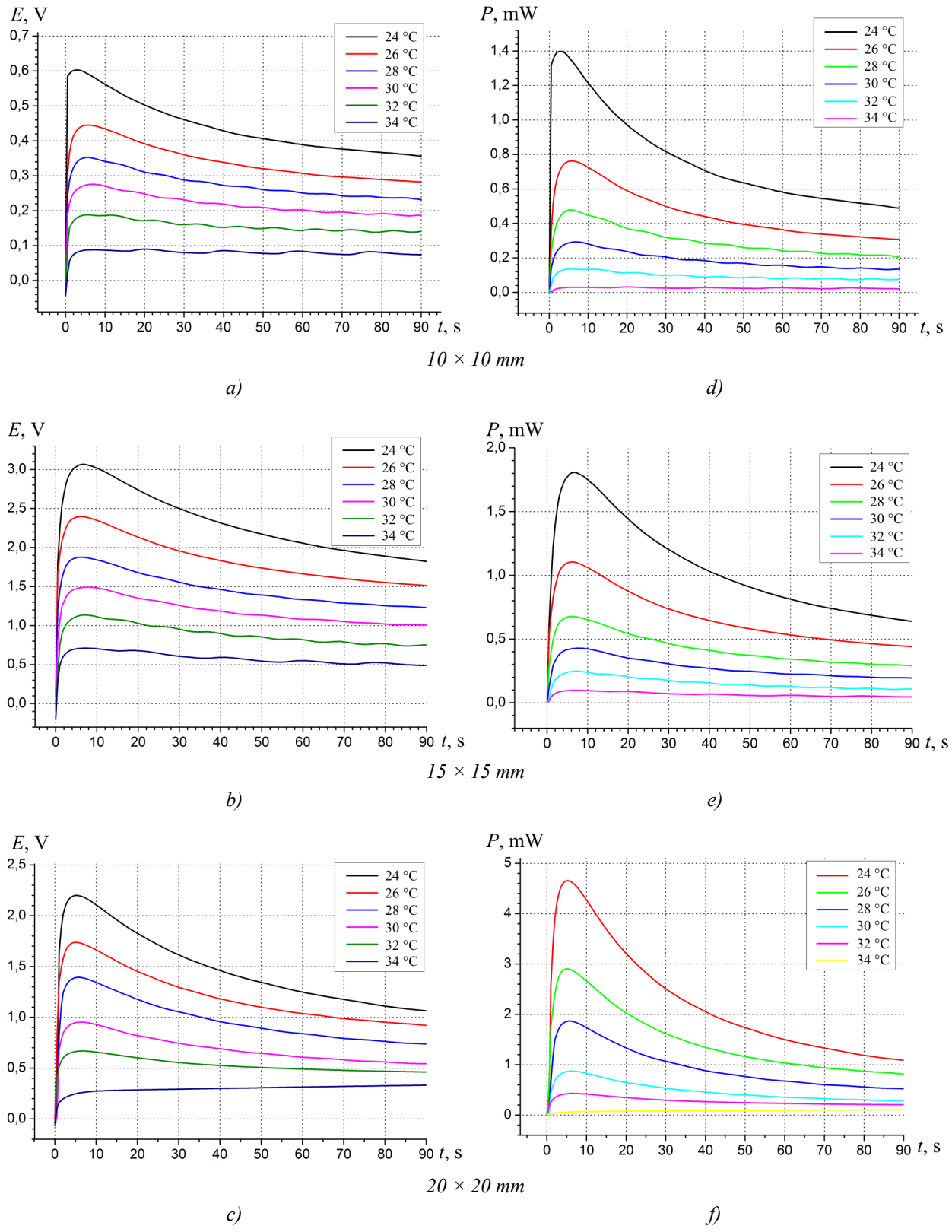

Fig. 6. Dynamics of change in the EMF (a,b, c) and electric power (d, e, f) of experimental thermoelectric microgenerators: a), d) microgenerator with dimensions 10 × 10 mm; b), e) microgenerator with dimensions 15 × 15 mm; c), f) microgenerator with dimensions 20 × 20 mm.

Apparently this peculiarity is due to imperfection of physical model, namely the absence from the side of contact between thermoelectric microgenerator and skin surface of a connecting layer which is an additional thermal capacity, resulting in reduction of thermal flux through microgenerator, hence, microgenerator characteristics. Moreover, a more real physical model should take into account a transient thermal layer between connecting plates and skin, however, to begin with, we will neglect it, since it is unkown.

Therefore, the constructed physical model should be improved through account of additional element, namely connecting layer (interlayer of POS-61 solder in the form of plates connecting thermogenerator legs) on the side of contact between thermoelectric microgenerator and skin surface.

6. Account of connecting plates and comparison of the results

Due to a divergence between the experimental data and the results of computer simulation, a physical model on the side of contact between thermoelectric microgenerator and surface skin was complemented with a continuous layer of POS-61 solder, assuring connection of legs. Following that, repated calculations of the energy characteristics of thermoelectric microgenerators were made that confirmed the assumption on the importance of this layer. A partial case of such comparison is given in Fig. 10 – 11 for a thermoelectric microgenerator with dimensions 15 × 15 mm at ambient temperature T = 24 °C.

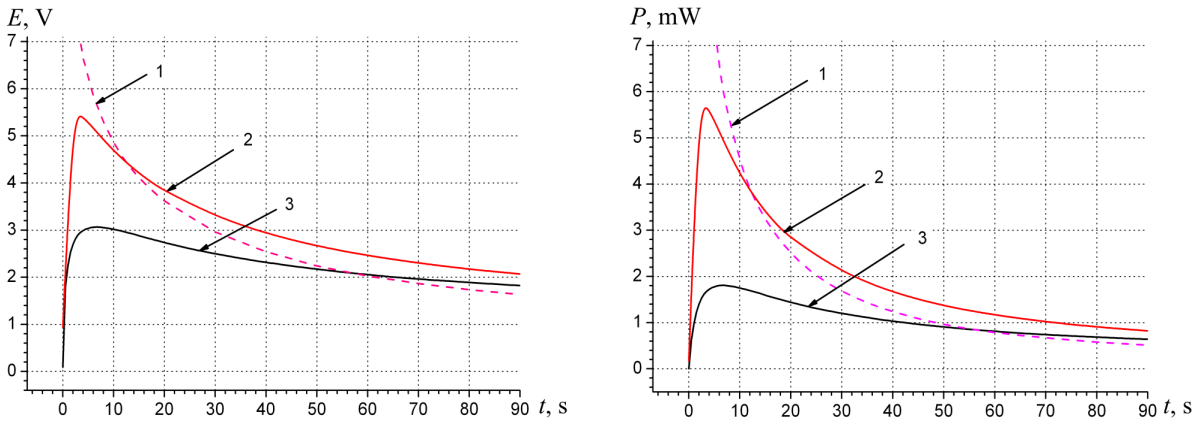

Fig. 7. Comparison of calculated and experimental results of EMF (a) and electric power (b) time dependence for a thermoelectric microgenerator with dimensions 15 × 15 mm with regard to connecting plates. (1 –computer simulation without regard to connecting layer;2 – computer simulation with regard to connecting layer; 3 – experiment).

The resulting coincidence between the experiment and computer calculations without regard in the model of a transient thermal layer between thermal generator surface and skin testifies that the effect of this layer is minor.

As is evident from Fig.7, on the calculated curve there is an optimum whose maximum value differs from the experimental data for EMF by 45 %, for electric power by 68 %. However, in this case the divergence between the calculated and experimental data remains insatisfactory, which is probably due to connecting plates geometry.

7. Account of the effect of geometry of connecting plates and comparison of the results

As is known, technology of legs connection provides for formation on the surface of thermoelectric microgenerators an array of plane-convex solder droplets with their subsequent grinding. Finally, a typical connecting plate assumes a shape that can be pretty exactly described in Fig. 8. This figure shows dimensions of connecting plates averaged from the measurements of experimental samples of thermoelectric microgenerators 1 – 3.

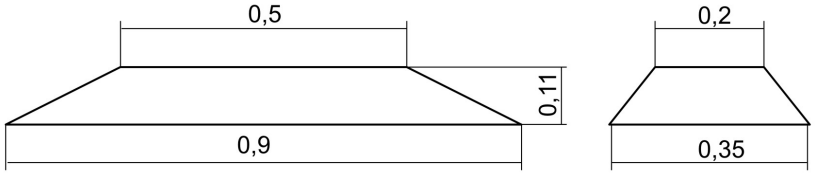

Fig. 8. Geometry of connecting plate of thermoelectric microgenerator.

With regard to geometry of connecting plates, computer simulation yielded specified energy characteristics of thermoelectric microgenerators, in particular, for a microgenerator with dimensions 15 × 15 mm (Fig. 9).

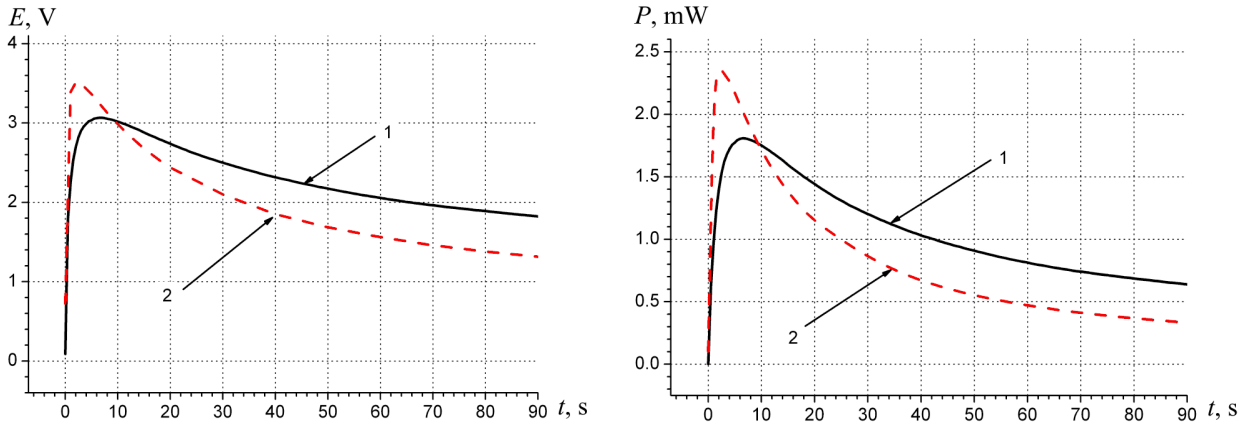

a) *b)*

Fig. 9. Comparison of calculated and experimental results of EMF (a) and electric power (b) time dependence for a thermoelectric microgenerator with dimensions 15 × 15 mm with regard to geometry of connecting plates. (1 –experiment; 2 – computer simulation with regard to geometry of connecting layer).

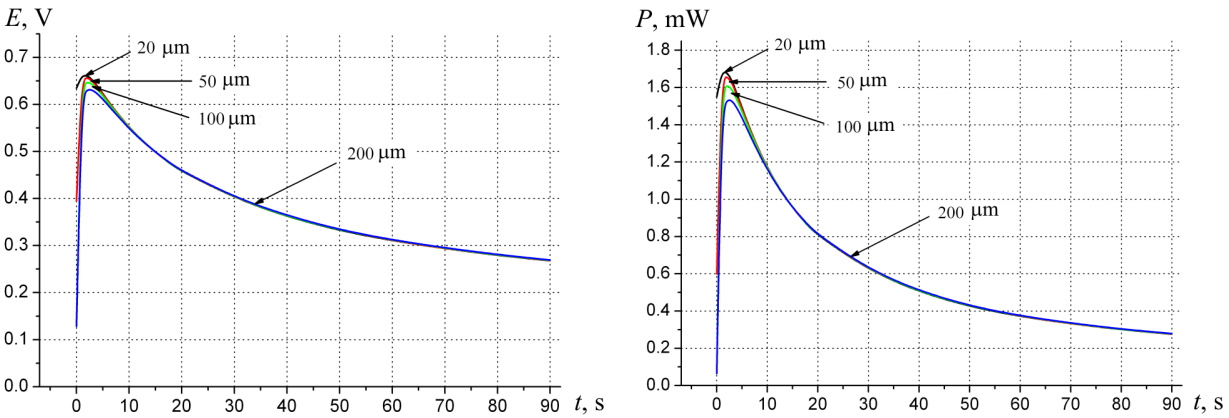

a) *b)*

Fig.10.Time dependence of EMF (a) and electric power (b) for a thermoelectric microgenerator with dimensions 10 × 10 mm for connecting plates of dissimilar thickness.

The effect of connecting plate thickness (20 μm, 50 μm, 100 μm, 200 μm) on the energy characteristics of thermoelectric microgenertaors was also investigated. As an example, Fig. 10 shows the influence of connecting plate thickness on the EMF and power of thermoelectric microgenerator with dimensions 10 × 10 mm at ambient temperature T = 24 °C.

As is evident from the plots in Fig. 10, a 10-fold change in connecting plate thickness leads to a change in EMF and electric power by 5 % and 9 %, respectively. Thus, the effect of connecting plate thickness on the energy characteristics of thermoelectric microgenerators is minor.

8. Typical time dependence of the electric energy of thermoelectric microgenerator in dynamic mode

From the curve of dynamics of electric energy storage of thermoelectric microgenerator (Fig. 11) it is seen that at the beginning of transient process the rate of electric energy storage is 2 times higher than several tens of seconds. Therefore, for a rational use of such thermoelectric microgenerator it is desirable to use special integrated electronic circuits with electric voltage stabilization and energy storage.

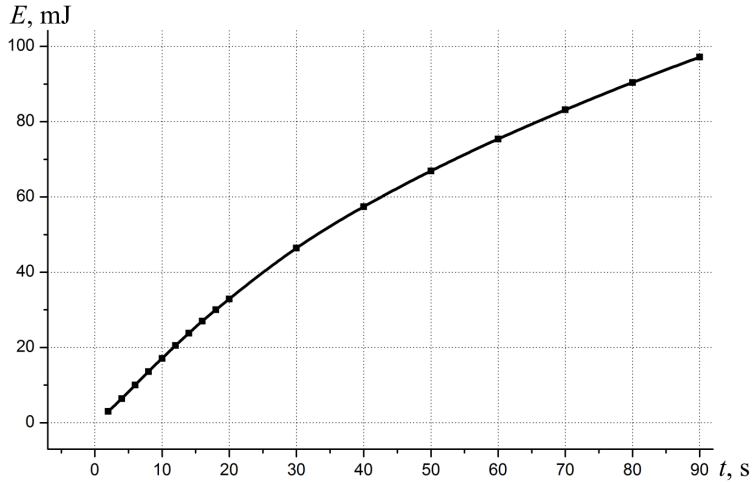

Fig. 11. Dynamics of electric energy storage of thermoelectric microgenerator with dimensions 10 × 10 mm.

9. The effect of thermoelectric microgenerator dimensions on its electric power

It is noteworthy that the work of thermoelectric microgenerator using human heat is essentially affected by its dimensions. The value of electric power is not proportional to the area of such thermal generator. With increasing area, its specific electric power is decreased. It is due to reduced effect of blood circulation bringing heat to thermal generator. Therefore, apparently it is more reasonable to use a series of thermoelectric microgenerators on given area of human body than one solid microgenerator, since in the latter case the efficiency is reduced. Moreover, arrangement of a good thermal contact is complicated. However, a study of this factor can be the subject of separate investigation.

Conclusions

1. The results of investigations confirm that when using dynamic modes at the initial steps of thermoelectric microgenerator heat-up, the released electric energy is larger than in steady-state modes. When considering a specific model it was obtained that on achieving maximum (about 5 seconds) the value of electric power is twice that in the steady-state case, which confirms the rationality of using a transient mode in short-life thermal generators.
2. In connection with a relatively low skin thermal conductivity and the fact that the experiment employed thermoelectric microgenerators where the area of connecting plates is somewhat smaller than the area of legs, the values of EMF and electric power are essentially dependent on the area of

contacting surface. Therefore, in the manufacture of such microgenerators care should be taken that the surface of contact between skin and thermal generator be maximum within each leg.

3. The resulting coincidence between the experiment and computer calculations with no account in the model of transient thermal layer between thermal generator surface and skin testifies that the effect of this layer is minor.
4. In thermoelectric microgenerators using the initial transient mode in contrast to steady-state mode it is heat sink capacity that has a dominant role in heat removal, rather than heat exchange with the environment. The latter is positive, since under such conditions one can use not heat sinks, but media with maximum possible heat capacity and thermal conductivity.

References

1. L.I. Anatychuk, *Thermoelements and Thermoelectric Devices: Handbook* (Kyiv: Naukova Dumka, 1979), 768 p.
2. L.I. Anatychuk, *Thermoelectricity, Vol. 2, Thermoelectric Power Converters* (Kyiv, Chernivtsi: Institute Thermoelectricity, 2003), 376 p.
3. L.T. Strutynska, Thermoelectric Microgenerators. State of the Art and Application Potential, *Tekhnologiya i Konstruirovaniye v Elektronnoi Apparature* **4**, 5 – 13 (2008).
4. V. Leonov and R.J.M. Vullers, Wearable Electronics Self-powered by Using Human Body Heat: The State of the Art and the Perspective, *J. Renewable and Sustainable Energy* **1**, 062701 (2009).
5. M. Lossec, B. Multon, H. Ben Ahmed, and C. Goupil, Thermoelectric Generator Placed on the Human Body: System Modeling and Energy Conversion Improvements, *Eur. Phys. J. Appl. Phys.* **52**, 11103 (2010).
6. Y. Yang, J. Liu, Evaluation of the Power-Generation Capacity of Wearable Thermoelectric Power Generator, *Front. Energy Power Eng. China* 4 (3), 346 – 357 (2010).
7. *Pat. 4106279 USA*, Wrist Watch Incorporating a Thermoelectric Generator /J. Martin and C. Piguet, 1978.
8. Pat. 6222114 USA, Portable Wrist Device/Mitamura Gen, 2001.
9. J. Paradiso, T. Starner, Human Generated Power for Mobile Electronics, *Low Power Electronics Design*, CRC Press, Fall 2004.
10. J. Paradiso, Energy Scavenging for Mobile Computing, *Responsive Environments Group. MIT Media Lab*. http://www.media.mit.edu/resenv.
11. J. Paradiso, T. Starner, Energy Scavenging for Mobile and Wireless Electronics, *IEEE CS* 5, 18 – 27 (2005).
12. G.J. Snyder, Small Thermoelectric Generators, *The Electrochemical Society Interface*, Fall 2008, p. 54 56.
13. K. Matsuzawa and M. Saka, Seiko Human Powered Quartz Watch. In *M. Rose, editor, Prospector IX: Human-Powered Systems Technologies, pages 359-384, Auburn, AL, November 1997. Space Power Institute, Auburn Univ.*
14. *Application for Utility Model* № u201315451 of 30.12.13, Pulse Meter with a Thermoelectric Power Supply /L.I.Anatychuk, R.R.Kobylianskyi, 2013.
15. *Patent of Ukraine 87400, InCl H01L 35/00*, Electronic Medical Thermometer with a Thermoelectric Power Supply / L.I. Anatychuk, R.R. Kobylianskyi, and S.B. Romanyuk, № u 2013 08794; filed 15.07.13; publ. 10.02.14, Bul. № 3.

16. L.I. Anatychuk, R.R. Kobylianskyi, On the Accuracy of Temperature Measurement by Electronic Medical Thermometer with Thermoelectric Power Supply, *J. Thermoelectricity* **5**, 75 – 79 (2013).
17. L.I. Anatychuk, R.R. Kobylianskyi, and I.A. Konstantinovich, The Effect of Thermoelectric Power Source on the Accuracy of Temperature and Heat Flux Measurement, *J. Thermoelectricity* **6**, 53 – 62 (2013).
18. L.I. Anatychuk, R.R. Kobylianskyi, and I.A. Konstantinovich, Thermoelectric Power Source for Electronic Medical Thermometer, *Tekhnologiya i Konstruirovaniye v Elektronnoi Apparature* 2 (2014).
19. Vladimir Leonov and Ruud J. M. Vullers. Wearable electronics self-powered by using human body heat: The state of the art and the perspective. // Journal Of Renewable And Sustainable Energy. - 1, 2009.
20. Julien Penders, Bert Gyselinckx, and Ruud Vullers, *Human: from Technology to Emerging Health Monitoring Concepts*, Holst Centre / IMEC-NL.
21. Vladimir Leonov, Tom Torfs, Ruud J.M. Vullers and Chris Van Hoof, Hybrid Thermoelectric-Photovoltaic Generators in Wireless Electroencephalography Diadem and Electrocardiography Shirt, *J. Electronic Materials 39* (9), 2010.
22. Vladimir Leonov and Ruud J. M. Vullers. Wearable electronics self-powered by using human body heat: The state of the art and the perspective. // Journal Of Renewable And Sustainable Energy. - 1, 2009.
23. Vladimir Vladimir Leonov, Tom Torfs, Chris Van Hoof, and Ruud J. M. Vullers, Smart Wireless Sensors Integrated in Clothing: an Electrocardiography System in a Shirt Powered Using Human Body Heat, *Sensors & Transducers Journal* **107** (8), 165 – 176 (2009).
24. Christl Lauterbach, Marc Strasser, Stefan Jung, and Werner Weber. *'Smart Clothes' Self-Powered by Body Heat, Infineon Technologies AG, Corporate Research, Emerging Technologies, Munich, Germany.* http://www.infineon.com.
25. A. Samarin, Electronics Embedded in Clothes, *Komponenty i Tekhnologii* **4**, 221 – 228 (2007).
26. A. Samarin, Electronics Embedded in Clothes – Technologies and Prospects, *Komponenty i Tekhnologii* **5**, 146 – 152 (2007).
27. S.C. Jiang, N. Ma, H.J. Li, and X.X. Zhang, Effects of Thermal Properties and Geometrical Dimensions on Skin Burn Injuries, *Burns* **28**, 713 – 717 (2002).
28. M.P. Cetingul, C. Herman, Identification of Skin Lesions from the Transient Thermal Response Using Infrared Imaging Technique, *IEEE*, 1219 – 1222 (2008).
29. M. Ciesielski, B. Mochnacki, and R. Szopa, Numerical Modeling of Biological Tissue Heating. Admissible Thermal Dose, *Scientific Research of the Institute of Mathematics and Computer Science* **1** (10), 11 – 20 (2011).
30. Florin Filipoiu, Andrei Ioan Bogdan and Iulia Maria Carstea, Computer-Aided Analysis of the Heat Transfer in Skin Tissue, *Proceedings of the 3rd WSEAS Int. Conference on Finite Differences - Finite Elements - Finite Volumes - Boundary Elements*, 2010, p. 53-59.
31. Daniela Carstea, Ion Carstea, and Iulia Maria Carstea, Interdisciplinarity in Computer-Aided Analysis of Thermal Therapies, *WSEAS Transactions on Systems and Control* **6** (4), 115-124 (2011).
32. V.A. Grigoryev, V.M.Zorin, *Heat-and-Mass Transfer. Heat Engineering Experiment: Handbook* (Moscow: Energoizdat, 1982), 512 p.
33. COMSOL Multiphysics User's Guide, COMSOLAB, 2010, 804 p.

Submitted 24.06.14

R.G.Cherkez

R.G.Cherkez

Institute of Thermoelectricity of the NAS and MES Ukraine,
1 Nauky str., Chernivtsi, 58029, Ukraine

PERMEABLE GENERATOR THERMOELEMENTS OF *Co-Sb* BASED MATERIALS

Results of computer investigations of permeable themoelements based on Co-Sb are presented. Optimal parameters and concentrations of doping impurities whereby maximum efficiency of thermal into electric energy conversion is accomplished are determined. Possibility of 1.1-1.3-fold efficiency increase of permeable thermoelements of Co-Sb based materials as compared to conventional ones is demonstrated.

Key words: *permeable thermoelements, computer design, Co-Sb based materials.*

Introduction

The use of thermal waste from industry and internal combustion engines is a promising line of solving the tasks of conservation of energy resources [1]. Attractive properties of thermoelectric method of direct thermal into electric energy conversion, namely the absence of movable parts and possibility of functioning under extreme conditions, make thermoelectric generators advantageous over the others. In so doing, it is customary to use thermoelectric modules of homogeneous materials whose maximum value of thermoelectric figure of merit is achieved in a rather narrow temperature range [2]. This is responsible for insufficient efficiency of thermoelectric power converters, hence restricts the possibilities of their practical use.

In recent decade, increasing researchers' attention has been drawn to promising thermoelectric materials based on *Co-Sb* [3]. They are ecologically safe and characterized by rather high values of the Seebeck coefficient and electric conductivity with maximum values of a dimensionless parameter of thermoelectric figure of merit *ZT* at a level of 1 – 1.1 in the temperature range of 700 – 750 K [4-5].

At the same time, growing interest has been observed recently in the study of permeable thermoelements, where heat input and removal occurs not only on the junctions, but also due to the use of a developed heat exchange surface in the bulk of legs material [6]. Such thermoelements are made permeable for pumping gas or liquid flows, which allows improving the efficiency of thermoelectric energy conversion. The use of permeable structures in thermoelectric modules with *Bi-Te* made it possible to improve the efficiency of energy conversion by 30 % [7].

However, the use of permeable thermoelements of promising materials based on *Co-Sb* has received no attention in the literature. Therefore, the purpose of this work is to determine characteristics of permeable generator thermoelements based on *Co-Sb*, to reveal their optimal thermophysical and design parameters whereby maximum efficiency of thermal into electric energy conversion is realized.

A physical model and its mathematical description

A physical model of a permeable thermoelement in electric energy generation mode is represented in Fig. 1. The thermoelement consists of *n*- and *p*-type legs whose physical properties are temperature-

dependent. Heat input is realized by passing heat carrier along the legs through the channels (pores). Each leg comprises N_n and N_p – segments, respectively, the contact resistance of compound is r_0. The lateral surfaces of the legs are adiabatically isolated; heat carrier temperature at thermoelement inlet T_m is assigned. The temperature of cold junctions T_c is thermostated.

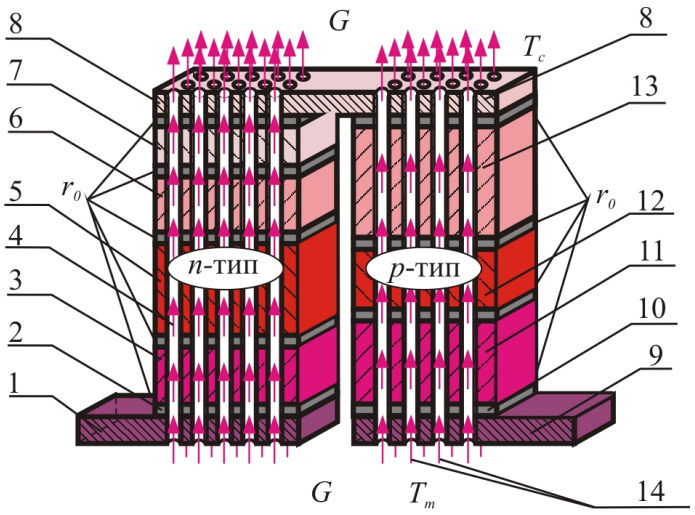

Fig. 1.A physical model of a permeable segmented thermoelement.
1, 8, 9 – connecting plates; 2, 10 –connecting layers;
3, 5, 6, 7 – segments (sections) of n-type leg; 4, 14 – heat carrier;
11, 12, 13 –segments (sections) of p-type leg.

A system of differential equations describing the distribution of temperatures and heat fluxes in a steady-state one-dimensional case, in the infinitely small part dx of each k-th segment of n- and p-type legs, in the dimensionless coordinates is given by relations [7]:

$$\left.\begin{aligned} \frac{dT}{dx} &= -\frac{\alpha_k j}{\kappa_k} T - \frac{j}{\kappa_k} q, \\ \frac{dq}{dx} &= \frac{\alpha_k^2 j}{\kappa_k} T + \frac{\alpha_k j}{\kappa_k} q + j\rho_k + \frac{\alpha_T \Pi_K^1 N_K l_K^2}{(S - S_K) j}(t - T), \\ \frac{dt}{dx} &= \frac{\alpha_T \Pi_K^1 N_K l_k}{G c_P}(t - T), \end{aligned}\right\}_{n,p} \quad \begin{aligned} &k = 1, \ldots, N_{n,p} \\ &x_{k-1} \le x \le x_k \end{aligned} \tag{1}$$

where Π_K^1 is channel perimeter; N_K is the number of channels, S_K is cross-sectional area of all the channels, S is section of a leg together with the channels, G is heat carrier expenditure in the channels, c_P is specific heat of heat carrier, t is heat carrier temperature at point x, T is leg temperature at point x, α_T is heat-transfer coefficient, α, κ, ρ are the Seebeck coefficient, thermal conductivity and resistivity of leg material.

Specific heat fluxes q and the reduced density of electric current j are determined through

$$q = \frac{Q}{I}, \qquad j = \frac{Il}{S}, \tag{2}$$

where Q is power of heat flux passing through thermoelement leg, I is electric current, S is cross-sectional area of thermoelement legs.

The boundary conditions necessary for solving (1) with regard to the Joule-Lenz heat release due to contact resistance r_0 at points of connection of leg segments are formulated as:

$$T_{n,p}(0)=T_C, \qquad t_{n,p}(1)=T_m, \qquad q_{n,p}(1)=0,$$
$$T_{n,p}(x_k^+)=T_{n,p}(x_k^-), \qquad q_{n,p}(x_k^+)=q_{n,p}(x_k^-)+\frac{r_0}{S_{n,p}}I, \tag{3}$$

where indices "-" and "+" denote the value of functions immediately to the left and right of the interface of segments x_k; $k = 1, \ldots, N$ is the index which determines leg segment number.

In the case of search for optimal values of doping impurities which determine carrier concentrations in leg segments it is necessary to assign the dependences of material parameters α, κ, ρ on temperature and concentration of carriers (or impurities).

The main task in the design of a permeable segmented generator thermoelement is to determine such agreed parameters (reduced current density j in the legs, heat carrier expenditures in channels G, concentration of doping impurities in materials of each segment whereby the efficiency of thermoelement reaches a maximum.

The efficiency will be determined through the relation of electric power P generated by the thermoelement to a change in heat carrier enthalpy:

$$\eta=\frac{P}{\sum_{n,p} Gc_p(T_m-T_C)}. \tag{4}$$

The maximum efficiency can be conveniently reduced to achievement of functional minimum:

$$J=\ln\left[\sum_{n,p}\{Gc_P(T_m-T_C)\}\right]-\ln\left[\sum_{n,p}\left\{Gc_P(T_m-t(0))+q(0)\frac{j(S-S_K)}{l}-I\left(\frac{r_0}{S_n}+\frac{r_0}{S_p}\right)\right\}\right]. \tag{5}$$

This problem was solved through use of the Pontryagin maximum principle [8] on which basis the relations giving the necessary optimality conditions were obtained. Such procedure as applied to thermoelectric energy conversion was described in many works, for instance, [9, 10], and was used for creation of computer program and study of a permeable thermoelement made of *Co-Sb* based thermoelectric materials [11].

Results of computer investigation of the energy characteristics of a permeable segmented generator thermoelement based on *Co-Sb*

Experimental data on the dependences of parameters α, κ, σ of *Co-Sb* based materials on the temperature and doping [12, 13] were approximated as polynomial dependences (Fig. 2) and used in computer investigation program. Calculation of a permeable segmented thermoelement was done under conditions when heat exchange coefficient of heat carrier – gas in the channels was assumed to be equal to $\alpha_T = 0.01$ W/cm^2·K, which is achieved in the channels with diameter 0.02 – 0.2 cm at a laminar motion of heat carrier and is a typical value of heat exchange coefficient under such conditions [14, 15]. The cross-sectional area of a leg together with the channels was $S = 1$ cm^2, contact resistance at points of legs connection was $r_0 = 5\cdot10^{-6}$ Ohm·cm^2. The calculation was done under condition of thermostating the cold junctions at temperature $T_c = 300$ K for different values of heat carrier temperature at thermoelement inlet T_m = 900 K, 1100 K, 1500 K. In so doing, the temperature of thermoelement hot junctions was software controlled not to exceed the value of 800 K, namely the limiting value of temperature dependences of *Co-Sb* based materials (Fig. 2).

As a result of calculations, the optimal values of *j, G* and doping parameter *x* were found whereby maximum efficiency of thermal into electric energy conversion is achieved. The dependences of efficiency and power on the leg height, channel diameter and the number of channels were determined.

The dependences of maximum efficiency η and specific electric power W of a permeable

generator thermoelement with the optimal values of j, G and doping parameter x of legs on the leg height l_k for different hot junction temperatures are given in Fig. 3. The data is given for channel diameter $_k$ = 0.1 cm and the number of channels N_k = 25 pcs per 1 cm^2.

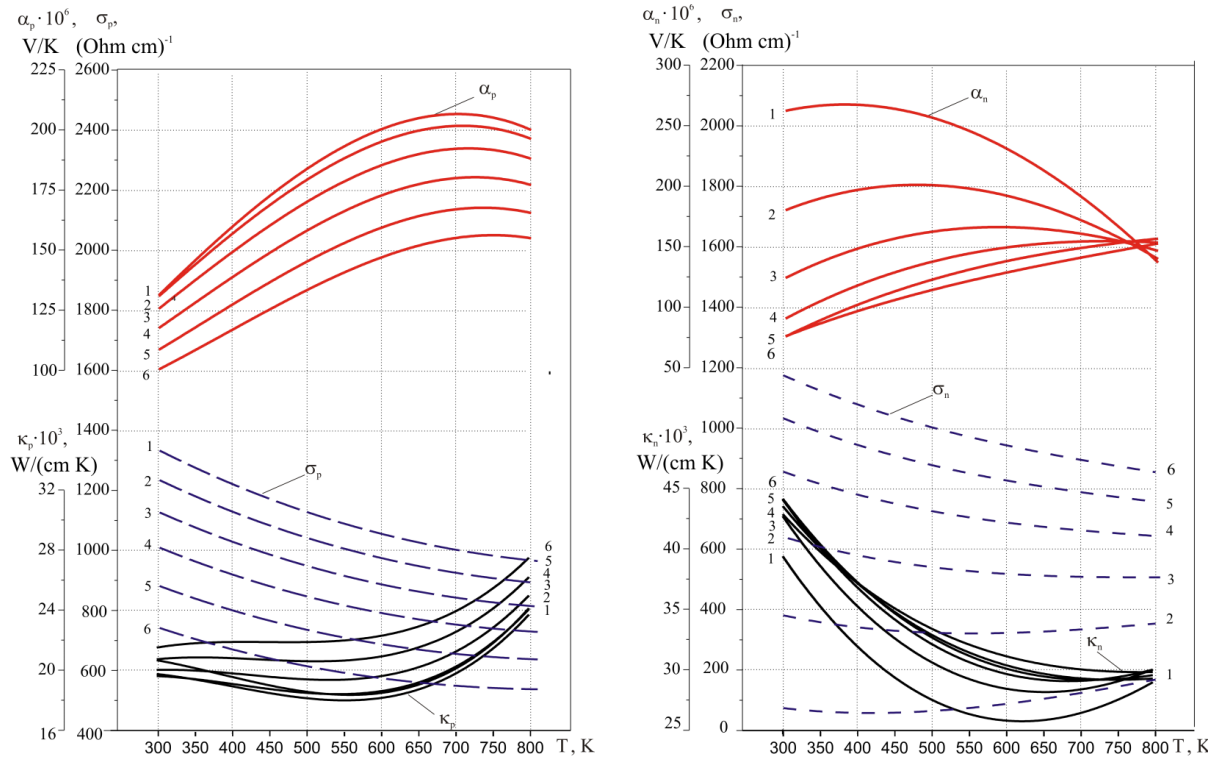

a) *b)*

Fig.2. Temperature and concentration dependences of Co-Sb based material:
a) n –type material $CoSb_{2.875-x}Ge_{0.125}Te_x$ for different values of x-components of Te impurity [12];
b) p –type material $Yb_xLa_yFe_{2.7}Co_{1.3}Sb_{12}$ for different x-components of Yb impurity (x+y = 1) [13];
(1 – x = 0.050 , 2 – 0.150, 3 – 0.250, 4 – 0.350, 5 – 0.450 , 6 – 0.550).

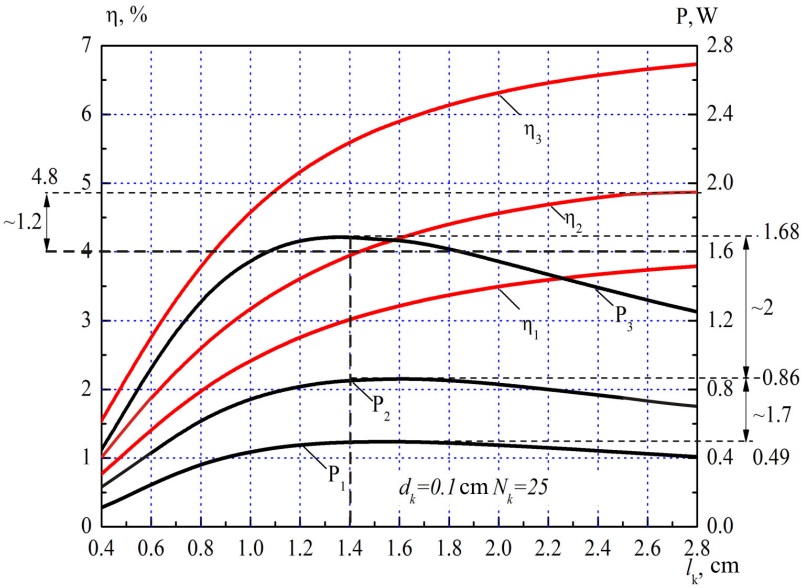

Fig. 3. Efficiency and electric power of a permeable Co-Sb based thermoelement as a function of leg length l_k.
1 – heat carrier temperature at thermoelement inlet T_m=900 K; 2 - T_m=1100 K; 3 - T_m=1500 K.

It is seen that as the leg height increases, the efficiency grows and attains saturation achieving maximum value ($\eta = 6.7$ %) for heat carrier temperature $T_m = 1500$ K. The electric power has a maximum at the leg height $l_k = 1.4$ cm which corresponds to optimal height of leg whereby maximum electric power is generated by thermoelement. In so doing, the efficiency for heat carrier temperature 1100 K is about 1.2 times that of an impermeable thermoelement η_0 working under similar conditions.

The results of research of the effect of channel diameter d_k on the efficiency and electric power of a permeable generator thermoelement under optimal conditions for different heat carrier temperatures T_m with the leg height $l_k = 1$ cm and the number of channels $N_k = 25$ pcs per 1 cm^1 are given in Fig. 4.

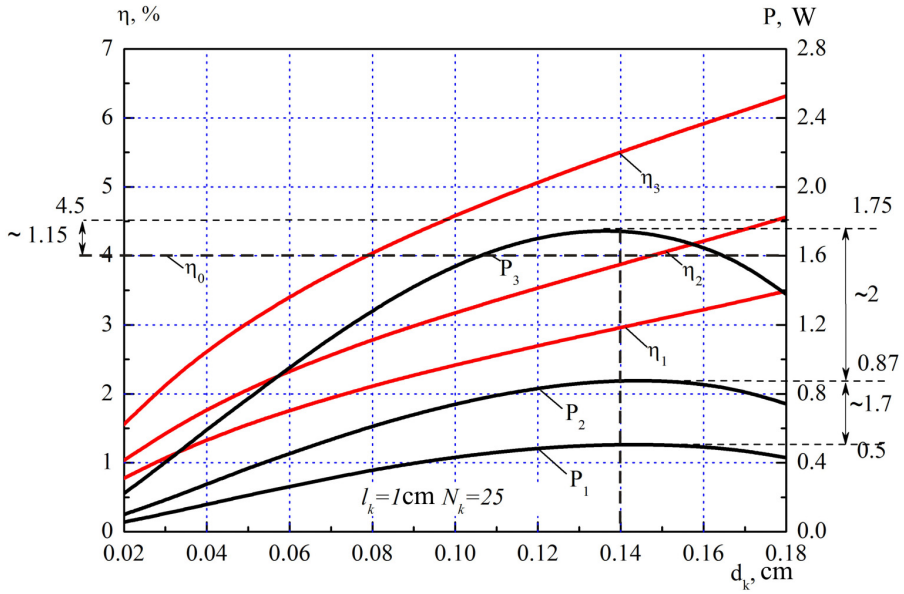

Fig. 4.Dependences of the energy characteristics of a permeable single-segmented thermoelement on channel diameter d_k: 1 – heat carrier temperature $T_m = 900$ K; 2 - $T_m = 1100$ K; 3 - $T_m = 1500$ K.

As is evident from Fig. 4, the efficiency of a permeable thermoelement increases with increase in channel diameter and has maximum values at heat carrier temperature $T_m = 1500$ K, as in the previous case. From the above dependences it is also seen that the efficiency of a permeable thermoelement can exceed that of classical thermoelement by a factor of 1.15. The electric power has an extremum with increase in channel diameter for all considered hot junction temperatures, however, it has the greatest value for heat carrier temperature 1500 K $P = 1.75$ W. This value is achieved with channel diameter $d_k = 0.14$ cm, which is optimal for obtaining maximum electric power.

Dependences of the efficiency and electric power of a permeable thermoelement on the number of channels N_k under optimal conditions of *j, G, x* for channel diameter $d_k = 0.2$ cm, leg height $l_k = 1$ cm are given in Fig. 5.From the data is follows that the efficiency increases with increasing the number of channels and reaches maximum, as in the two previous cases, at heat carrier temperature $T_m = 1500$ K and makes $\eta = 6.8$ %. There can be 1.3-fold efficiency increase as compared to a conventional thermoelement. Electric power has a maximum at $N_k \sim 16$ pcs per 1 cm^2 and makes $P = 1.57$ W.

For different operating conditions of permeable generator thermoelements of *Co-Sb* based materials it is necessary to determine their own optimal design parameters (leg height, diameter and number of channels) whereby maximum electric power will be obtained. Under optimal operating conditions the efficiency is 1.1.-1.3 times that of a conventional thermoelement.

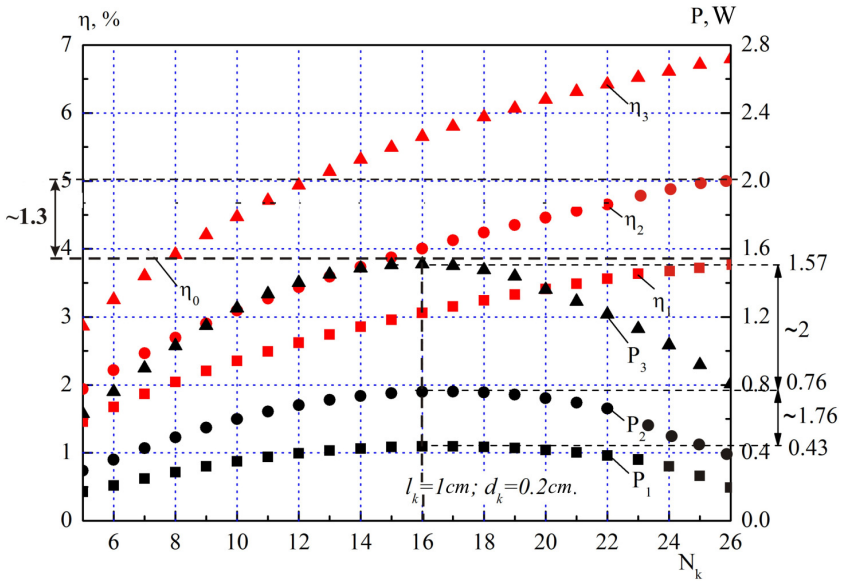

Fig. 5. Dependences of the energy characteristics of a permeable segmented thermoelement on the number of channels N_k. 1 – heat carrier temperature T_m = 900 K; 2 - T_m = 1100 K; 3 - T_m = 1500 K.

Conclusions

1. Procedure of calculation and design of permeable generator thermoelements of *Co-Sb* based materials is represented.
2. The effect of design parameters (leg height and the number of segments) under optimal efficiency operating conditions on the basic characteristics of energy conversion is determined. Optimal design parameters have been found, namely leg height l_k = 1.4 cm, channel diameter d_k = 0.14cm, the number of channels N_k ~ 16 pcs per 1 cm^2 whereby maximum electric power is obtained.
3. It is shown that the efficiency of permeable generator thermoelements of *Co-Sb* based materials can be approximately 1.1 – 1.3 times that of conventional thermoelements working under similar conditions.

References

1. L.I.Anatychuk, R.V.Kuz, and Yu.Yu.Rozver, Efficiency of Thermoelectric Recuperators of the Exhaust Gas Energy of Internal Combustion Engines, *J.Thermoelectricity* **4**, 78-83 (2011).
2. E.P.Sabo, Technology of Chalcogenide Thermoelements. Physical Foundations. Chapter 1. Structure and Properties of Materials, *J.Thermoelectricity* **3**, 30 (2000).
3. C.Uher, Skutterudite-Based Thermoelectrics. Thermoelectrics Handbook. Macro to Nano. Edited by D.M.Rowe (CRC Press, 2006), P. 34-1-34-13.
4. Jae-Yong Jung, Kwan-Ho Park, and Il-Ho Kim, Thermoelectric and Transport Properties of *In*-filled and *Ni*-doped $CoSb_3$ Skutterudites, *J. of the Korean Physical Society* **57**(4), 773-777 (2010).
5. G. A. Lamberton, S. Bhattacharya, R. T. Littleton, M. A. Kaeser, R. H. Tedstrom, T. M. Tritt, J. Yang, and G. S. Nolas, High Figure of Merit in *Eu*-Filled $CoSb_3$-Based Skutterudites, *Appl. Phys. Lett.* **80**, 598 (2002).
6. L.I.Anatychuk, R.G.Cherkez, Permeable Thermoelement in Electric Energy Generation Mode, *J.Thermoelectricity* **2**, 35-46 (2003).

7. L.I.Anatychuk, R.G.Cherkez, Permeable Segmented Thermoelement in Electric Energy Generation Mode, *J.Thermoelectricity* **3**, 5-12 (2010).
8. A.J.Zhou, T.J.Zhu, X.B.Zhao, et al., Improved Thermoelectric Performance of Higher Manganese Silicides with Ge Additions, *J. of Electronic Materials* **39**(9), 2002 (2010).
9. L.I.Anatychuk, L.M.Vikhor, *Thermoelectricity. Volume IV. Functionally-Graded Thermoelectric Materials* (Chernivtsi: Bukrek, 2012), 180 p.
10. R.G.Cherkez, M.V.Maksimuk, and P.P.Fenyak, Design of Thermoelectric Permeable Structures Based on *Mg* and *Mn* Silicides, *J.Thermoelectricity* **6**, 62-70 (2013).
11. V.R.Bilinsky-Slotylo, L.M.Vikhor, V.Ya.Mikhailovsky, R.N.Mochernuyk, and A.F.Semizorov, Efficiency Improvement of Generator Modules Based on *CoSb* through Use of Segmented and Multi-Stage Structures, *J.Thermoelectricity* **3**, 71-76 (2013).
12. X.Su, H.Li, Q.Guo, X.Tang, Q.Zhang, and C.Uher, Structure and Thermoelectric Properties of *Te*- and *Ge*-Doped Skutterudites $CoSb_{2.875-x}Ge_{0.125}Te_x$, *J. of Electronic Materials* **40**(5), 1286-1291 (2011).
13. Ch.Zhou, D.Morelli, X.Zhou, G.Wang, and C.Uher, Thermoelectric Properties of p-type *Yb*-filled Skutterudite $Yb_xFe_yCo_{4-y}Sb_{12}$, *Intermetallics* **19**(10), 1390-1393 (2011).
14. Yu.N.Lobunets, *Methods of Calculation and Design of Thermoelectric Power Converters* (Kyiv: Naukova Dumka, 1989), 176 p.
15. G.K.Kotyrlo, G.M.Schegolev, *Heat Diagrams of Thermoelectric Devices* (Kyiv:Naukova Dumka, 1973), 215p.

Submitted 27.06.2014.

Yu.M. Lobunets

Yu.M. Lobunets

Institute of Thermoelectricity, 1, Nauky Str.,
Chernivtsi, 58029, Ukraine

THERMOELECTRICITY AND OCEAN

The prospects of using thermoelectric generators for ocean thermal energy conversion are discussed. It is shown that thermoelectric method of power conversion is capable of assuring competitive technical and economic performance as compared to traditional systems of ocean thermal station (OTEC).

Key words: thermoelectric generator, ocean thermal energy.

Introduction

The global ocean covers more than 70 % of the earth surface. In fact, it is a huge natural accumulator of solar energy the absorption of which creates temperature gradient between the surface and deep water layers. In tropical latitudes this difference reaches 20 °C (Fig. 1). By the existing estimates, from the ocean surface restricted by a square of one degree of latitude and longitude, one can obtain 100 mlrd kW-hours of thermal energy per year. That is, it is almost a boundless source of thermal energy that can be converted into electric energy. However, this resource is hard to be exploited, since currently existing technologies of ocean thermal energy use have not yet reached the commercial level.

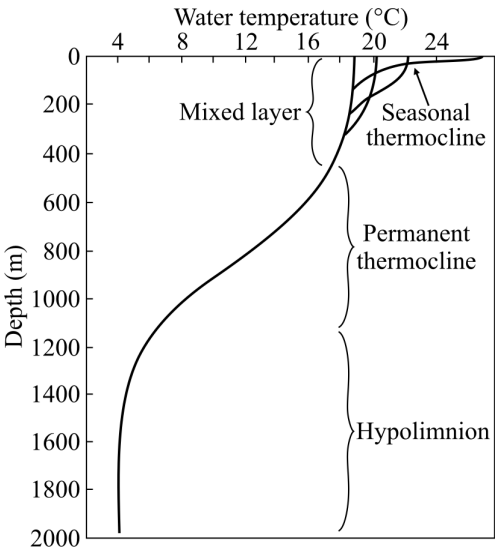

Fig. 1. Temperature distribution within the ocean column.

Starting from the 70-s of the last century, investigations have been pursued to use ocean thermal energy mostly in two directions, namely to supply energy to island consumers and for power supply to self-contained systems (navigational and oceanological buoys, etc.).

A series of implemented pilot projects [1, 2] confirm principal opportunity of achieving acceptable technical and economic performance of OTEC, but this technology does not find industrial application so far. Considerable attention to studies of this problem is paid to the Asia-Pacific region. There are 15 research centres in Japan that are equipped with systems of deep sea water delivery of volume from 500 to 13000 tons per day [3]. The largest of them, "Kumejima" project [4] stipulates creation of a sustained development model for small islands of Okinawa prefecture (Japan) which is based on the use of deep sea water for ecologically clean energy, agricultural and aquaculture technologies. The project is based on cold sea water delivery system providing for supply of 13 thousand tons per day of water with temperature 6...9 °C. This resource is used for room air conditioning systems, product cooling and in aquaculture. In June 2013, a project of 50 kW demonstrational OTEC was put into operation on the island (Fig. 2) [5].

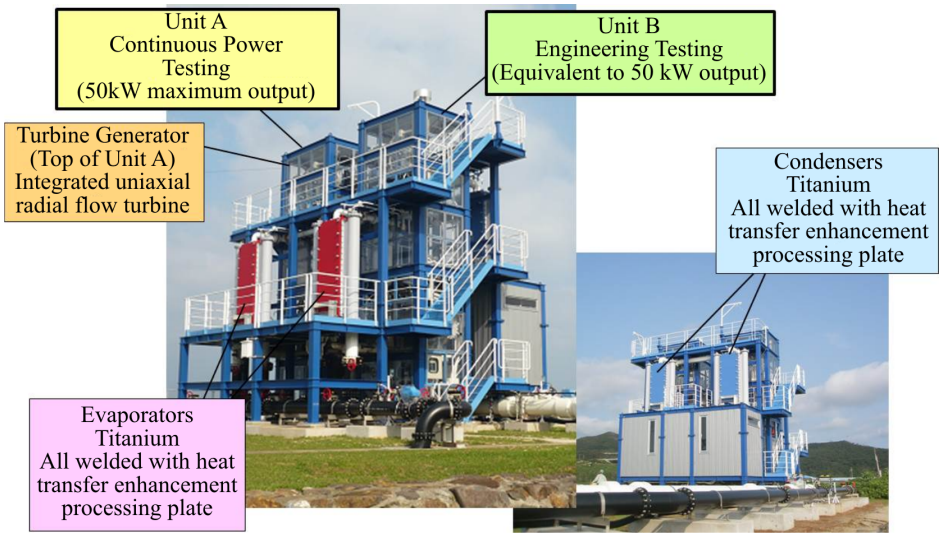

Fig. 2. 50 kW demonstrational OTEC on Kumejima Island [5].

The project was developed by Institute of Ocean Energy of Saga University and company Xenesys in cooperation with Natural Energy Laboratory of Hawaii, NELHA. In the USA, the leading company in the field of investigations on ocean energy problems is Lockheed Martin Corp., developing the project of OTEC of power 10 MW [6]. Another big centre of research on OTEC problems is Taiwan.

The prospects of using TEG for ocean thermal energy conversion

Modern OTEC projects focus on the use of steam-power cycle with a low-boiling refrigerant. The drawback of this technology is high metal consumption and essential dependence of economic figures on the scale factor, namely minimum power level that assures acceptable economic performance is 50 MW (Fig. 3).

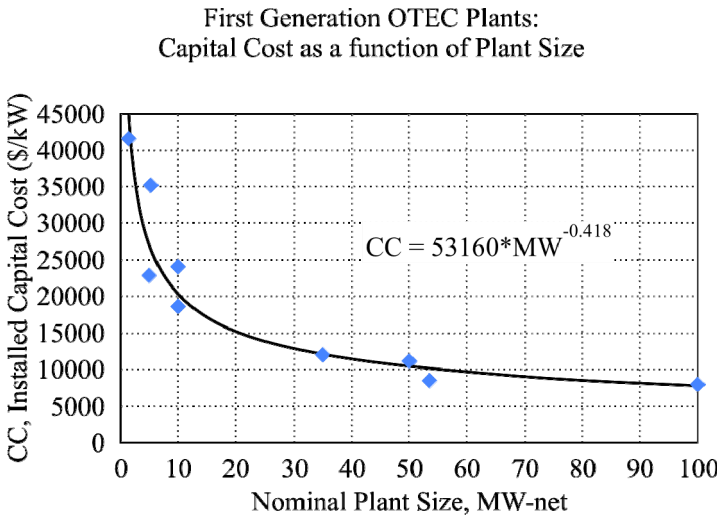

Fig. 3. Relative capital cost $US/kW versus OTEC size [1].

On evidence derived from [1], the cost of electric energy of 1 MW OTEC is 0.7 – 0.9 $US/kW-h, and for 100 MW OTEC – 0.12 $US/kW-h (Fig. 4). The latter figure can be already considered as competitive as compared to the cost of electric energy from traditional sources, but implementation of similar projects is problematic because of the necessity of big investments (on the level of

1 mlrd $US) under conditions of ill defined risks. At the same time, the experience of introduction of modern conversion systems of renewable power sources (photoelectric converters, wind generators) shows that their extensive use, despite the high cost of electric energy, became possible due to the use of low power systems (1 – 100 kW) and the use of special feed-in tariffs assuring high profitability of using similar systems. Unfortunately, for a classical OTEC system with a steam-power cycle such a way is impossible due to scale restrictions.

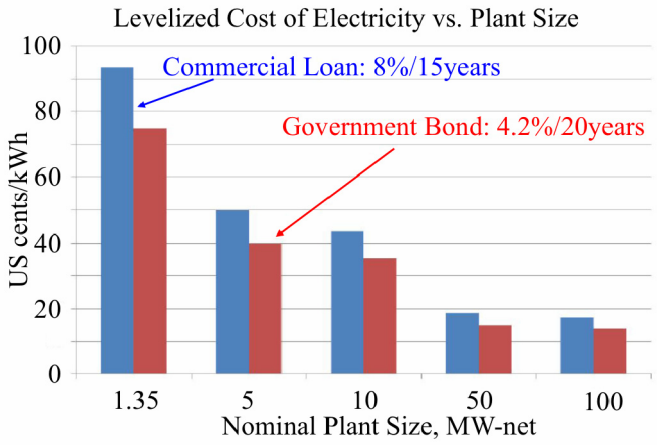

Fig. 4. The cost of electricity $US/kW-h versus OTEC size [1].

In this respect, thermoelectric method of thermal energy conversion offers certain advantages, while in the operating temperature range of OTEC the efficiency of TEG is practically the same as the efficiency of steam-power cycle (both have the efficiency 1 %). First of all, TEG are almost insensitive to scale factor, that is, economic parameters of ocean thermoelectric generator (OTEG) of 1 kW scale are practically not different from OTEG of megawatt scale which makes its possible to bring OTEG to commercial level in kilowatt power range.

An additional advantage of OTEG is a simpler design, absence of low-boiling refrigerants (as a rule, toxic), and, respectively, much higher reliability and self-sufficiency. Similar to OTEC with steam turbine generator, OTEG system includes pipelines of cold and hot water, heat exchangers, pumps, as well as thermoelectric converter and inverter. Design of a heat exchange-type TEG proposed in [7] allows combining in one unit the heat exchangers of the hot and cold heat carrier, which reduces considerably materials consumption and the dimensions of OTEC. For comparison, 50 kW OTEG will have approximately the same dimensions as condenser unit OTEC-50 (shown in the right bottom angle in Fig. 2). Estimates of electric energy cost of 100 kW power OTEG [8] confirm the possibility of reaching quite competitive level of electric energy cost (0.10 $US/kW-h), comparable to the cost of energy from conventional energy sources and unattainable for traditional OTEC schematic. This opens up the possibilities of creating 1...1000 kW OTEG for commercial use for the purpose of reliable electric energy supply to numerous independent consumers.

OTEG + “Solar pond” = OSTEG

Another schematic of using sea water potential with the help of thermoelectricity is a combination of OTEG schematic with “solar pond” schematic. Solar pond is a water reservoir 2 – 3 m deep filled with salt solution (Fig. 5). Due to the fact that solubility of salts in water is increased with a rise in temperature, situations are possible when solution stratification occurs, namely in the near-bottom layer the concentration (and density) of solution is increased, and in the near-surface layer it is

reduced [9]. Owing to this, three pronounced zones appear in the reservoir, namely upper convective zone 0.1...0.3 m thick consisting of fresh water, gradient layer where salt concentration grows with increasing the depth, and near-bottom convective zone with maximum concentration.

Gradient layer due to suppression of natural convection has high thermal resistance (about three orders higher than the thermal resistance of fresh water).

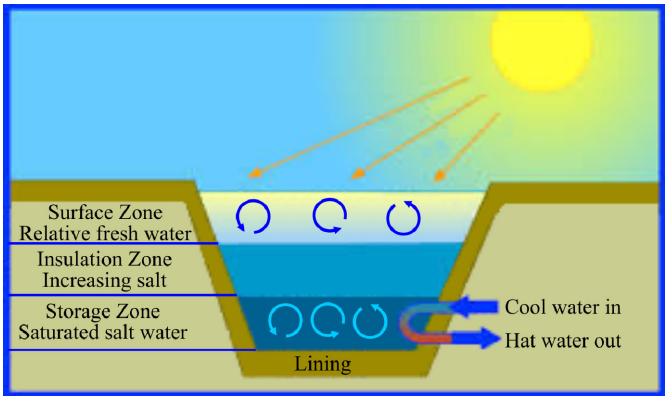

Fig. 5. "Solar pond" schematic [10].

As a result, the near-bottom layer is isolated from the surface and can accumulate the energy of solar radiation. The temperature in the near-bottom layer can reach more than 100 °C.

A combination of such thermal energy source with a powerful heat sink such as deep sea water opens up the possibilities of creation of sufficiently high-performance electric power stations. Owing to greater temperature difference, the thermoelectric generator in such a schematic has much better parameters than OTEG. The main capital expenditures account for pond construction – its cost is about 30 \$US/m^2 [11], which with regard to the necessary volume of heat accumulator yields 8...10 thousand \$US per 1 kW of rated power of OSTEG. As compared to OTEG, the cost of schematic under study is about 30 % lower. Accordingly, the cost of electric energy with round-the-clock operation is 0.1 \$US/kW-h, and in the case of using OSTEG in peak mode – 0.04 \$US/kW-h [12]. The acceptable power range for OSTEG is 10 – 100 kW. The most promising application spheres are within complexes of using deep sea water similar to "Kumejima" centre on Okinawa Island.

OTEG for self-contained systems

Modern ocean is filled with thousands of various-purpose sea buoys, namely navigational, research, military, etc. that work under water in autonomous mode. The equipment of these devices requires power supply which is generally realized by means of chemical sources whose operation time is restricted.

In due time, for similar applications we proposed a thermoelectric supply with nearly unrestricted lifetime [13]. The specific feature of this device is that it can independently migrate between horizons with warm and cold water, filling the respective capacities that serve as heat accumulators. Heat flows from the hot to cold accumulator through a thermopile that generates electric current. Migration takes place at the cost of change in equipment buoyancy which occurs due to using the temperature dependence of the solubility of gases present in sea water. Later on, the principle of migration of underwater unit between water layers with different temperature for charging heat accumulators was proposed in the works of Martin Marietta Corporation, including the use of thermoelectric generator [14, 15]. However, these proposals are meant for more powerful applications, since they are based on quite energy-intensive mechanisms of assuring migration of devices.

Conclusions

The use of thermoelectric generators in applications related to ocean subject matter holds good prospects, but their practical implementation is largely dependent on the attraction of investments to scientific research.

References

1. Luis A. Vega, Ph.D, Economics of Ocean Thermal Energy Conversion (OTEC): An Update, *2010 Offshore Technology Conference* (Houston, Texas, USA, 3 – 6 May 2010).
2. G.C. Nihous and M. A. Syed, A financing strategy for small OTEC Plants, *Energy Convers. Mgmt.* 38 (3), 201 – 211 (1997).
3. http://otecokinawa.com/en/OTEC/WaterUse.html
4. http://www.okinawab2b.jp/misc6.html
5. http://morethttpsjapanese.com/okinawa-otec-power-initialization-ceremony/
6. http://www.lockhttpmartin.com/us/products/otec.html
7. *Patent of Ukraine №83157*, Thermoelectric Generator (Yu.M.Lobunets, 27.08.2013).
8. Yu.M. Lobunets, Performance Evaluation of OTEC with Thermoelectric Power Converter, *J. Thermoelectricity* 1, 62 – 67 (2013).
9. A. Akbarzadeh, J. Andrews, Solar Ponds, http://www.eolss.net/Sample-Chapters/C08/E6-106-08.pdf
10. http://www.energyeducation.tx.gov/renewables/section_3/topics/solar_ponds/index.html
11. http://soilwater.com.au/solarponds/costs.httpPOWER
12. Yu.M. Lobunets, Solar Pond with Thermoelectric Energy Converter, *J. Thermoelectricity* 2, 95 – 98 (2013).
13. Patent RF № 2031486, Thermoelectric Generator (Yu.M. Lobunets, N.A. Grin, and TG.V. Struts, 01.04.1991).
14. Patent US 2010/039271 A1, 10.06.2010.
15. Patent US 8065972 B2, 29.11.2011.

Submitted 12.06.14

L.I. Anatychuk, R.V. Kuz

Institute of Thermoelectricity of the NAS and MES
of Ukraine, 1, Nauky Str.,
Chernivtsi, 58029, Ukraine

L.I. Anatychuk

EFFECT OF AIR COOLING ON THE EFFICIENCY OF A THERMO-ELECTRIC GENERATOR IN A CAR WITH A PETROL ENGINE

R.V. Kuz

The paper is concerned with a physical model of a thermoelectric generator (TEG) for a petrol engine with a system of heat removal from TEG, comprising an air-to-liquid heat exchanger and an electric fan. A mathematical and computer description of the model is presented. Computer simulation of the model for a 70 kW petrol engine is considered. Optimal hot side temperatures of the generator and optimal powers of the fan are found whereby maximum net power is attained and, accordingly, maximum real efficiency of TEG with regard to expenditures on the fan supply for ambient temperatures in the range of –40…+50^{O}C. A comparison of such efficiencies to those previously obtained for a diesel engine is made. It is shown that a real efficiency of TEG with a heat exchanger for a petrol engine is 1.3 – 1.5 fold higher than for a diesel engine of the same power.
Key words: heat recovery, thermoelectric generator, internal combustion engines.

Introduction

The use of waste heat from the internal combustion engines is one of most discussed subjects among practical applications of thermoelectricity. The ultimate purpose of such application is fuel saving due to the use of engine exhaust heat for electric energy generation [1, 2].

As is known, the presence of a thermoelectric generator in a car has a considerable impact on its operation. The negative factors include, for instance, additional resistance to gas motion in vehicle exhaust system, additional expenditures of engine power on the transportation of TEG proper; and the expenditures related to the necessity of heat removal from a thermoelectric generator. Some of these impacts are discussed in [3-5]. It is shown that for cars these costs can sometimes exceed the effective work of TEG.

Expenditures on heat removal from TEG for a car with a diesel engine are considered in [6]. The values of these expenditures for 75 kW engine are determined. It is established that expenditures on heat removal from a one-sectional TEG can reach 15-25% of the electric energy produced by TEG, or about 6-12% of TEG power in the form of engine's mechanical energy. In general, it is shown that for a diesel engine the use of TEG with regard to expenditures on heat removal adds 1.5-4% to engine power in the form of electric energy, which, accordingly, can give about 2-6% of fuel saving when doing away with a dynamo.

It is interesting to establish similar regularities for petrol engines, since the exhaust gas temperature in them is known to be much higher compared to diesel engines, which can give more optimistic figures of fuel saving.

The purpose of this work is to estimate the efficiency of using a thermoelectric generator for a car with a petrol engine with regard to energy spent on heat removal from TEG.

Physical model and computer design of TEG for a car

The work of a thermoelectric generator as part of a car can be represented by a schematic shown in Fig. 1.

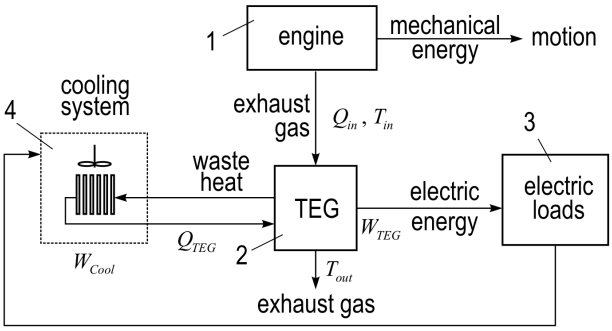

Fig. 1. A model of TEG operation in a car with regard to electric energy spent on heat removal from TEG.

Exhaust gas of thermal power Q_{in} from engine 1 comes to thermoelectric generator 2 of thermal resistance R_t at temperature T_{in} and leaves the generator at temperature T_{out}. The TEG generates electric energy W_{TEG} at efficiency η_{TEG}. A case is considered when part of this electric energy W_{cool} is spent on the operation of cooling system 4 which removes thermal power Q_{TEG} from the TEG. The ambient temperature is T_{amb}.

Computer model and design methods for this model are given in [6]. The main relations for the calculations are as follows:

$$T_{out}(R_t) = \left(Q_{in}\left(1 + \frac{T_{amb}}{T_{in} - T_{amb}}\right) + \frac{T_0}{R_t} \right) / \frac{1}{R_t} + \frac{Q_{in}}{T_{in} - T_{amb}}, \tag{1}$$

$$\eta_{TEG}(R_t) = \frac{T_{out} - T_0}{T_{out}} \frac{M - 1}{M + T_0 / T_{out}}, \tag{2}$$

where

$$M = \sqrt{1 + Z\frac{(T_{out} + T_0)}{2}}. \tag{3}$$

The effective efficiency of TEG is introduced by the expression:

$$\eta_{ef} = (W_{TEG} - W_{cool}) / Q_{in}. \tag{4}$$

These methods are not essentially different from the design methods for a diesel engine. The difference lies primarily in higher temperatures of exhaust gases (~800°C) and the use of alternative thermoelectric materials suitable for operation at elevated temperatures.

Such a model has two values that should be optimized, namely the hot side temperature of TEG and the electric power spent on the operation of cooling system.

Example of parameters calculation of TEG for a petrol engine

As an example, we shall calculate the basic parameters of TEG for a stock 70 kW petrol engine UMZ-3318 in continuous operation mode. In this operation mode, the exhaust gas temperature is about 790°C. For such a TEG, *n-PbTe* and *p*-TAGS materials that have the best figure of merit in the operating temperature range were selected. The *ZT* value of a module of such a couple is given in Fig. 2 [8].

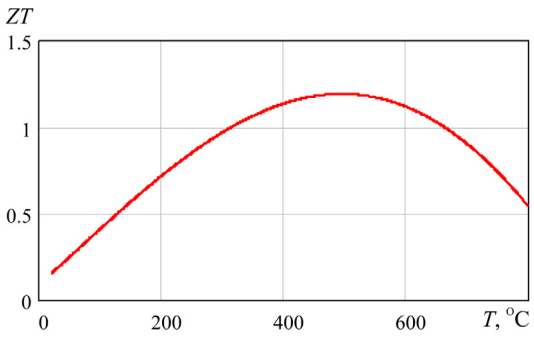

Fig. 2. Temperature dependence of ZT for n-PbTe and p-TAGS based modules.

The characteristics of air-to-liquid heat exchanger necessary for calculations were taken from [6].

TEG hot side temperature optimization. In the beginning, optimization for the efficiency of the hot side temperature of TEG took place which at constant thermal power of exhaust gases is a function of TEG thermal resistance. Fig. 3 shows the result of such optimization. It is seen that optimal temperatures change only slightly. It allows without essential efficiency loss using in thermal generator one averaged thermal resistance of thermopile. Fig. 4 gives the values of efficiency and electric power of TEG depending on the hot side temperature at different cold side temperatures of TEG. It is seen that with a reduction of cold side temperature, maximum efficiency and power is shifted towards lower temperatures, as in Fig. 3, and the efficiency value in this case is somewhat increased (Fig. 5) due to a combined effect of the thermodynamic efficiency and the temperature dependence of *ZT* of modules.

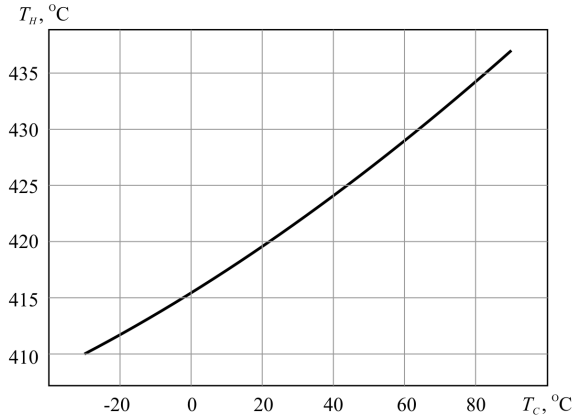

Fig. 3. Optimal hot side temperature of TEG versus its cold side temperature.

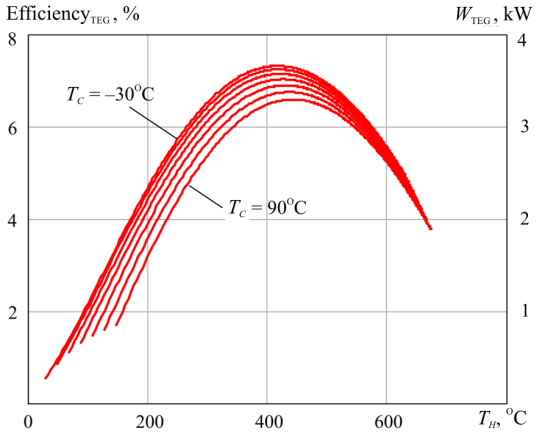

Fig. 4. Efficiency and electric power of TEG versus its hot side temperature. T_C varies from –30°C to +90°C.

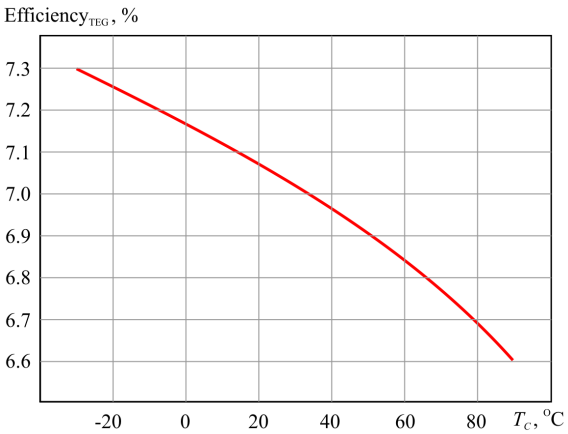

Fig. 5. TEG efficiency versus its cold side temperature.

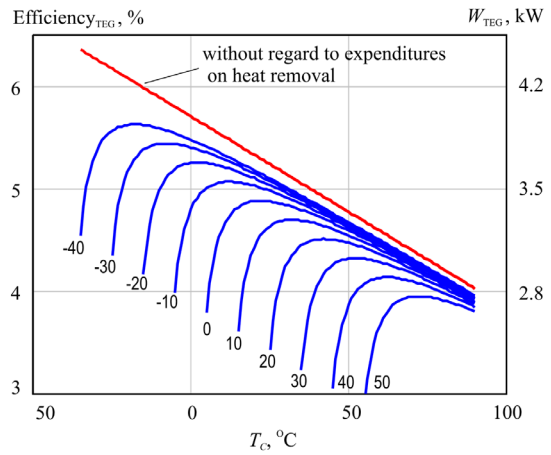

Fig. 6. Dependences of the efficiency and electric power of TEG on the cold side temperature of TEG (Ambient temperature, °C is indicated beside the plots).

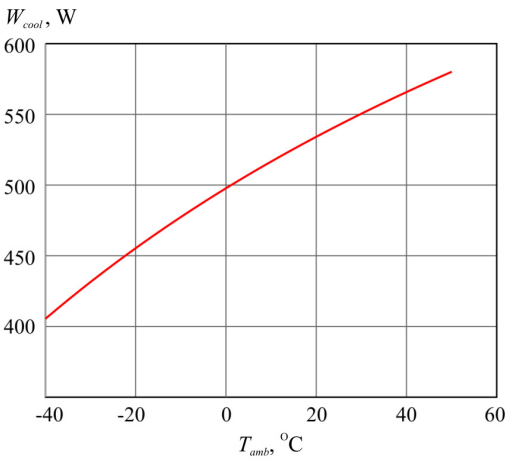

Fig. 7. Dependence of the optimal electric supply power of cooling system on the ambient temperature.

Calculations of extreme efficiency and power of TEG with regard to the fact that part of its electric energy is spent on providing the work of heat removal system were made with the aid of computer simulation according to Eqs. (1-4).

Fig. 6 shows the result of optimization of "TEG-cooling system" system for different ambient temperatures. From the plots it is seen that there exist pronounced optimal operating modes of TEG cooling system. The values of optimal powers of cooling system fan are given in Fig. 7. They make ~10%...20% of thermal generator power.

Fig. 8 gives a comparison of TEG efficiency with a heat removal system for diesel [6] and petrol engines. As is evident, the use of TEG with a petrol engine yields better parameters, namely the efficiency is less dependent on the ambient temperature. It can assure ~1.3-1.5-fold higher efficiency and electric power and, accordingly, fuel saving about 4 – 6.5%.

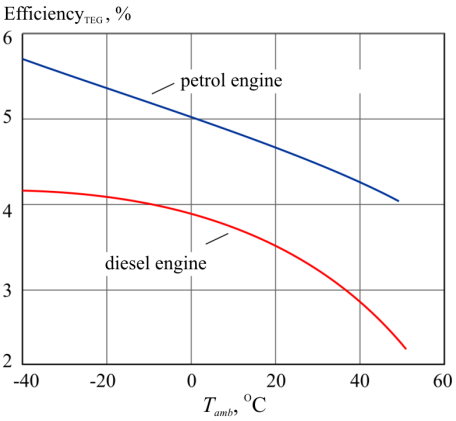

Fig. 8. Dependence of TEG efficiency on the ambient temperature.

Conclusions

1. Computer simulation has been used to establish essential dependence of the efficiency of using TEG in a car with a petrol engine on the electric power spent on heat removal from the thermal generator.

2. It has been also established that the extreme values of efficiency and power are attained with TEG optimization for hot side temperature and for the electric power spent on fan supply in a system of heat removal from the thermal generator.

3. Computer simulation of TEG with a system of heat removal for a 70 kW petrol engine, the ambient temperatures –40…+50^{O}C and the use in TEG thermopiles of materials based on *PbTe* and TAGS have yielded the following results: optimal hot side temperatures of the generator 410-435^{O}C; the generator efficiency with regard to expenditures on heat removal 4-6.5%; the electric power 2.8-4.5 kW; expenditures on heat removal 400-550 W; improvement of the efficiency and power of generator for a petrol engine as compared to a diesel engine by a factor of 1.3-1.5; the expected fuel saving 4-6.5%.

References

1. L.I.Anatychuk, R.V.Kuz, and Yu.Yu.Rozver, Efficiency of Thermoelectric Recuperators of the Exhaust Heat from Internal Combustion Engines, *J.Thermoelectricity* **4**, 80-85 (2011).
2. L.I.Anatychuk, R.V.Kuz, and Yu.Yu.Rozver, Thermoelectric Generator for a Petrol Engine, *J.Thermoelectricity* **2,** 97-104 (2012).
3. G.Min, D.M.Rowe, Conversion Efficiency of Thermoelectric Combustion Systems, *IEEE Transactions on Energy Conversion* **2**, 528-534 (2007).
4. K.M.Sacr, M.K.Mansour, and M.N.Mussa, Thermal Design of Automobile Exhaust Based on Thermoelectric Generators: Objectives and Challenges, *J.Thermoelectricity* **1**, 64-73 (2008).
5. X.Zhang, K.T.Chau, and C.C.Chan, Overview of Thermoelectric Generation for Hybrid Vehicles, *J. Asian Electric Vehicles* **6**(2), 1119-1124 (2008).
6. L.I.Anatychuk, R.V.Kuz, Effect of Air Cooling on the Efficiency of Thermoelectric Generator in a Diesel-Engined Car, *J.Thermoelectricity* **2**, 61-69 (2014).
7. PTC Mathcad – Engineering Calculations Software. www.ptc.com.
8. L.I.Anatychuk, R.V.Kuz, Materials for Vehicular Thermoelectric Generators, *Proc. of ICT-2011* (Michigan, USA).

Submitted 15.06.2014

L.I. Anatychuk[2], Jenn-Dong Hwang [1], M.V. Havrylyuk[2], V.V. Lysko[2], A.V. Prybyla[2]

[1]Industrial Technology Research Institute,
Bldg.77, Chung Hsing Rd., Chutung, Hsinchu, Taiwan;
[2]Institute of Thermoelectricity of the NAS and MES of Ukraine, 1, Nauky Str.,
Chernivtsi, 58029, Ukraine

REMOTE DEVICE FOR MEASUREMENT OF HEAT FLUX AND SURFACE TEMPERATURE OF CEMENT KILNS

The paper deals with a development of physical and mathematical models of a remote thermoelectric device for measurement of heat flux and temperature with regard to specific features of heat exchange from the surface of cement kilns. The results of calculation of convective and radiant heat flux components with consideration of kiln rotation are presented. Such a remote measuring device has been designed and manufactured, as well as its experimental calibration has been made.
Key words: cement kiln, measuring device, thermoelectricity.

Introduction

General characterization of the problem. The specific feature of cement production process is high consumption of thermal and electrical energy [1]. Works [2-4] are concerned with the possibility of reducing energy expenditures for cement production through use of thermoelectric recuperators of waste heat from cement kilns. For creation of such recuperators it is vital to have information on the amount of thermal energy radiated by cement kiln surface, as well as on its temperature.

Moreover, in the process of production one must assure for certain time the necessary temperatures in cement passage zones. In so doing, it is important to control temperature conditions in these zones, as well as to measure heat losses from the kiln surface (Fig. 1) [1, 5].

Fig. 1. Outward appearance of a cement kiln [6].

There are devices for monitoring the amount of heat release from the surface of kilns [1, 5]. However, they do not assure sufficient precision of temperature and heat flux measurement [7, 8].

The purpose of this work is development of a device for precise contactless measurement of heat flux and surface temperature of cement kilns.

Physical and mathematical models of measuring device

Fig. 2 shows a physical model of a thermoelectric device for remote measurement of temperature and heat flux from the surface of cement kiln 1 of length c and radius a. Heat flux Q_0 from the surface of cement kiln with temperature T_0 and emissivity factor ε_1 is transferred to the environment with temperature T_a. At the distance b from the cement kiln there is a thermoelectric measuring device. Part of heat flux Q_1 from the cement kiln comes to a graphite receiving pad 2 of the device with emissivity factor ε_2. Heat flux passes through the receiving pad with surface temperature T_1 and through thermoelectric module 3 (T_2 is the hot side temperature of thermoelectric module; T_3 is the cold side temperature of thermoelectric module). The module converts thermal energy into electric energy W. The receiving pad and thermoelectric module are placed in thermally isolated package 4. Heat losses through isolation are Q_3. Removal of heat Q_2 from the thermoelectric module is done by liquid heat exchanger (T_4, T_5 are liquid temperatures at the inlet to and outlet of heat exchanger, respectively).

The rate of heat flux from the lateral surface of the cement kiln can be written as:

$$Q = Q_{rad} + Q_{conv}, \tag{1}$$

where Q_{rad} is radiation component of heat flux, Q_{conv} is convective component of heat flux.

According to the Stephan-Boltzmann law, a radiant heat exchange between two arbitrary grey surfaces is determined by the formula:

$$Q_{rad} = \sigma \cdot \varepsilon_1 \cdot \varepsilon_2 \cdot (T_0^4 - T_1^4) \cdot S_1 \cdot \varphi_{1-2} = \sigma \cdot \varepsilon_1 \cdot \varepsilon_2 \cdot (T_0^4 - T_1^4) \cdot S_2 \cdot \varphi_{2-1}, \tag{2}$$

where σ is the Stephan-Boltzmann constant, S_1 is the radiation surface area, S_2 is the receiving pad area, φ_{1-2}, φ_{2-1} are angular radiation coefficients.

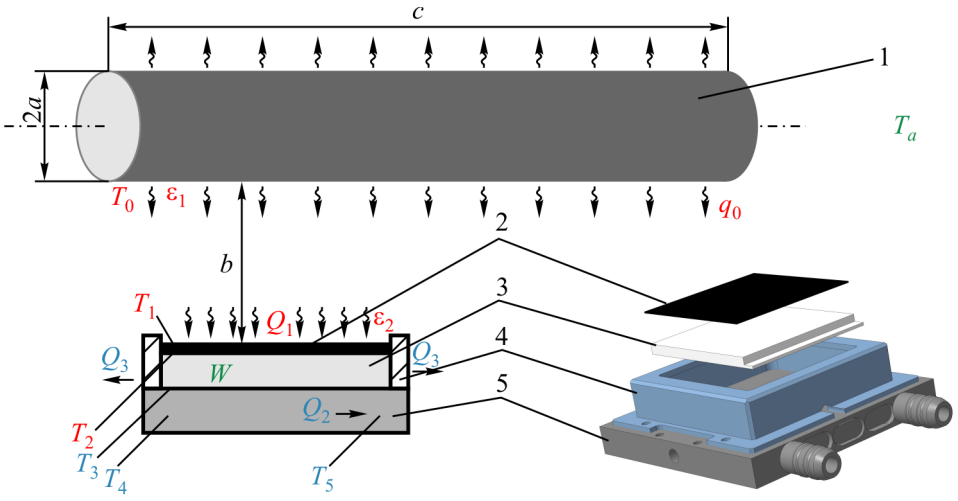

Fig. 2. A physical model of thermoelectric measuring device: 1 – cement kiln, 2 – graphite coating of receiving pad, 3 – thermoelectric module, 4 – package, 5 – liquid heat exchanger.

To determine component of heat flux that is passed to the receiving pad of the measuring device from the surface of cement kiln by radiation, it is necessary to calculate the angular radiation coefficients using the following expressions:

$$\varphi_{1-2} = \frac{1}{S_1} \cdot \iint\limits_{S_1 S_2} \frac{\cos\alpha_1 \cdot \cos\alpha_2}{\pi \cdot r^2} dS_1 dS_2, \tag{3}$$

$$\varphi_{2-1} = \frac{1}{S_2} \cdot \iint\limits_{S_1 S_2} \frac{\cos\alpha_1 \cdot \cos\alpha_2}{\pi \cdot r^2} dS_1 dS_2 = \frac{S_1}{S_2} \varphi_{1-2}, \tag{4}$$

where α_1, α_2 are the angles between the radiation direction and the normal to surfaces S_1 and S_2, respectively, r is the distance between the two surfaces.

For the case of a radiant heat exchange between the cylinder surface and the flat pad the following equation is valid:

$$\varphi_{2-1} = \frac{2}{\pi \cdot B} \cdot \left\{ \operatorname{ctg} \frac{C}{\sqrt{B^2 - 1}} + C \cdot \left[\frac{X^2 - 2 \cdot B}{X \cdot Y} \cdot \operatorname{ctg} \frac{X}{Y} \sqrt{\frac{B-1}{B+1}} - \operatorname{ctg} \sqrt{\frac{B-1}{B+1}} \right] \right\}, \tag{5}$$

where $B = \frac{b}{a}$, $C = \frac{c}{a}$, $X = \sqrt{(1+B^2)^2 + C^2}$, $Y = \sqrt{(1-B^2)^2 + C^2}$, c is the length of cement kiln 1, a is its radius, b is the distance from the kiln surface to the receiving pad.

Thus, total heat flux from cement kiln surface to a rectangular receiving pad of thermoelectric measuring device is determined by the expression:

$$Q = \sigma \cdot \varepsilon_1 \cdot \varepsilon_2 \cdot (T_0^4 - T_1^4) \cdot S_2 \cdot \frac{2}{\pi \cdot B} \cdot \left\{ \operatorname{ctg} \frac{C}{\sqrt{B^2 - 1}} + C \cdot \left[\frac{X^2 - 2 \cdot B}{X \cdot Y} \cdot \operatorname{ctg} \frac{X}{Y} \sqrt{\frac{B-1}{B+1}} - \operatorname{ctg} \sqrt{\frac{B-1}{B+1}} \right] \right\}. \tag{6}$$

For the calculation of a convective component of heat flux from cement kiln surface [4] it is necessary to determine the Nusselt criterion which in free convection is a function of the Prandtl and Grashof criteria and depends on the body shape parameter.

$$\frac{\alpha l}{\kappa} = f\left(\mathrm{Pr};\ \mathrm{Gr};\ \text{body shape}\right), \tag{7}$$

$$\frac{\nu}{a} = Pr, \quad \frac{g l^3}{\nu^2} \beta \Delta t = Gr \tag{8}$$

here β is coefficient of volume expansion of the medium; Δt is thermal head.

Thermal resistance in gases is determined by the resistance of a narrow near-surface gas layer where molecular friction prevails. Therefore, a system of motion equations will comprise only four independent variables instead of five (a, $g\rho\beta\Delta t$, μ, l). This yields only one governing criterion:

$$Pr\ Gr = \frac{g l^3}{a\nu} \beta \Delta t. \tag{9}$$

Formulae for the calculation of heat exchange coefficient in this case are as below:

a) at $10^{-3} < Pr\ Gr < 5 \cdot 10^2$

$$\alpha = A_1 \left(\frac{\Delta t}{2a^5} \right)^{1/3}, \tag{10}$$

b) at $5 \cdot 10^2 < Pr\ Gr < 2 \cdot 10^7$

$$\alpha = A_2\left(\frac{\Delta t}{2a}\right)^{1/4}, \tag{11}$$

c) at $Pr\,Gr > 2\cdot10^7$

$$\alpha = A_3\Delta t^{1/3}. \tag{12}$$

For the air at the average temperature $T_{av} = \frac{1}{2}(T_1 + T_0)$ the values of coefficients $A_{1–3}$ are as follows: $A_1 = 0.28$, $A_2 = 1.07$, $A_3 = 1.05$.

Thus, $Pr\,Gr = 1.3\cdot10^{12}$, and, accordingly, $\alpha = 6.8$ W/(m^2·K).

However, in the above variant of heat exchange due to free convection the cement kiln rotation, that is the presence of forced convective heat exchange, is disregarded. The effect of forced convection may prove to be essential. In the Couette-Taylor problems, such a rotation is taken into account through dimensionless parameters, namely the Reynolds number Reh, characterizing forced flow, or the Taylor number. Here, for the calculations a modified Taylor number is used as below

$$Ta_m = \frac{\Omega^2 d^2 \delta^3}{2\nu(d+\delta)}\left(\frac{1697}{\pi^4}C\right), \tag{13}$$

where Ω is angular velocity of rotation,

$$C = 0.0571\left(1 - 0.652\frac{2\delta}{d}\right) + 0.00056\left(1 - 0.652\frac{2\delta}{d}\right)^{-1}. \tag{14}$$

Prior to origination of secondary flows ($Ta_m < 1700$), the Nusselt number Nu^* is defined by equality

$$Nu^* = 2 \tag{15}$$

and does not depend on the properties of gas, the dimensions and rotation rate of the cylinder.

In the origination of macroeddy secondary flows, one must take into account the Taylor number. In the range $Ta_m \approx 1700\ldots10^5$ the coefficient of heat exchange for the air is defined by the empirical formula

$$Nu^* = 0.128Ta_m^{0.367}; \tag{16}$$

in the range $Ta_m \approx 10^4\ldots2\cdot10^8$

$$Nu^* = 0.42Ta_m^{0.25}Pr^{0.25}; \tag{17}$$

in the range $Ta_m \approx 10^7\ldots2\cdot10^9$

$$Nu^* = 0.28Ta_m^{0.285}. \tag{18}$$

Thus, account of kiln rotation yields increase in coefficient of heat exchange due to convection by a factor of 2.2.

Moreover, to perform precise measurements, it is also important to take into account the convective component of the heat flux that comes to the receiving surface of the measuring device Q'_{conv}. It can be taken into account by the formulae for solid wall thermal conductivity by introducing the equivalent thermal conductivity coefficient of the air gap.

The equivalent thermal conductivity coefficient of the air gap, with neglect of heat transfer due to radiation from one wall to another, is defined by the formula

$$\kappa_{eq} = \varepsilon_{conv}\kappa, \tag{19}$$

where κ is thermal conductivity coefficient of the medium filling the gap, with the average temperature of the latter (0.0355 W/(m·K) for the air at temperature 150 °C), $\varepsilon_{conv} = f\ (Pr\ Gr)$ is coefficient taking into account the effect of conversion.

The evaluation formulae for the determination of coefficient of convection:

a) at $10^4 < Pr\ Gr \left(\frac{L_1}{L_2}\right)^k \left(\frac{d}{\delta}\right)^n < 10^7$

$$\varepsilon_{conv} = 0.062\left[Pr\ Gr \left(\frac{L_1}{L_2}\right)^k \left(\frac{d}{\delta}\right)^n\right]^{1/3}; \tag{20}$$

b) at $10^7 < Pr\ Gr \left(\frac{L_1}{L_2}\right)^k \left(\frac{d}{\delta}\right)^n < 10^{10}$

$$\varepsilon_{conv} = 0.22\left[Pr\ Gr \left(\frac{L_1}{L_2}\right)^k \left(\frac{d}{\delta}\right)^n\right]^{1/4}, \tag{21}$$

where δ is layer thickness, L_1/L_2 is the ratio between the length of convective flux path from the lower heater surface to the cooler and the height of this path, d is the diameter of the heater. For an inclined cylinder layer $L_1/L_2 = 1$, $k = 3$, $n = 0$. For a horizontal cylinder layer $\frac{L_1}{L_2} = \frac{\pi r + \delta}{d + \delta}$, $k = 3$, $n = 0$.

With the value of $Pr\ Gr \left(\frac{L_1}{L_2}\right)^k \left(\frac{d}{\delta}\right)^n$ complex $< 10^3$, the effect of convection in the gap is practically absent, so in the calculation of heat exchange only thermal conductivity component is taken into account.

In the calculation of criteria, the value of average temperature $T_{av} = \frac{1}{2}(T_1 + T_0)$ is used. For this case the value of $Pr\ Gr \left(\frac{L_1}{L_2}\right)^k \left(\frac{d}{\delta}\right)^n = 7.6 \cdot 10^5$, and $\varepsilon_{conv} = 2.62$. Accordingly, $\kappa_{eq} = 0.093$ W/(m·K), and heat flux due to convection from the lateral surface of the kiln to the receiving surface of the measuring device will depend on the steady-state temperature T_1.

Description of measuring device design

Outward appearance of thermoelectric measuring device is shown in Fig. 3.

Measuring head 1 with a thermoelectric device for temperature and heat flux measurement is arranged on the telescopic mast 2 which allows control of measuring head elevation. The telescopic mast 2 is fixed to the package of control and measuring unit 5 with a collet clamp 3. Removable supports 6 assure steady state position of the measuring device.

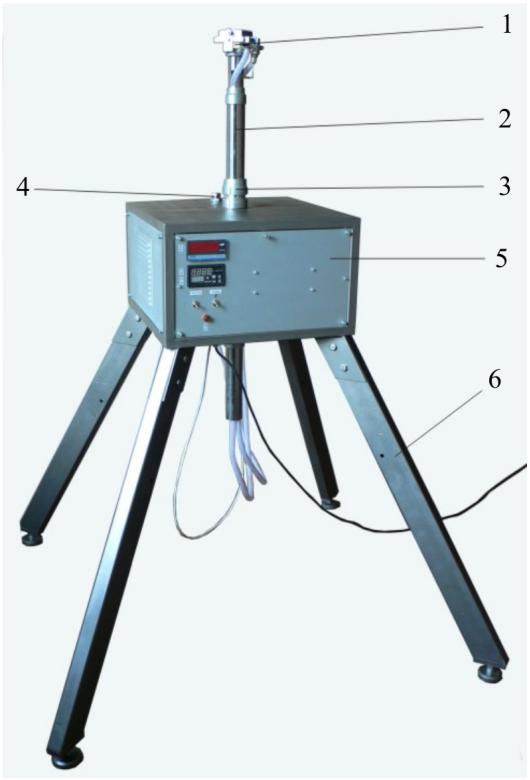

Fig. 3. Outward appearance of the measuring device: 1 –measuring head, 2 – telescopic mast, 3 – mast collet clamp, 4 – filler neck of expansion tank, 5 – control and measurement unit, 6 – supports.

Heat flux measuring device consists of a heat meter located on the heat exchanger for rejection of heat. Temperature sensor is fixed on the heat exchanger close to the heat meter's passive side. The heat exchanger is connected to liquid heat rejection circuit by liquid heat carrier. Distilled water can be used as cooling liquid. The temperature of liquid in cooling circuit is maintained by a two-channel temperature controller, where one channel maintains constant heat carrier temperature in the heat meter circuit, and the other channel is used to measure the temperature of passive heat meter side. Miniature resistance thermometers with a nominal static characteristic 100 Pt serve as temperature sensors. Heat meter signal is measured by a digital voltmeter. Heat meter together with temperature sensor and heat exchanger form a measuring head.

Fig. 4. Outward appearance of the measuring head.

The outward appearance of the measuring head is shown in Fig. 4. Liquid cooling circuit comprises also an expansion tank with water reserve about 4 l, allowing reduction of temperature fluctuations in operation of temperature control. As circuit coolers, 10 thermoelectric modules are used that work in maximum cooling capacity mode. Heat from the modules is rejected by means of heat exchangers with forced air cooling by two fans. The thermoelectric modules are powered by pulse current.

Control and measurement unit is shown in Fig. 5.

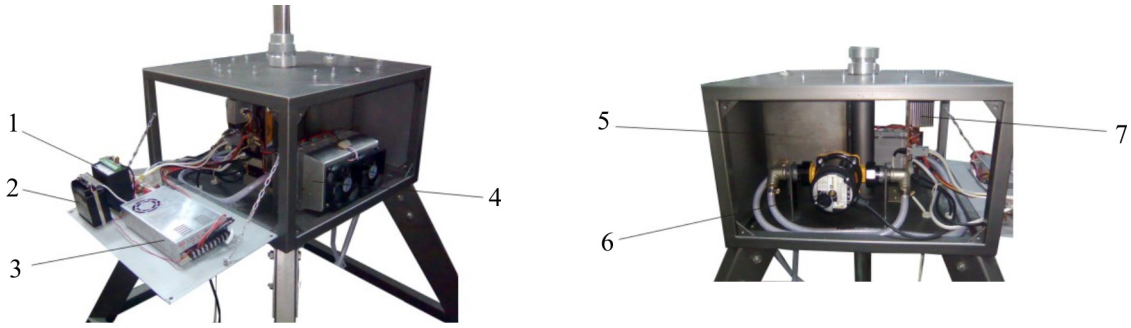

Fig. 5. Arrangement of component parts inside control unit. 1 – digital voltmeter, 2 – thermal controller, 3 – supply unit, 4 –thermoelectric water cooler in cooling circuit, 5 – expansion tank, 6 – circulating pump, 7 – power switch of thermal control system.

The power of radiation heat and the temperature of object under study are determined by the results of measuring the thermopower of thermoelectric module and its hot side temperature. The module is preliminarily calibrated. For this purpose, the emissivity factor of receiving pad is determined by experiment, and thermal flux radiated by the object and the object temperature are calculated using Eqs. (22), (24).

Calibration of a device for measuring the temperature and heat flux from the heated surface

For calibration of temperature and heat flux measuring device a special bench is used with a heater whose thermal radiation is similar to radiation from the heated cement kiln. The experimentally obtained volt-watt and volt-degree characteristics of thermoelectric meter are shown in Figs. 6, 7.

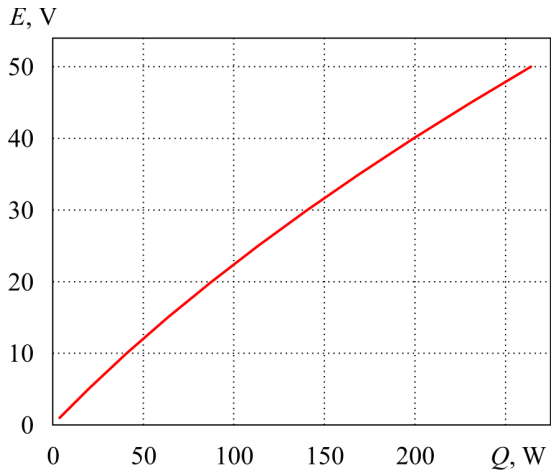

Fig. 6. Volt-watt characteristic of measuring device.

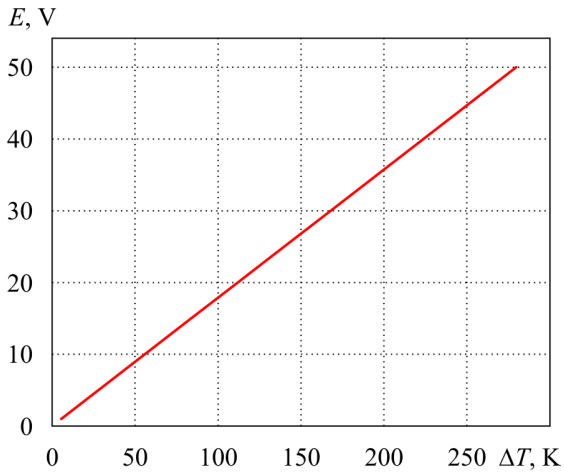

Fig. 7. Volt-degree characteristic of thermoelectric converter.

Experimental volt-watt characteristic of measuring device is described by a polynomial of the kind:

$$Q = A_1 \cdot E + A_2 \cdot E^2, \tag{22}$$

where Q is thermal flux [W], E is thermopower [V], $A_1 = 3.788$ [W/V], $A_2 = 0.03$ [W/V^2].

The temperature of heat meter's receiving pad (in Kelvin degrees) is determined as

$$T_1 = 273.15 + t_{heater} + \Delta T, \tag{23}$$

where t_{heater} are readings of thermal controller channel 1 in degrees Celsius, ΔT is temperature difference

on thermoelectric converter.

Using volt-degree calibration of thermoelectric converter, temperature difference in the heat meter is determined as:

$$\Delta T = A_3 \cdot E_{heater}, \tag{24}$$

where E_{heater} are voltmeter readings [V], $A_3 = 5.59446$ [K/V].

Based on (1) – (4), we obtain the object temperature:

$$T_0 = \sqrt[4]{\frac{A_1 \cdot E_{heater} + A_2 \cdot E_{heater}^2}{\sigma \cdot \varepsilon_1 \cdot \varepsilon_2 \cdot S} + (273.15 + t_{heater} + A_3 \cdot E_{heater})^4}. \tag{25}$$

If the exact value of coefficient ε_1 s unknown, the object temperature can be determined more precisely by performing calibration. For this purpose it is necessary to determine the value of object temperature by an external device and compare heat meter signal to this value. In this way one can determine the generalized constants. In this case:

$$T_0 = \sqrt[4]{k \cdot E_{heater} \cdot (E_{heater} + A_1 / A_2) + (273.15 + t_{htater} + A_3 \cdot E_{heater})^4}. \tag{26}$$

At $T_0 = T$ we obtain the value for k – a generalized coefficient of heat exchange

$$k = \frac{T^4 - (273.15 + t_{heater} + A_3 \cdot E_{heater})^4}{E_{heater} \cdot (E_{heater} + A_1 / A_2)} = \text{const}, \tag{27}$$

where T is an actual value of absolute object temperature measured independently.

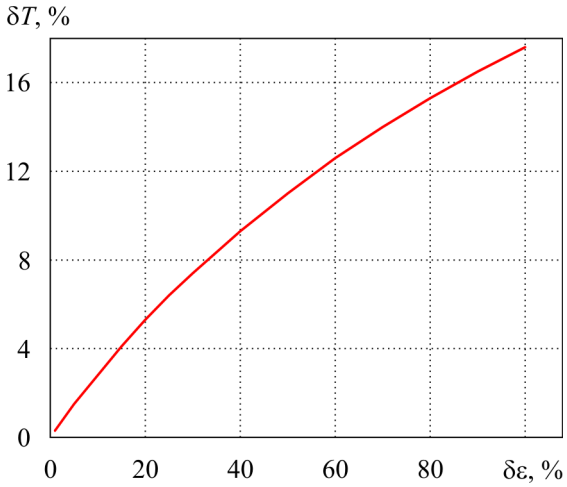

Fig. 8. Dependence of the error in measuring object temperature δT *on the error in determination of emissivity factor* $\delta\varepsilon$.

Moreover, estimates have been made of the impact of error in determination of measured surface emissivity factor on the accuracy of its temperature measurement. It has been established that a relative error in temperature measurement depends to a small extent on the accuracy of determination of surface emissivity factor (Fig. 8). Thus, to assure temperature measurement accuracy 10 %, it is sufficient to know surface emissivity factor to an accuracy of 44 %.

Conclusions

1. Physical and mathematical models of thermoelectric device for remote measurement of heat flux and temperature for cement kilns have been developed.

2. The impact of convective and radiant components of heat flux for a rotating cement kiln has been calculated. It has been established that the contribution of convective component of the flux does not exceed 30 % of its total value.
3. A thermoelectric device for remote measurement of heat flux and temperature of cement kiln surface has been designed and manufactured.
4. The volt-watt and volt-degree calibrations of such thermoelectric measuring device have been experimentally obtained.
5. Calculations of the error in object temperature measurement versus the error in determination of its emissivity factor have been performed. It is established that to provide temperature measurement accuracy 10 %, it is sufficient to know surface emissivity factor to an accuracy of 44 %.

References

1. M. Bolliger, E. Gallestey, G. Crosley, and M. Kiener, Energy management in cement manufacturing, *The Corporate Technical Journal of the ABB Group* 2, (2007).
2. L.I. Anatychuk, Rational Areas of Research and Applications of Thermoelectricity, *J. Thermoelectricity* **1**, 3 – 14 (2001).
3. L.I. Anatychuk, Current Status and Some Prospects of Thermoelectricity, *J. Thermoelectricity* **2**, 7 – 20 (2007).
4. L.I. Anatychuk, Jenn-Dong Hwang, V.V. Lysko, and A.V. Prybyla, Thermoelectric Heat Recuperators for Cement Kilns, *J. Thermoelectricity* **5**, 36 – 42 (2013).
5. G.V. Gusev, *System of Noncontact Temperature Measurements of Rotary Kilns and Estimation of Kiln Band Migration*, http://www.tekkno.ru.
6. http://ayan-tula.ru/page/public_art1.html.
7. L.I. Anatychuk, A.V. Prybyla, The Effect of Heat Exchange Systems on the Efficiency of Thermoelectric Devices, *J. Thermoelectricity* **3**, C. 39 – 43 (2012).
8. L.I. Anatychuk, A.V. Prybyla, The Effect of Heat Exchange System on Thermoelectric Generator Efficiency, *J. Thermoelectricity* **4**, 80 – 85 (2012).

Submitted 24.06.14

ARTICLE PREPARATION RULES

The article shall conform to the journal profile. The article content shall be legible, concise and have no repetitions.

The article shall be submitted to the editorial board in electronic version.

The text shall be typed in text editor not lower than MS Word 6.0/7.0.

Page setup: "mirror margins"- top margin – 2.5 cm, bottom margin – 2.0 cm, inside – 2.0 cm, outside– 3.0 cm, from the edge to page header – 1.27 cm, page footer – 1.27 cm.

Graphic materials, pictures shall be submitted in color or, as an exception, black and white, in .opj or .cdr formats, .jpg or .tif formats being also permissible. According to author's choice, the tables and partially the text can be also in color.

The article shall be submitted in English on A4 paper sheets; the number of pages shall not exceed 12. By agreement with the editorial board, the number of pages can be increased.

To accelerate publication of the article, please adhere to the following rules:

- the authors' initials and names are arranged in the centre of the first page at the distance of 1 cm from the page header, font Times New Roman, size 12 pt, line spacing 1.2;
- the name of organization, address (street, city, postal code, country) – indent 1 cm below the authors' initials and names, font Times New Roman, size 11 pt, line spacing 1.2, center alignment;
- the title of the article is arranged 1 cm below the name of organization, in capital letters, semi-bold, font New Roman, size 12 pt, line spacing 1.2, center alignment. The title of the article shall be concrete and possibly concise;
- the abstract is arranged 1 cm below the title of the article, font Times New Roman, size 10 pt, in italics, line spacing 1.2 ,center alignment;
- key words are arranged below the abstract, font Times New Roman, size 10 pt, line spacing 1.2, justified alignment. The title "Key words" – font Times New Roman, size 10 pt, semi-bold;
- the main text of the article is arranged 1 cm below the abstract, indent 1 cm, font Times New Roman. size 11 pt, line spacing 1.2, justified alignment;
- formulae are typed in formula editor, fonts Symbol, Times New Roman. Font size is "normal" – 12 pt, "large index" – 7 pt, "small index" – 5 pt, "large symbol" – 18 pt, "small symbol" – 12 pt). The formula is arranged in the text, centre aligned and shall not occupy more than 5/6 of the line width, formulae are numbered in round brackets right;
- dimensions of all quantities used in the article are represented in the International System of Units (SI) with the explication of the symbols employed;
- figures are arranged in the text. The figures and pictures shall be clear and contrast; the plot axes – parallel to sheet edges, thus eliminating possible displacement of angles in scaling;
- tables are arranged in the text. The width of the table shall be 1 cm less than the line width. Above the table its ordinary number is indicated, right alignment. Continuous table numbering throughout the text. The title of the table is arranged below its number, center alignment;
- references should appear at the end of the manuscript. References within the text should be enclosed in square brackets. References should be numbered in order of first appearance in the text. Examples of various reference types are given below.

– L.I. Anatychuk, *Thermoelements and Thermoelectric Devices: Handbook* (Kyiv: Naukova Dumka, 1979), p.766. (Book)
– T.M. Tritt, Thermoelectric Phenomena, Materials, and Applications, *Annual Review of Materials Research* **41**, 433 (2011). (Journal paper)
– U. Ghoshal, *Proceedings of the XXI International Conference on Thermoelectrics* (N.Y., USA, 2002), p. 540. (Proceedings Conference)

The article should be supplemented by:

• letter from the organization where the work was performed or from the authors of the work applying for the publication of the article;

• information on the author (authors): last name and initials; full name and postal address of the institution where the author works; academic degree; position; telephone number; E-mail;

• author's (authors') photo in color or, as an exception, in black and white. With the number of authors more than two their photos are not given;

• author's application to the following effect:

We, the undersigned authors, … transfer to the founders and editors of "Journal of Thermoelectricity" the right to publish the article…in Ukrainian, Russian and English. This is to confirm that the present publication does not violate the copyright of other persons or organizations.

Date Signatures

Below is given an example of article preparation.

Author's photo 3 × 4 cm

A.I. Casian[1], B.M. Gorelov[2]

[1]Technical University of Moldova,
168, Stefan cel Mare Ave.,
Chisinau, MD-2004, Moldova;
[2]Institute of Surface Chemistry of National Academy
of Sciences of Ukraine, 17, Gen. Naumov Str.,
Kyiv, 03164, Ukraine

Author's photo 3 × 4 cm

STATE OF THE ART AND PROSPECTS OF THERMOELECTRICITY ON ORGANIC MATERIALS

The aim of the paper is to analyze the expected thermoelectric opportunities of organic materials, including some highly conducting quasi-one-dimensional crystals. It is shown that interest of investigators in these materials has been growing recently. Quasi-one-dimensional organic crystals have high prospects for thermoelectric applications. These materials combine the properties of multi-component systems with more diverse internal interactions and of quasi-one-dimensional quantum wires with increased density of electronic states. It is shown that the values of the thermoelectric figure of merit ZT ~ 1.3 – 1.6 at room temperature are expected in really existing organic crystals of tetrathiotetracene-iodide, TTT_2I_3, if the crystal parameters are approaching the optimal ones.

Key words: thermoelectricity, tetrathiotetracene-iodide, polarizability.

Introduction

It is known that conducting organic materials usually have much lower thermal conductivity than the inorganic materials. Moreover, the organic materials can be fabricated by simpler chemical methods, and it is expected that such materials will be less expensive in comparison with the inorganic ones. Exactly these properties attracted attention to such materials for the use in thermoelectric (TE) applications long time ago [1, 2]. In spite of relatively high value of the thermoelectric figure of merit $ZT = 0.15$ at room temperature observed in polycopper phthalocyanine [2] as early as 1980, the thermoelectric properties of organic materials are still weakly investigated. This situation has the only explanation that thermoelectricians are still weakly interested in organic materials, and organic chemists are also weakly interested in thermoelectric materials. Moreover, in order to seek good organic thermoelectrics, it is necessary to organize multidisciplinary consortiums of physicists, organic chemists and engineers in the field of thermoelectricity. …

The aim of this paper is to present briefly the state-of-the-art of investigations in the area of new organic thermoelectric materials and to describe the nearest expected results for really existing quasi-one-dimensional organic crystals of tetrathiotetracene-iodide, TTT_2I_3.

Quasi-one-dimensional organic crystals of TTT_2I_3

The structure of quasi-one-dimensional organic crystals of tetrathiotetracene-iodide, TTT_2I_3, has been briefly described in [34]. These needle-like crystals are formed of segregate chains or stacks of planar molecules of tetrathiotetracene *TTT*, and iodine ions. The chemical compound TTT_2I_3 is of mixed-valence: two molecules of *TTT* give one electron to the iodine chain which is formed from I_3^- ions. The

conductivity of iodine chains is negligibly small, so that only *TTT* chains are electrically conductive and holes serve as carriers. The electrical conductivity σ along *TTT* chains at room temperature varies between 10^3 and $10^4\ \Omega^{-1}\text{cm}^{-1}$ for crystals grown by gas phase method [35], and between 800 and $1800\ \Omega^{-1}\text{cm}^{-1}$ for crystals grown from solution [36]. Thus, the conductivity is very sensitive to crystal impurity and perfection which depends on growth method. In the direction perpendicular to chains σ is by three orders of magnitude smaller than in the longitudinal direction and is neglected. …

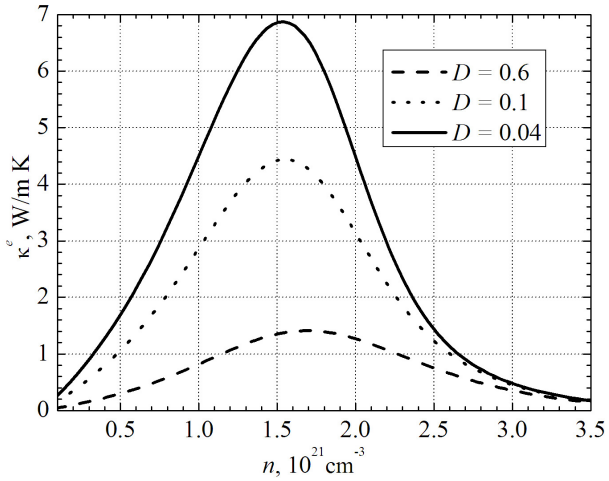

Fig. 1. Dependences of electron thermal conductivity κ^e *on n.*

$$\sigma = R_0,\ S = R_1 / eTR_0,\ \kappa^e = \left(e^2T\right)^{-1}\left(R_2 - R_1^2 / R_0\right), \tag{1}$$

Thermoelectric properties

Expressions (2) – (3) have been calculated in order to determine the thermoelectric properties of quasi-one-dimensional organic crystals of TTT_2I_3 with different degrees of purity….

Conclusions

The state-of-the-art of research on new organic materials for thermoelectric applications is analyzed. It is shown that the interest of investigators in these materials has been growing in recent years. The highest value of $ZT \sim 0.38$ at room temperature has been measured in doped acetylene, with the only problem that this material is not stable. Accurate control of the oxidation level in poly (3, 4-ethylenedioxythiophene) (PEDOT) gave the power factor $324\ \mu\text{W}\cdot\text{m}^{-1}\text{K}^{-2}$ and in combination with its low intrinsic thermal conductivity ($\kappa = 0.37\ \text{W}\cdot\text{m}^{-1}\text{K}^{-1}$) yielded $ZT = 0.25$ at room temperature, and this material is air-stable….

References

1. Ali Shakouri, Recent Developments in Semiconductor Thermoelectric Physics and Materials, *Annu.Rev.Mater.Res*.**41**, 399-431 (2011).
2. L.I. Anatychuk, *Thermoelectricity, Vol.2, Thermoelectric Power Converters* (Kyiv, Chernivtsi: Institute of Thermoelectricity, 2003), 376p.
3. M.E. Bengen, *German Patent Appl*. OZ 123, 438, 1940; *German Patent* 869,070, 1953, Tech. Oil Mission Reel, 143,135, 1946.